Università degli Studi di Trieste

Dipartimento di Ingegneria e Architettura
XXXI ciclo del Dottorato di Ricerca in Ingegneria e Architettura

Ph.D. thesis
funded by The Research Hub^{TM} by Electrolux Professional

Numerical modelling of thermal systems for professional food service appliances

ING-IND/10

Ph.D. Candidate
Eng. EMIDIO TIBERI

Supervisor
Prof. Eng. PAOLO GALLINA
Co-Supervisor
Prof. Eng. MARZIO PILLER
Ph.D. Coordinator
Prof. Eng. DIEGO MICHELI

Company Scientific Referee
Ph.D. Eng. RICCARDO FURLANETTO
Company Technical Coordinator
Ph.D. Eng. MICHELE SIMONATO

Academic Year 2017-2018

Contents

List of Figures

List of Tables

Nomenclature

Chapter 2

0	Initial condition *subscript*
α	Thermal diffusivity $[m^2/s]$
α_{th}	Thermal resistivity coefficient $[1/K]$
β	Thermal expansion coefficient $[1/K]$
$\tilde{\mathbf{v}}, \tilde{D}, \tilde{f}$	Values corrected with the contraction coefficient
$\delta_{i,j}$	Kronecker function
∞	Nozzle exit condition *subscript*
λ	Thermal conductivity $[W/mK]$
μ	Dynamic eddy viscosity $[Pas]$
μ	Dynamic viscosity $[Pa\,s]$
∇	Nabla operator $[1/m]$
ν	Kinematic viscosity $[m^2/s]$
ω	Turbulent frequency $[1/s]$
Φ	Dissipation function $[W/m^3]$
ρ	Density $[kg/m^3]$
$\sigma_k,\ \beta^*,\ \sigma_{\omega,1},\ \sigma_{\omega,2},\ \gamma_2,\ \beta_2$	$SST\ k-\omega$ turbulence model coefficients
τ	Characteristic time $[s]$
τ_{max}	Safety time for SRI $[s]$
$\mathbf{v}$	Velocity vector $[m/s]$

$\tilde{H}$	Volumetric enthalpy $[J/m^3]$
ζ	Contraction coefficient
A	Area $[m^2]$
av	Volume average *subscript*
Bi	Biot number
c	Specific heat $[J/kgK]$
CFD	CFD obtained *subscript*
D	Diameter of the nozzles $[m]$
f	Relative nozzle area
g	Gravitational acceleration $[m/s^2]$
H	Distance between the jet exit and the wall $[m]$
h	Convective heat transfer coefficient $[W/m^2K]$
$hexagon$	Hexagon geometry *subscript*
I_t	Turbulence intensity $[\%]$
k	Turbulent kinetic energy $[m^2/s^2]$
l	Turbulence length scale $[m]$
$Martin$	Martin correlation *subscript*
Nu	Nusselt number
P	Pressure mean component of the Reynolds decomposition $[Pa]$
p	Pressure $[Pa]$
p_j	Distance between two adjacent jets (pitch) $[m]$
Pr	Prandtl number
q_w	Heat flux $[W/m^2]$
r	Condition at T_r *subscript*
R_w, R_r	Electric resistances $[\Omega]$
Ra	Rayleigh number
Re	Reynolds number

Ri	Richardson number
$S_{i,j}$	Shearing linear deformation components $[1/s]$
$safe$	Safety condition *subscript*
SRI	Safety Risk Indicator
$STUI$	Simulated Temperature Uniformity Index
T	Temperature $[K]$
t	Time $[s]$
tg	Target value *subscript*
$TrUI$	Transient Uniformity Indicator
u', v', w'	Velocity fluctuating components of the Reynolds decomposition $[m/s]$
U, V, W	Velocity mean components of the Reynolds decomposition $[m/s]$
u, v, w	Velocity vector components $[m/s]$
U_g	Overall thermal transmittance $[W/m^2K]$
UI	Uniformity Index
V	Volume $[m^3]$
VI	Velocity Indicator $[h]$
w	Condition at T_w *subscript*
$wall$	Wall condition
x, y, z	Cartesian coordinates $[m]$
x_{max}	Boundary condition for $x = x_{max}$ *subscript*
x_{min}	Boundary condition for $x = x_{min}$ *subscript*
y_{max}	Boundary condition for $y = y_{max}$ *subscript*
y_{min}	Boundary condition for $y = y_{min}$ *subscript*
z_{bottom}	Boundary condition for $z = z_{bottom}$ *subscript*
z_{top}	Boundary condition for $z = z_{top}$ *subscript*

Chapter 3

β	Attenuation coefficient $[1/m]$

$\dot{m}$	Mass flow $[kg/s]$
ϵ	Radiation emissivity
ϵ_{in}	Burner boundary emissivity
η	Exhaust efficiency
λ	Thermal conductivity $[W/mK]$
μ	Dynamic viscosity $[Pa\,s]$
∇	Nabla operator $[1/m]$
ν	Wavelength $[m]$
ω	Solid angle $[sr]$
$\overline{u_i'u_j'}$	Reynolds stress tensor $[m^2/s^2]$
Φ	Dissipation function $[W/m^3]$
Φ'	Scattering phase function
ρ	Density $[kg/m^3]$
σ	Stefan-Boltzmann constant [W/m^2K^4]
σ_s	Scattering coefficient $[1/m]$
τ	Optical thickness
$\mathbf{q''}$	Radiative heat flux vector $[W/m^2]$
$\mathbf{v}$	Velocity vector $[m/s]$
ε_{th}	Thermal efficiency according the $\varepsilon - NTU$ method
ξ	Thermo-hydraulic efficiency
A	Area $[m^2]$
a	Radiation absorption coefficient $[1/m]$
b	Concentration of gaseous combustion products
Bo	Boltzmann number
Bo'	Modified Boltzmann number
C_D	Drag coefficient
c_p	Constant pressure specific heat [J/kgK]

c_v	Constant volume specific heat $[J/kgK]$
D_h	Hydraulic diameter of the tube *subscript*
E	Surface emissivity power $[W/m^2]$
e	Air-fuel equivalence ratio
E_b	Black body surface emissivity power $[W/m^2]$
F_D	Drag force $[N]$
F_{ij}	View factor of the surface i respect to j
G	Irradiation $[W/m^2]$
h_c	Convective heat transfer coefficient $[W/m^2K]$
I	Radiation intensity $[W/sr\,m^2]$
i	Specific enthalpy $[J/kg]$
I_b	Black body radiation intensity $[W/sr\,m^2]$
J	Radiosity $[W/m^2]$
L_c	Characteristic length $[m]$
LHV	Lower Heating Value $[MJ/kg]$
LSF, f_i	Logarithmic sensitivity factor
N	Total number of combustion products
Nu	Nusselt number
P_k	Turbulent kinetic energy production $[kg/ms^3]$
Pr	Prandtl number
Q	Heat power $[W]$
q	Heat flux $[W/m^2]$
Re	Reynolds number
S	Optical path length $[m]$
s	Generic coordinate $[m]$
St	Stanton number
T	Temperature $[K]$

t	Time $[s]$
u	Velocity component $[m/s]$
u'	Velocity fluctuating value in Reynolds average $[m/s]$
V	Volume $[m^3]$

Chapter 4

Δx	Spatial step $[m]$
$\dot{m}_{fan}$	Fan mass flow $[kg/s]$
ϵ	Emissivity
λ	Thermal conductivity $[W/mK]$
ρ	Density $[kg/m^3]$
σ	Stefan-Boltzmann constant [W/m^2K^4]
A	Area $[m^2]$
C	Cooking zone air *subscript*
C	Thermal capacity $[J/K]$
c	Specific heat $[J/kgK]$
e	Ambient *subscript*
F_{i-j}	View Factor from the i-th to the j-th surface
g_1, g_2	Glass door nodes *subscript*
h_{conv}	Convective heat transfer coefficient $[W/m^2K]$
L	Resistors characteristic length $[m]$
L	Walls characteristic length $[m]$
mC	Cooking zone thermal mass *subscript*
mP	Power zone thermal mass *subscript*
N	Number of walls
n	Timestep *subscript*
Nu	Nusselt number
P	Power zone air *subscript*

P_{el}	Electric power $[W]$
P_{rad}	Radiation power $[W]$
Pr	Prandtl number
$R1, R2$	Power zone resistors *subscript*
R_g	Overall glass thermal resistance $[Km^2/W]$
R_{conv}	Convective thermal resistance $[Km^2/W]$
R_{conv}	Radiative thermal resistance $[Km^2/W]$
Re	Reynolds number
T	Temperature $[K]$
t	Time $[s]$
V	Volume $[m^3]$
w	Wall node *subscript*
ws	Superficial internal wall node *subscript*

Chapter 1

Motivations, aims and executive summary

Numerical models are very popular in industry thanks to their efficiency in terms of time saving and high level of details for the investigation of physical phenomena.

In industrial applications a numerical model has to be accurate in reproducing the physical phenomenon under investigation, but at the same time robust and computationally efficient. In this thesis three technologies used for food service professional appliances are modelled by numerical models computationally-efficient and reliable. The reliability of these *virtual* models is assessed by extensive experimental validation carried out in Electrolux Professional's laboratories. Thanks to their characteristics, the models can be used in optimization processes, which are considered fundamental during the product development to maximize the efficiency and the performance of industrial machines. Robustness is a further key feature of the proposed models, which makes them suitable for investigating different working conditions and geometries, with a very low number of tuning parameters.

Executive summary

The thesis is organized in three main chapters, each focusing on a different physical process used in the food industry. In the second chapter the *jet impingement technology* is investigated: high speed jets, issued from a single nozzle or an array of nozzles, are directed towards a surface for heat and/or mass transfer operations. A huge literature focused on this technology, which has been used since the second half of the XX century, but only recently it has been introduced in the food processing. An innovative design methodology is proposed in this work, combining reliability and low execution time. The method consists in using a sequence of two numerical models, a Computational Fluid Dynamic (CFD) model and a Finite-Difference heat-conduction model (FDHCM). The CFD model is used to calculate the transient distribution of the convective heat transfer coefficient on the surface of the solid item placed below the array of jets in a confined chamber. The distribution is then used as boundary condition for the FDHCM, which simulates the temperature distribution within the solid object. The choice of such methodology permits to have a consistent saving of time, because a complete Conjugate Heat Transfer (CHT) CFD simulation requires a high computational cost to simulate hours of real process. The methodology has been validated by experimental tests carried out in an in-house test rig. The setup of the models and the description of the experimental tools is presented in detail.

In the first step the validation of the velocity field is shown for three representative free-jet regions by the comparison of CFD simulation with experimental data obtained by a hot wire anemometer. The experiments are carried out with Reynolds of 21000 and with a distance between the nozzle exit and the surface of 5 diameters.

After the fluid-dynamic study, the thermal field is extensively analysed. The outcomes from the CFD model, in terms of Nusselt number distribution, are compared against experimental data obtained with the micro-calorimeter technique for two Reynolds number (16000 and 21000). The heat flux is measured by a series of small copper disks, featuring a fast response time.

The validated distributions are then used as boundary conditions for the FDHCM for two test cases: the cooling down process of a thin metal slab and the thawing of a thick Tylose brick (a *food analog*). In the first study, a thin metal slab is firstly heated up by an external heater and then cooled down by the jet impingement flow. Eleven temperature data are measured in transient state and a good agreement has been found when compared with the numerical results. An important outcome from this study is the importance of taking into account the spatial distribution of the convective coefficient on the temperature field and for this purpose the distribution obtained by the CFD code has been compared against a semi-empirical correlation which provides a surface average convective heat transfer coefficient as boundary condition. The use of an average coefficient leads to an underestimation of the cooling effect of the array of jets, especially at the stagnation points.

In the second test case the thawing process of a Tylose brick has been studied. The Tylose is a meat analog material, whose thermal properties are well known in literature. Indeed the thawing process is simulated by using the laws of the specific heat and of the conductivity which vary with the temperature. For the experimental data the temperature is monitored within the Tylose brick by seven thermocouples. An excellent agreement between numerical and experimental data has been found. Also in this case the importance of a detailed distribution of the Nusselt number has been remarked, especially for the regions of solid near the stagnation points. three thawing indicators are proposed, which are representative of the uniformity, safety and velocity of a thawing process.

Eventually, we have compared a one-side impingement with a two-side configuration, finding promising results in terms of productivity and safety.

In the third chapter a CFD model of a gas boiler, used into food service professional ovens, is presented. The gas boiler is the device responsible of the steam production for steam cooking operations. We propose a reliable and computationally efficient CFD model to simulate the thermal behaviour of such device in steady state conditions, without taking explicitly into account both combustion and water boiling. The CFD model is validated against experimental data, obtained by an in-house test rig.

The heat release rate of the actual combustion process, taking place within the combustion chamber, is replaced by an equivalent flow of hot exhaust gases, released from the burner with a specific composition and thermodynamic properties, satisfying the energy balance of an ideal combustion. The diffusion, convection and turbulent dispersion of the different gas species are neglected: hence, the composition of the exhaust gas is assumed constant and homogeneous. The radiation heat transfer is modelled by assigning radiative properties to the burner surface. The role of the exhaust gases in the radiation heat transfer within the combustion chamber is investigated comparing the *Participating Media* (PM hereinafter) model (where the fluid can interact with the radiation field) against the *Surface to Surface* (S2S hereinafter) model (where only the solid surfaces can exchange radiation flux and the fluid is transparent to the radiation). The boiling process is not explicitly considered and a uniform temperature, corresponding to water saturation at ambient pressure, is assumed on the water side of the heat exchange surface.

Numerical and experimental results are compared for several operating conditions, finding an excellent agreement. The two radiation models provide comparable accuracy, but the S2S model requires almost 30% of the computational cost of the PM model.

In the third chapter a numerical model of a food service professional oven is presented. The oven is represented as a thermal system in which the main components are described with the lumped-capacitance approach. The components are inter-linked by conduction, convection and radiation heat fluxes. The system is conceptually divided in two zones, the *Power Zone* and the *Cooking Zone*, which correspond physically to the region where the electric power is dissipated into thermal power by the electric heaters and the region where the food is placed within the oven. Practically in the real oven the two regions are divided by a sheet metal wall, which is used to separate the two zones: in the Power Zone a centrifugal fan is used to create a recirculating airflow and convey the thermal power to the Cooking Zone by forced convection. The thermal system is considered analog to an electric circuit and the set of algebraic equations is described in detail. The forced convection heat transfer is represented by convection coefficients, which are not known a priori and are intended as *tuning parameters*; consequently a tuning procedure with experimental data is discussed. At the same time the radiation heat transfer is described in detail by means of the *net radiation method for enclosures*. Finally some results about the thermal behaviour of the oven have been presented and discussed, regarding the temperature distribution within the oven and its energy consumption.

The use of virtual prototyping is fundamental for Electrolux Professional: in particular, the increasing demand of more efficient energy technologies and solutions has been a boost for the development of models able to predict the behaviour of thermal machines. The three technologies described in this thesis are a practical example of the benefits that can be achieved with numerical models. In fact, often the increase of the efficiency is linked to the introduction of more sophisticated control strategies or simply more complex architectures with different integrated components. Thus an analysis through experiments is often time-consuming, especially to find the root causes in such complex systems, in terms of sensor numbers, sensor calibration, prototypes and data analysis. On the contrary, a virtual model can be a powerful tool, especially when several of parameters have to be taken into consideration.

Chapter 2

Jet impingement technology for food service

2.1 Introduction

Jet impingement is an efficient heat- and mass-transfer technology where a high-speed flow, issued from an array of nozzles, is directed towards an object. In the present work we want to investigate the application of this technology for professional food processing appliances. An industrial design tool is proposed and validated: it allows to derive the temperature distribution within a prototypic food item, which is heated or cooled by jet impingement. The method combines a 3D Computational Fluid Dynamics model (CFD hereinafter) and a Finite-Difference heat-conduction model (FDHCM hereinafter), to study the efficiency of this heat transfer process. The validation of the proposed methodology is carried out by comparing the predicted temperature evolution at selected locations within solid object against thermocouple readings.

2.2 State of the art

2.2.1 Jet impingement technology in general

The study of the jet impingement technology started in the second half of the XX century, as advanced heat transfer technology to provide high convective heat transfer coefficients. Nowadays the use of jet impingement is very popular in many industrial applications, like paper drying (Di Marco et al. (2016)), glass tempering (Yu et al. (2017)), cooling of turbine blades (Liu et al. (2018)) and electronic board cooling (Fabbri et al. (2005)). Martin (1977) proposes a very extensive investigation on the jet impingement technology, introducing a wide range of semi-empirical correlations for the heat and mass transfer coefficients. In some applications the presence of a secondary flow (typically orthogonal to the main flow) can influence the heat and mass transfer at the solid wall. This effect is called *crossflow* effect. Florschuetz et al. (1980) investigate experimentally the heat transfer characteristics of an array of nozzles designed to cool the midchord region of air cooled gas turbine airfoils. It is one of the first complete studies about array of jets with in-line and staggered configurations. The main aim of the work is to understand the effects of the crossflow on the heat transfer coefficients and they remark that an increase in the crossflow rate is not always linked to a decrease in performance. Zuckerman and Lior (2006) propose an extensive investigation of the jet impingement technology, presenting a huge explanation of the fluid-dynamic mechanisms and the way in which they can be simulated numerically. Moreover an extensive set of semi-empirical correlations is reported. It is verified that jet impingement, compared to convection cooling by confined flow parallel to the cooled surface, produces convective coefficients up to three times higher at a given maximum flow rate. O'Donovan and Murray (2007a) and O'Donovan and Murray (2007b) propose a detailed experimental investigation, looking at the correlations between the heat transfer at the surface and the velocity signal spectra. In particular, the time dependent velocity signals are acquired by the Laser Doppler methodology and then processed to correlate the effects of the structure of the vortices with the turbulent structures that have a direct impact on the heat transfer on the surface.

2.2.1.1 Jet Impingement Regions

The description of the jet impingement technology starts from the definition of several distinct regions, as shown in figure 2.1. The first region starts from the exit of the nozzle, where the flow presents a velocity profile dependent on the type of nozzle used: for pipe-shaped nozzles the velocity profile is parabolic with a moderate amount of turbulence generated within the pipe; on the contrary for sharp-edged nozzles the velocity profile at the nozzle exit is very flat, with less turbulence and with the development of the *vena-contracta* downstream the exit. This first part is called *initial free-jet* region, and it extends from the nozzle exit to the apex of the *potential core* (the potential core is the central portion of the flow in which the velocity remains constant and equal to the velocity at the nozzle exit). In this region the jet behaves as a free jet (if the distance between the nozzle and the solid surface is very low, compared to the nozzle diameter, this region may not develop) and the outer regions of the flow start to interact with the fluid at rest (as it can be seen in figure 2.2), forming the shear layer and pulling additional fluid along the jet (this effect is called *entrainment*). The shear layer is a great source of turbulence, as it is evident in figure 2.3. Both the figures 2.2 and 2.3 are retrieved from the CFD simulations carried out in this work.

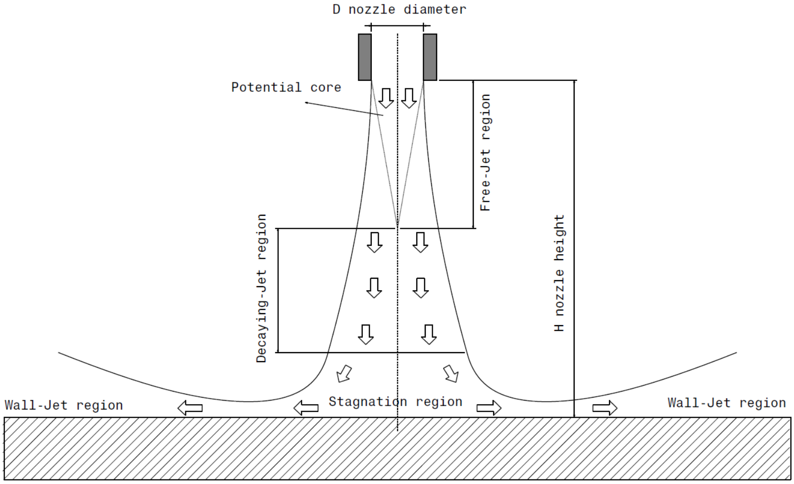

Figure 2.1: The flow regions of an impinging jet.

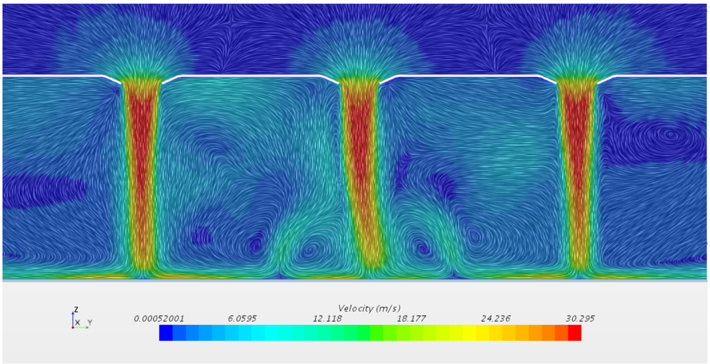

Figure 2.2: The velocity flow field on a section plane.

Downstream this region the axial velocity component decreases (forming the *decaying region*) and the jet spreads progressively in the transverse direction. Approaching the wall the jet decelerates further and bends, forming the so-called *stagnation region*: here the flow is characterized by a high static pressure and high gradients, which greatly influence the local transport properties. After turning, the flow moves parallel to the wall, entering in the *wall-jet* region. In this region a boundary layer forms and grows up progressively along the solid surface.

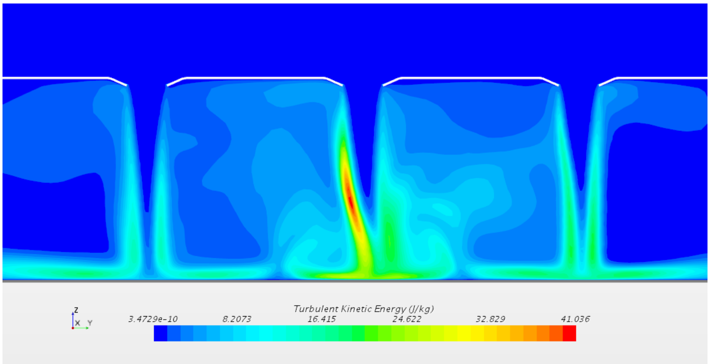

Figure 2.3: The turbulence kinetic energy field on a section plane.

In the study of jet impingement the distinction between laminar and turbulent jet is fundamental. In the present work we will refer only to turbulent submerged subsonic jets, as the minimum value of Reynolds number is above 15000 and the maximum Mach number is below 0.3. Further details about the fluid-dynamics of impinging jets can be found in (Vickers (1959) and Martin (1977)).

In practical applications the use of an array of nozzles is very common; this is due to the necessity of having a more uniform distribution of the convective heat transfer coefficient over large surfaces. The relative position of the nozzles in the array is generally indicated as *pitch* and can lead to effects of interaction between the jets. The interaction is due to the combination of two neighbouring shear layers, which decrease the velocity gradients in magnitude, reducing an important source of turbulence. Two neighbouring jets can interact also in the wall-jet region, due to the combination of the respective boundary layers, which create another stagnation region and an upward flow (in what are commonly called *fountains*, clearly visible in 2.2). In the fountain regions the heat transfer coefficient may present a higher value than in the wall-jet regions, due to the high turbulence production during the interaction of the boundary layers (Fenot et al. (2005) and Huber and Viskanta (1994)). Multiple jet impingement unfortunately is characterized by the presence of the *crossflow* effects, i.e. the interaction between a secondary stream and the jet flow (as in figure 2.4).

The source of a crossflow can be manifold, in the present work the crossflow is due to the fact that the internal jets of the array have to deliver the flow towards the exit channels, which are present at the border of the confined chamber, creating secondary flows which interact with the other jets. When the crossflow occurs, the section of the main flow tends to bend and create a bean shape (the reader will notice this characteristic in the flow field simulated in the present work). Practically the crossflow tends to degrade the heat transfer rate, as reported by several authors (Florcshuetz et al. (1981)) and its entity is strongly dependent

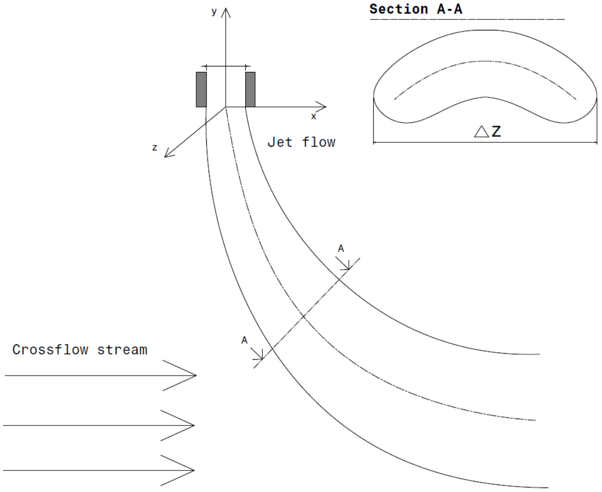

Figure 2.4: The effect of crossflow on the jet.

on the geometric configuration of the array; in confined domains the position of the outlet channels influences significantly the intensity and the direction of the crossflow. Onstad et al. (2009) propose to reduce the intensity of the crossflow by removing the spent flow from each jet through extraction holes, placed on the array of jets.

2.2.1.2 Jet Impingement parameters

The main advantage of the jet impingement is the presence of very thin boundary layers that induce high transport coefficients. For convection heat transfer processes the heat transfer coefficient is defined as:

$$h = \frac{-\lambda \partial T / \partial n}{T_{\infty} - T_{wall}} \tag{2.1}$$

where λ is the fluid conductivity.

The typical thickness of the velocity boundary layer at the stagnation region is no more than 1% of the jet diameter (Martin (1977)).

Generally for an array of jets (with the jet axis orthogonal to a flat solid surface) the experimental results of surface average Nusselt number are correlated by the form:

$$Nu = \frac{hD}{\lambda} = C Re^{m} Pr^{n} f(H/D, p_j/D)$$

where f is an empirically determined function, C,m,n are empirical constants, Re is the Reynolds number defined with the diameter of the nozzle as characteristic length, Pr is the Prandtl number, H/D is the nozzle-to-plate ratio and p_j/D is the dimensionless distance between the axes of the nozzles.

2.2.2 Specific applications of jet impingement for food processing

In food processing the jet impingement has been widely used in the past, mainly for heating and drying processes. Smith (1973) filed a patent where he describes a *cooking apparatus* which uses jets of temperature controlled air to cook food. He indicates also a possible combination of jet impingement with microwaves, combining the superficial and volumetric heat transfer mechanisms. Ruocco et al. (2011) carry out an optimization study of an oven prototype in which jet impingement is combined with microwaves. Their investigation focus on the analysis of the best impingement/microwave combination, in terms of power distribution, in order to obtain a combination of superficial and volumetric effects that maximizes the temperature uniformity during a heating process. A. Li and Walker (1996) propose a comparative study between conventional, impingement and hybrid ovens; they conclude that air impingement increases four times the superficial heat transfer coefficient, reducing the baking time to half compared to conventional ovens, moreover if combined with microwave the time is reduced by an half again. One of the first fluid-dynamic studies about an impingement oven is presented by Marcroft and Karwe (1999); they investigate the velocity field of one single jet in a commercial jet impingement oven using a laser Doppler anemometer. Nitin and Karwe (2001) provide correlation for the heat transfer process of cookie shaped objects within a jet impingement oven; they evaluate the effects of the interaction between the airflow and the cookies, highlighting the importance of the spatial variation of the convective heat transfer coefficient and the variation of the dimensions of the items on the cooking performance. Ovadia (2000) filed a patent about an impingement oven for pizza. In his invention the impingement is used to increase the uniformity of heating across the oven and to reduce the cooking time. This is one of the first inventions about impingement ovens that introduces pulsating jets and compressed air instead of fans. Wählby et al. (2000) have been one of the first to introduce the effect of the impingement technology on the quality of the food. In particular they observe that the impingement technology lead to a lower weight-loss than conventional ovens and a remarkable reduction of time for large meat pieces. The importance of introducing quality criteria to evaluate the performance of a heating technology will be remarked also in this work in the chapter related to the use of the jet impingement for thawing processes.

However the jet impingement was not studied only for heating processes:

Bórquez et al. (1999) discuss about the use of jet impingement for driers. They introduce a physical model to simulate the drying process, finding a good agreement by the comparison with experimental data. Moreira (2011) presents a work about impingement driers and she compared the performance of hot air jets with steam jets, remarking that, during the drying process, the use of superheated steam can produce potato chips with less color deterioration and less nutritional losses than using hot air. Wang et al. (2017) and Xiao et al. (2014) propose steam impingement as blanching system for agricultural products.

The use of jet impingement was also investigated for the refrigeration field: Salvadori and Mascheroni (2002) investigate the performance of an impingement freezer. They propose a numerical tool to predict the heat and mass transfer process and they validated the mentioned model with experimental data. Thus, they remark that the use of jet impingement lowers remarkably the freezing process with respect to conventional devices, stating that the freezing times and the weight losses are comparable to cryogenic freezing.

The use of jet impingement for thawing processes has been proposed theoretically by several authors (e.g. Smith (1973)), but few of them analysed a complete array of nozzles. Anderson and R. Singh (2006) propose an inverse method to estimate the distribution of an effective heat transfer coefficient for a single impinging jet on the surface of a nylon disk.

In the present work we propose a design tool to estimate the effects of jet impingement technology on food processing, in particular for the case of thawing processes. The novelty behind this work is the study of the jet impingement technology directly applied to a cavity which is representative of a real domain of existing thawing machines. In particular the presence of an array of jets in a confined domain for thawing processes has not been investigated in literature yet. Moreover we propose a methodology which takes both in consideration thermal aspects and food quality aspects, which are considered fundamental for Electrolux Professional when it comes to the description of thawing processes. In fact the jet impingement has been demonstrated to be very efficient on the thermal point of view, but few references exist on the effect of this technology on the food properties. In this work a complete treatment of the food quality is out of scope, but we provide some simple tools to create a solid basis for future works. The methodology is developed combining both experimental and numerical procedures. In particular the experimental data are obtained to validate a numerical tool that combines a CFD model with a FDHCM. The validation is done by steps, starting with the fluid-dynamic field, passing through the thermofluid-dynamic field and finally evaluating the thawing process of a food analog item.

2.2.2.1 Brief description of thawing processes in professional appliances

The thawing is a thermal process in which the food is heated from very cold temperatures (typically -18°C) to some degree above the 0°C. The heat can be exchanged with the food by the use of several heating technologies (the best known are still air, forced air, water, microwaves and radio frequency), but in this work we will refer only to the technologies in which a fluid is used as heating vector by direct contact with the frozen food. In this case the thawing is a very long process because it commonly does not rely on high temperature differences between the food and the fluid (for safety reasons, as described in Food-Safety (2017)), moreover it is a heat transfer process that takes place at the surface of the food by convection and then the heat is conveyed towards the internal zones by conduction. Consequently the increase in the heat transfer coefficient is a good strategy to increase the thawing speed, which is linked to an increase in productivity for professional machines and, for the most of the frozen products, to an increase in quality (Eastridge and Bowker (2011)). The thawing process can be potentially hazardous for some food (e.g. fish) due to the excessive exposure of the food to high temperatures for long time. In particular some regulations (e.g. Food-Safety (2017)) define a *dangerous zone*, as combination between temperature (in the range 4°C and 47 °C) and time spent at that temperature (e.g. 4 hours), where the development of bacteria is potentially dangerous. These effects make critical the use of high temperature thawing fluids and make also problematic the use of volumetric thawing technologies due to the problem of *hot spots* (e.g. the microwave technology is not suitable for heterogeneous food due to the uneven heating process). It is well known that some volumetric heating technologies, e.g. Radio Frequency, are very efficient in this field, but nowadays are used only for the *tempering* process, which means that the frozen food is heated up at a temperature below the melting point (typically between -5°C and -2°C). This process can not be accepted when we want to restore the fresh conditions of the food, in particular because the tempering process ends just before the melting phase, which is the longest period of a thawing process. The existing thawing machines on the market are forced convection air machines, which use a fan to move the air and establish a forced convection regime. However the fluid-dynamic efficiency of such airflow is often low (the typical convective heat transfer coefficient is of the order of 20-40 W/m^2K) and the shape of the cabinet makes difficult an even distribution of the air on the food surfaces. Consequently the thawing times are very long and the food is processed unevenly. In the present work we want to investigate the potentialities of a technology which is able to increase locally the heat transfer coefficient and provide a more structured and even distribution of the heat flux on the surface of the food.

2.3 Materials and methods

2.3.1 Test rig

A test rig has been designed to provide experimental data for the thawing process of a food analog. These, in turn, serve to validate the proposed design methodology. The facility, represented in figure 2.5, has been fully designed in-house and assembled in the Electrolux Professional's workshop. It consists of a closed loop air circuit endowed with a blower (ebm-papst centrifugal fan, backward curved type G1G170-AB31-01). The prescribed airflow is attained controlling the rotational speed of the fan by the PWM technique (Peddapelli (2017)) and an airflow meter is used to monitor the value of the airflow and control the blower. The airflow meter consists of a differential pressure meter Deltabar PMD75 (© Endress-Hauser) that measures the pressure loss across a calibrated orifice Deltatop D062C (© Endress-Hauser, figure 2.8b). The value of the pressure loss is then used to calculate the volume flow rate according to a calibration table.

The airflow meter is equipped with a gauge pressure meter (© Testo 312-4) and with a temperature sensor (thermocouple type T 36-gauge) for the compensation of the ambient conditions and to obtain the mass flow from the volumetric flow. A throttling valve is placed downstream the airflow meter to extend the range of operative conditions when the rotational speed of the blower is out of range. The core of the facility is the test chamber, a cavity with a basement of 420 mm x 420 mm and total height of 340 mm. On the top of the chamber a grid of nozzles is placed: in the present work each nozzle has a diameter of 15,5 mm with a pitch of 84 mm between each nozzle (staggered configuration, as in figure 2.7a). The nozzles are shown in details in figure 2.7b. Inside the test chamber a shelf can be moved vertically to study different nozzle-to-plate (H/D) distances. The grid can be changed easily to test other configurations. A plenum is used to slow down the air above the nozzles and to uniform the velocity profile among all the nozzles; in particular the plenum is a conical diffuser, with a total height of 850 mm, a radius of 340 mm for the lower base and a radius of 50 mm for the upper base. The thermal conditions within the test chamber are adjusted by a heater and a chiller that are controlled by the temperature signal in the test chamber (hysteresis control strategy with 1 K dead-band). The heater is made of tubular resistors, with a total power of 8.25 kW; the chiller is extracted from a professional blast-chiller (figure 2.8a) and it is characterized by power rate of 1.6 kW at -30°C (R404a as refrigerant). The exhaust flow from the test chamber is filtered and then recirculated at the blower inlet. For all the experiments the temperature of the laboratory is controlled and kept between 20°C and 25°C with a relative humidity between 50 % and 60 %. All the measuring devices are connected with a © National Instruments acquisition station, made of a cDAQ-9174 chassis equipped with two NI-9213 modules (for the thermocouples) and one NI-9201 module for the analogical signals.

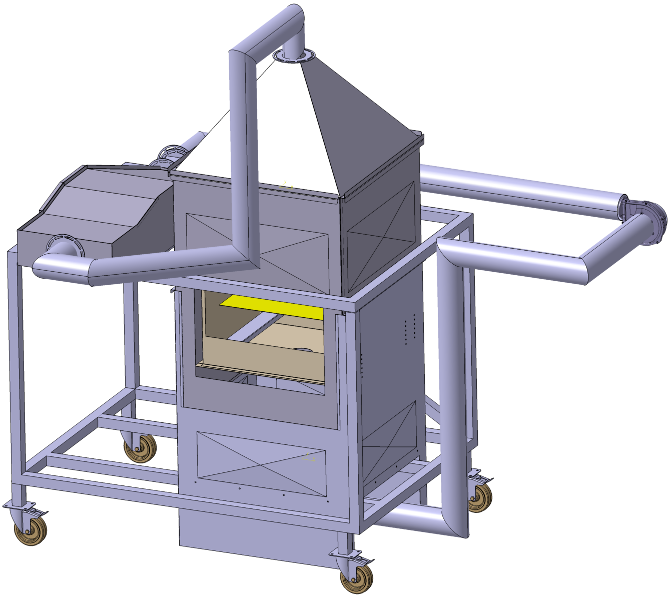

Figure 2.5: Test rig CAD drawing.

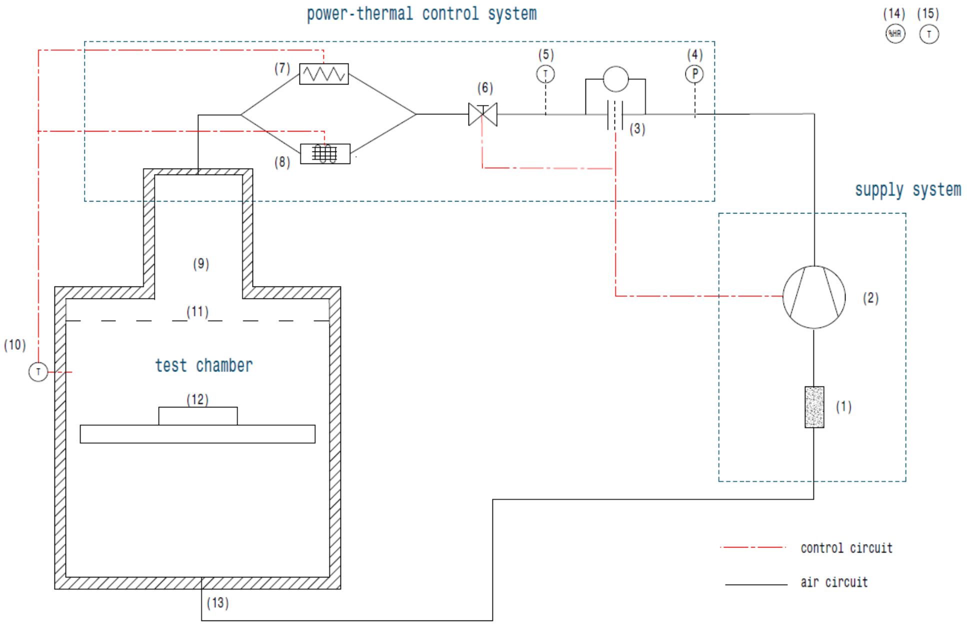

Figure 2.6: Test rig scheme: 1) air filter, 2) blower, 3) volumetric flow meter, 4) pressure gauge, 5) temperature transducer, 6) throttling valve, 7) heaters, 8) chiller, 9) plenum, 10) temperature transducer, 11) nozzles plate, 12) target, 13) recirculating duct.

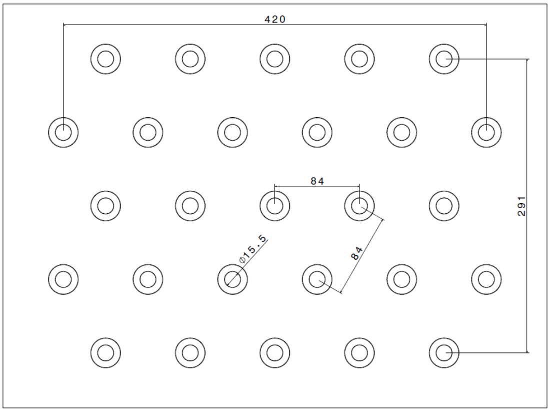

(a) Nozzles grid

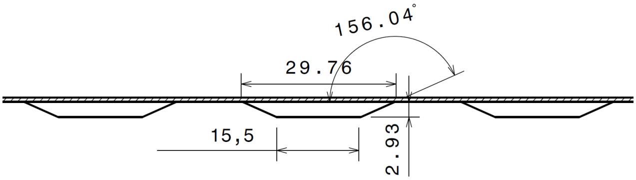

(b) Nozzles details

Figure 2.7: Nozzles geometry

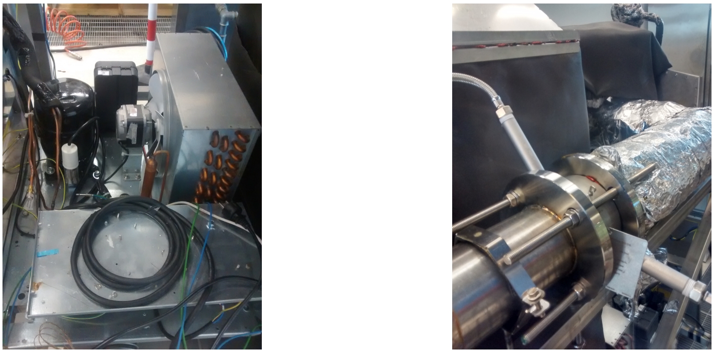

(a) Chiller (b) Calibrated orifice

Figure 2.8: A view of some components installed in the test rig

2.3.2 Hot wire anemometry

In the present work numerical data about the fluid-dynamic field are compared against experimental velocity data, obtained using the hot wire anemometer technique.

2.3.2.1 AN 1005 device

The hot wire anemometry is a well-known technique that permits to evaluate locally the velocity of a fluid (Lomas (2011)): the principle is based on the cooling effect of a fluid flow over a wire electrically heated. The cooling rate is related to the heat transfer coefficient between the fluid and the wire and consequently to the local velocity field. Generally two configurations are the most used: Constant Current Anemometry (CCA), where the probe is feed by a constant current and Constant Temperature Anemometry (CTA), where the probe is kept at constant temperature. The device used in this work is configured to operate in CTA, therefore the electrical resistance of the probe is constant (the value of the electrical resistance is a monotonically increasing function of the temperature, as described in equation (2.2), where R_w is the value of the resistance at T_w, R_r is the value of the resistance at the reference temperature R_r and α_{th} is the thermal resistivity coefficient). The change in the velocity of the fluid breaks the thermal equilibrium between the wire and the fluid, consequently the temperature of the wire changes and the electrical resistance of the wire changes as well, according to equation (2.2). The resistance comprises one leg of a Wheatstone bridge (figure 2.9b), therefore the change in the value of the resistance induces an unbalance in the value of the voltage across the bridge. This unbalance is received by the control system that modulates the value of the current that passes through both the legs of the Wheatstone bridge, inducing a change in the Joule effect and consequently the value of the temperature in the sensor wire changes until the bridge is balanced once more. The entity of the modulation is correlated to the value of the velocity of the fluid, which is finally determined.

$$R_w = R_r(1 + \alpha_{th}(T_w - T_r)) \tag{2.2}$$

The anemometer used for the experiments is a single-wire tungsten probe (type PII © Dantecs Dynamics), which can resist to air velocity in the range 0-150 m/s. The sensor is connected to the control and acquisition system AN 1005 (© A.A. Lab Systems Ltd.), a multi-channel station which is able to sample data up to 500 kHz. The reader can find further details about the setup characteristics of the AN1005 station in Pugliese (2017).

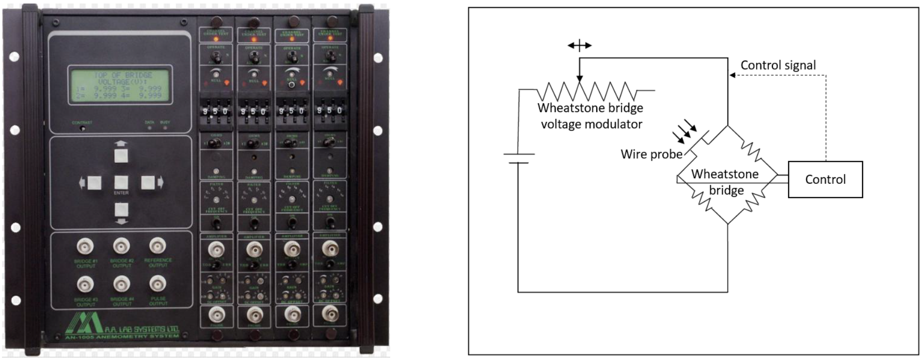

(a) AN1005 device

(b) CTA electrical circuit

2.3.2.2 Calibration procedure

The anemometer needs to be calibrated to correlate the output voltage to a value of the local velocity field. For the calibration a convergent nozzle feed by a volumetric compressor is used as benchmark device. The air is collected before the nozzle in a plenum, where a pressure transducer is used to calculate the static pressure that is then converted to dynamic pressure at the nozzle exit where the wire sensor is placed (figure 2.11).

Starting from the value of the dynamic pressure, it is possible to calculate the velocity of the air that passes through the hot wire; this value is then associated to the value of voltage read by the acquisition system (figure 2.13). The calibration procedure is referred to the velocity range 0-30 m/s with four repeats for each velocity value. The temperature of the air is kept at 20°C with 50% of humidity. The cooling effect of the air on the heated wire is dependent on the direction of the velocity vector respect to the orientation of the wire. It is interesting to evaluate the effect of a change in the position of the wire respect to the direction of the velocity, in particular if the value of the velocity direction can not be know accurately during the experiments *a priori*. This is useful to take some considerations about all the possible errors that affect the measuring procedure. Therefore the wire has been rotated around the axis of the holder (axis x in figure 2.10, considering the velocity direction coincident with the axis y), and the sensitivity analysis of the velocity measurement with the rotation angle has been summarized in figure 2.14 for different flow velocities. An error in 30° for the direction of the velocity field implies an error of the 12% for the value of the local velocity field.

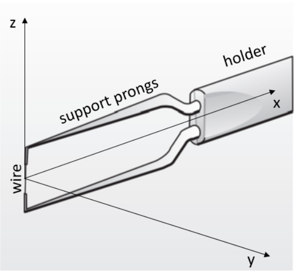

Figure 2.10: Wire probe

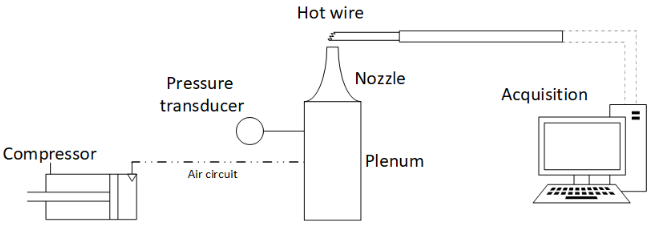

Figure 2.11: Configuration of the calibration system

(a) Pressure transducer

(b) The convergent nozzle and the anemometer wire

Figure 2.12: Some components used in the calibration procedure

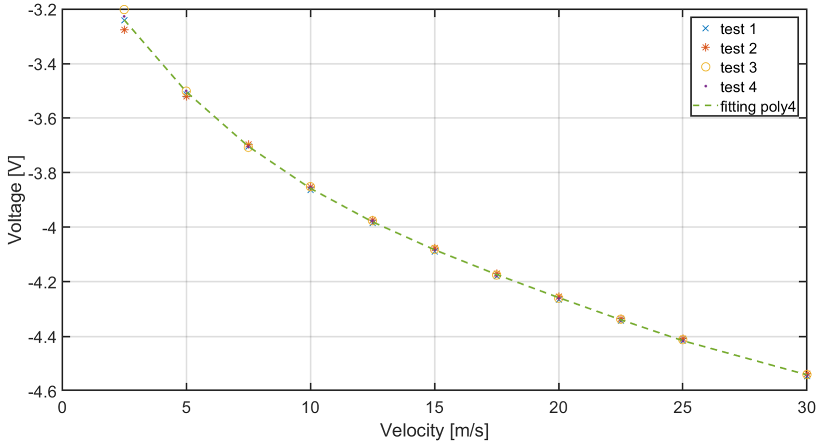

Figure 2.13: Calibration curve

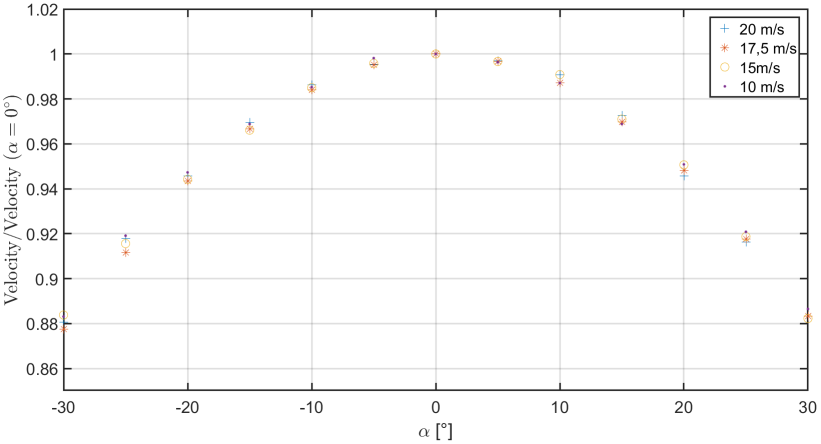

Figure 2.14: Wire angular sensitivity

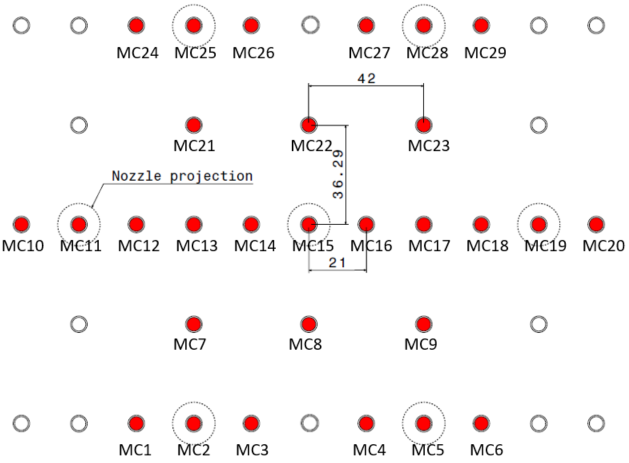

Figure 2.15: Setup configuration of the array of micro-calorimeters; the micro-calorimeters used for the tests are marked in red (dimensions in mm).

2.3.3 Micro-calorimeters

The distribution of the convective heat transfer coefficients on the surface below the array of jets is measured experimentally using the micro-calorimeter technique (Sarkar and R. Singh (2003)). In particular, a series of small copper disks (5 mm of diameter and 0.8 mm of thickness) is used as calorimeters (respecting the condition of Bi<0.01, the lumped-capacitance approach can be used) and therefore the disks can be described as isothermal bodies and their temperature evolution during a heating/cooling process can be used to estimate the heat transfer coefficient, according to the equation (2.3) (valid if the thermal properties of the medium are constant with the temperature).

$$\rho V \frac{dcT}{dt} = hA(T_\infty - T) \tag{2.3}$$

Where A is the surface of the copper disk exposed to the convective heat transfer with the fluid at T_∞. Moreover, if the convective coefficient, the specific heat of the copper and the temperature of the fluid are supposed constant, the ordinary differential equation can be easily solved (equation (2.4)).

$$T = T_\infty - (T_\infty - T_0)e^{-\frac{hA}{\rho V c}t} = T_\infty - (T_\infty - T_0)e^{-\frac{t}{\tau}} \tag{2.4}$$

As suggested by Sarkar and R. Singh (2003), each copper disk is insulated laterally from the copper plate with a low conductivity epoxy and it is also insulated on the bottom surface with polystyrene. Consequently, only the upper surface of the copper disk is exposed to the airflow. T-type fast-response thermocouples (0.25 mm of wire thickness) are used to monitor the evolution of the temperature inside each copper disk (figure 2.16). In particular the copper disk is melted in the Electrolux Professional's workshop by using the © Kemppi MasterTig 3003MLS TIG welding device and the thermocouples wires are annealed in the melted disk without using any additional welding material. In this way the uncertainties in the change in weight of the copper disk are reduced respect to the use of a solder.

An array of micro-calorimeters is designed to study the Nusselt number distribution for a grid of seven nozzles as in figure 2.15. 29 micro-calorimeters are used in the tests, because the acquisition station can monitor 32 thermocouples (16 fast-channels per module with 2 modules available). The position of the micro-calorimeters is optimized to have a good description of the heat transfer coefficients both in the stagnation zones and in the intermediate zones between the stagnation zones. Each module is configured to acquire at high velocity the temperature data (10 Hz), since the dynamics of each copper disk is very fast due to the low inertia and the high heat transfer coefficients (the mass of each copper disk is almost 0.140 g and the time-constant τ of the exponential law is 13.7 sec, considering a heat transfer coefficient of 200 W/m^2K).

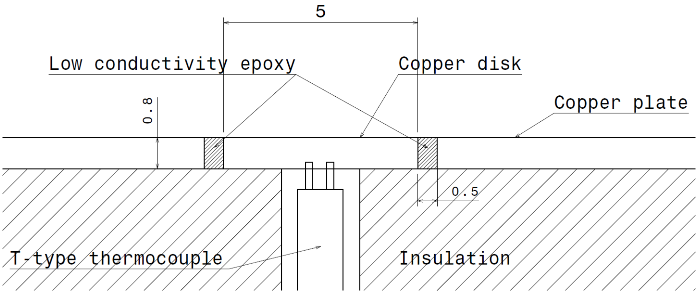

Figure 2.16: Setup configuration of each micro-calorimeter (dimensions in mm).

The first step of the experimental test consists of heating the copper plate with an electrical heating source, made with electrical resistors annealed in a block of aluminium to even the heat flow. When the copper disks reach, in average, the temperature of 65-70°C, the heating source is removed and the blower of the test rig is activated to cool down the copper plate with the jet flow at 30°C. The temperature of each disk is monitored until it almost equilibrates with the temperature of the fluid. In particular two Reynolds numbers have been tested (16000, 21000) considering one nozzle-to-plate distance (H/D=5) and each test is replicated three times (for this reason the *t-Student* tables are used to calculate the statistical error). The data are then analysed using the commercial package of numerical analysis Matlab$^{\mathrm{TM}}$ R2017b. Each profile of temperature is used to calculate the convective heat transfer coefficient, in particular the experimental data are approximated by an exponential law, as indicated in (2.4): if the exponential law well approximates the temperature data it means that the assumptions of constant convective coefficient and constant thermal properties are correct, on the contrary we have to use *locally* the exponential law (i.e. we have to consider a piecewise function). In this work we have found a good approximation for all the experimental profiles of temperature with a single exponential law, as found also by other authors (Sarkar and R. Singh (2003)).

2.3.4 The Tylose brick as *food analog*

The proposed numerical models rely on the following assumptions regarding the food item:

- Homogeneous and isotropic material
- Isotropic material
- Negligible density changes during the phase change
- Internal heat transfer by conduction only
- No mass transfer, such as evaporation, at the external surface
- Known thermal properties

Though most of the aforementioned assumptions could be relaxed, they make the model more robust (i.e. less adjustable parameters are involved) and easier to validate. The real food hardly respects all the requirements listed above: for this reasons, *food analogues* are commonly used. Riedel (1960) developed a substance that is nowadays the most used as meat analog. It is known as "Tylose", and it is a 23% methyl-cellulose gel (77 % water). The Tylose has many advantages: it can be moulded into different shapes; it remains homogeneous even after several experiments without deterioration and its density does not change remarkably in the temperature ranges of interest for the food processing. The thermodynamic data of Tylose are available in several research studies (Cleland; Bonacina and Comini; Anderson and R. Singh (1985; 1973; 2005)) and are here represented in figure 2.17. The phase change condition is easily recognizable by the abrupt change in thermodynamic properties and, as for the real food, it is spread over a range of almost 3-4 K.

The Tylose brick used in the experiments is adapted from a commercial Test Package type 1000 © MADI and a picture of the frozen brick is shown in figure 2.18a. The brick is equipped with thermocouples (type-T 36 gauge), placed in different positions within the gel, as reported in figure 2.18b. The number of

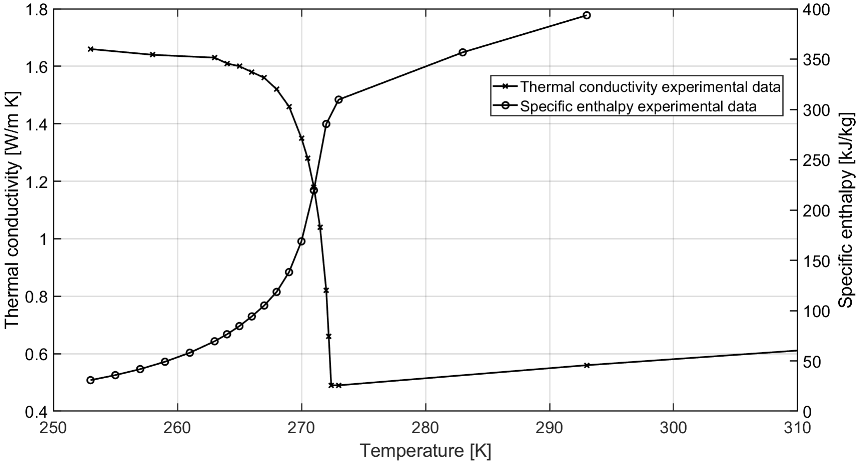

Figure 2.17: Thermal properties of the Tylose brick

thermocouples is dependent on the dimensions of the brick, because the presence of too many wires within the gel breaks the uniformity of the medium and consequently the reliability of the assumption accepted for the thermal model. The Tylose gel is wrapped into a thin layer of plastic film to limit the evaporation process, as it is out of the scope of the present work.

The present investigation focuses on the thawing process of the Tylose brick. The experimental test consists in freezing the brick in a freezing cabinet, for at least 12 hours, at -18°C. The brick is then placed in the jet impingement cavity over a tray under the array of jets, as in figure 2.19, and the blower is suddenly switched on. As for the experiments with the micro-calorimeters, a grid of seven nozzles is used. Temperature data are acquired until the lowest measured temperature reaches 0°C, which is considered a standard threshold to avoid any presence of residual ice inside the food (James et al. (1976)). Nine configurations have been studied experimentally, considering three Reynolds numbers, namely 17000, 23000 and 34000, corresponding to the minimum, half and maximum power of the blower respectively, and three nozzle-to-plate distances H/D (2, 5 and 8).

2.3.4.1 Thawing indicators

The thawing process of a food item in a professional machine has to respect some requirements: it should be uniform, safe and fast. These conditions ensure a high quality and healthy process and a high productivity of the machine (Eastridge and Bowker (2011)). Consequently, three *thawing indicators* are proposed in the present work, starting from the transient thermal field within the Tylose brick. Several authors introduce indicators to evaluate the performance of thawing pro-

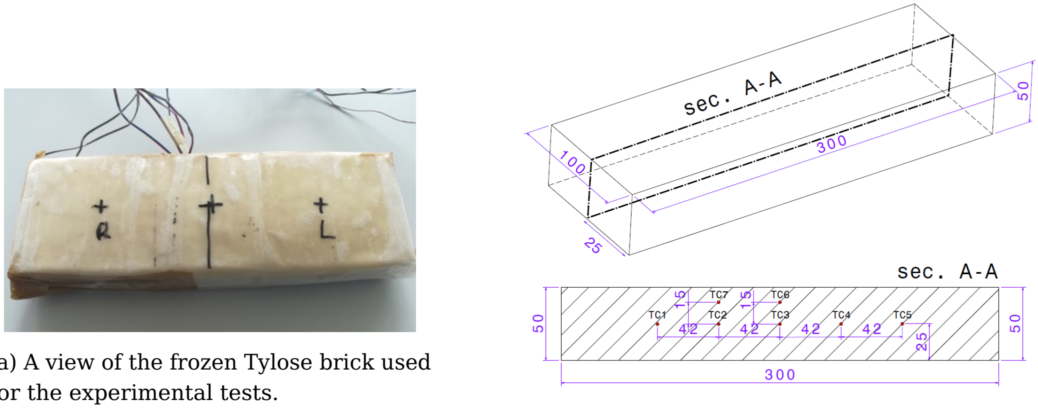

(a) A view of the frozen Tylose brick used for the experimental tests.

(b) A view of the thermocouples (TC) inserted into the Tylose brick at various locations (dimensions in mm)

Figure 2.18: The Tylose brick

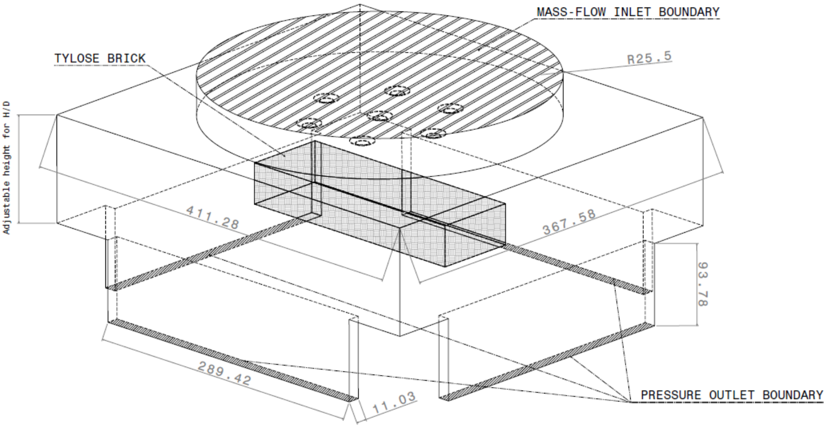

Figure 2.19: A scheme of the configuration used for the experiments with the Tylose brick (dimensions in mm).

cesses: Alfaifi et al. (2014) introduce a *Uniformity Index* (UI) defined in equation (2.5), where T_{av} is the average temperature of the food item of volume V, which is at T_0 at the beginning of the process.

$$UI = \frac{\int_V \sqrt{(T - T_{av})^2} dV}{V(T_{av} - T_0)} \tag{2.5}$$

The index is particularly useful at the end of the thawing process, since at the beginning the condition $T_{av} = T_0$ yields a singularity that prevents its use.

Y. Li et al. (2018) modify the UI, introducing the *Simulated Temperature Uniformity Index* (STUI), which describes the temperature deviation inside the food item from the target set-point temperature T_{tg} and it is described in equation (2.6).

$$STUI = \frac{\int_V |(T - T_{tg})| dV}{V(T_{tg} - T_0)} \tag{2.6}$$

The indexes (2.5) and (2.6) are introduced to study the effects of the Radio Frequency technology in thawing processes, in particular to verify the uniformity at the end of the heating process, consequently they do not consider the thermal history of the process.

In the present work we want to have information of the performance of the system during all the thawing process, consequently we propose three new indicators that provide information about:

- the temperature uniformity within the food item during the thawing process;
- the risk of developing bacteria due to localized, overheated zones;
- the time necessary to complete the process.

The first indicator has been called *Transient Uniformity Indicator* and it is defined in equation (2.7). It is defined combining the equations (2.5) and (2.6). As it is, the indicator has to be minimized to have a uniform thawing process.

$$TrUI = \frac{\int_V \sqrt{(T(x,y,z,t) - T_{av}(t))^2} dV}{V(T_{tg} - T_0)} \tag{2.7}$$

The second indicator is the *Safety Risk Indicator*, defined in (2.8): it provides information about the safety thresholds that must be respected to prevent bacteria proliferation. In particular bacteria proliferation is considered *potentially dangerous* when the food attains *critical* temperature conditions for a *long* period of time. Generally these conditions are strongly dependent on the type of food, anyway in Food-Safety (2017) there are some references related to a *Dangerous Zone*, defined as the condition in which potentially hazardous food is left for more that 3-4 hours at a temperature between 4 °C and 46 °C (in some cases the proposed upper limit is increased to 57 °C).

$$SRI = \frac{1}{V}\int\limits_{V} g\left(\int\limits_{0}^{t} g(T(x,y,z,t) - T_{safe})dt - \tau_{max}\right) dV \tag{2.8}$$

where

$$g(x) = \begin{cases} 0 & \text{if} \quad x \leq 0 \\ 1 & \text{if} \quad x > 0 \end{cases}$$

SRI can be interpreted as a sort of *mean safety gap* for the brick. This indicator can be used to calibrate the parameters governing the thawing process in order to maximize the thawing rate while at the same time ensuring the food safety. In particular this indicator is bounded above by 1, a value attained when all the material spent more than τ_{max} above the safety threshold T_{safe}. Consequently we have to keep this index as close to 0 as possible to prevent safety issues.

The third indicator gives information about both the productivity of the machine and the quality of the thawing process (Eastridge and Bowker (2011)). It is called *Velocity Indicator* and it is defined as the time in which the minimum temperature (calculated as volume average for a volume corresponding to the 5% of the total volume) reaches 0 °C: the threshold of 0 °C is suggested by James et al. (1976) to avoid any presence of ice inside the food.

2.3.5 Numerical models

This chapter describes the numerical methodology developed for the investigation of the jet impingement technology for professional appliances. In particular the method consists of two consecutive steps where two different computational models are combined in cascade. In the first step a CFD model is used to describe the thermofluid-dynamic interaction between the fluid flow and the solid item, in conjugate heat transfer; in particular the aim of this model is to evaluate the distribution of the Nusselt coefficient on the surface of the item. In particular, the CFD model is used only to describe some seconds of the thawing process, in which the Nusselt number gradually settles on a stationary value. The CFD model is computationally expensive, thus the distribution of the Nusselt number is used as boundary condition for a FDHCM, which solves only the energy equation and describes the transient thermal field within the item. This strategy allows to describe in a computationally-efficient way the performance of the jet impingement technology and, at the same time, permits to deal with advanced design optimization.

2.3.5.1 CFD model

The CFD model STARCCM+® is used to solve the thermofluid-dynamic equations that describe the behaviour of the fluid flow and the heat transfer between the fluid and the solid objects present in the test chamber.

As preliminar analysis, we have developed a numerical CFD model to reproduce the fluid field of a single jet. This study is propedeutic for the choice of the turbulence model and the mesh size distribution. Cooper et al. (1993) report an extensive set of measurements for a turbulent jet impinging orthogonally on a large plane surface (figure 2.20). They provide results for several nozzle-to-plate distances and radial distances from the stagnation point. In all the experiments the air flows through a sharp-edged pipe nozzle to have a fully developed flow at the exit of the nozzle. The computational mesh and the turbulence model are selected by comparing the vertical profiles of the simulated and experimental velocity magnitudes (figures 2.24a and 2.22), for a given nozzle-to-plate distance H/D and at two different values of the radial distance (r/D=1.5 and r/D=2) from the stagnation point, marked in blue and green respectively in figure 2.20. The mesh sensitivity analysis permits to select the best mesh distribution, in terms of number of prism layers and cell sizes. In particular the mesh size is refined in the jet and free-jet zones (1,5 mm as characteristic length), in the zones near the wall (1,2 mm as characteristic length) and at the wall with 10 layers of prisms with a total thickness of 0,7 mm. When it comes to the description of the thermo-fluid dynamic of jet impingement flows, the choice of the turbulence model is a fundamental step: LES models have a good ability to capture the turbulent structures and their effect on the thermal field (Taghinia et al. (2014) and Bovo and Davidson (2015)), however they are quite computationally-expensive. RANS two-equations models represent a valid alternative every time that the complexity of the problem requires a computationally-efficient solution: in literature, several authors remark the ability of the $k-\varepsilon$ models to reproduce the jet impingement flow field (Ryfa et al. (2012) and D. Singh et al. (2013)), but at the same time the $k-\omega$ (especially in the Menter SST version, Pope (2000)) is found to be very suitable in reproducing the heat transfer at the stagnation point and in the wall jet region (Hofmann et al. (2007) and Zuckerman and Lior (2006)). Three turbulence models are compared

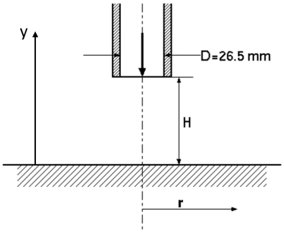

Figure 2.20: The geometry of the Cooper's model

(using the mentioned mesh size), namely the *Standard* $k - \varepsilon$ model, the *Realizable* $k - \varepsilon$ model and the $SST\, k - \omega$ model. The $SST\, k - \omega$ turbulence model yields significantly more accurate results than the *Standard* $k - \varepsilon$ or the *Realizable* $k - \varepsilon$ turbulence models. In the present work the $SST\, k - \omega$ turbulence model is used.

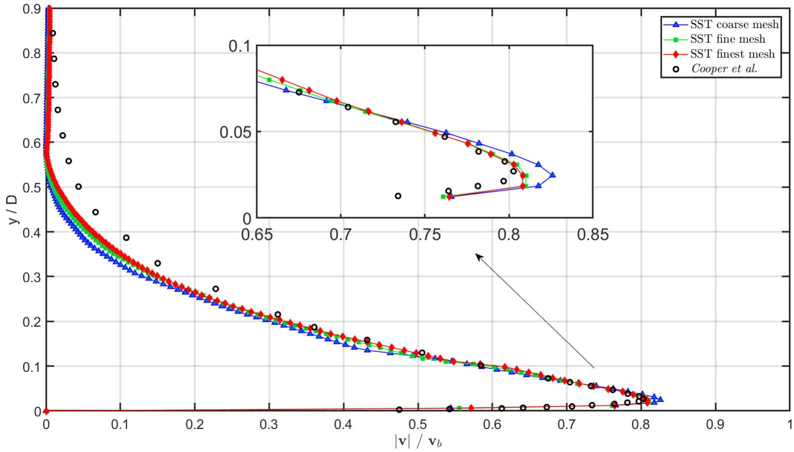

Figure 2.21: Mesh size sensitivity analysis for H/D=6 and r/D=1.5. The coarse mesh comprises 290 000 polyhedral cells, the fine mesh 530 000 cells and the finest 2 000 000 cells.

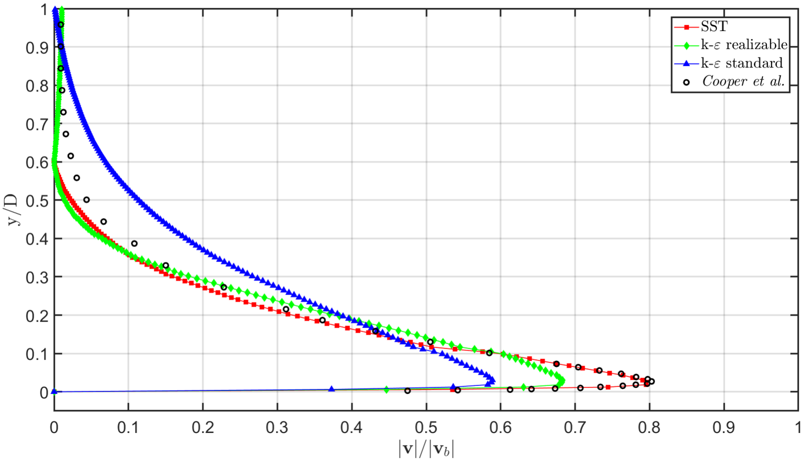

Figure 2.22: Sensitivity analysis with respect to the turbulence model, for H/D=6 and r/D=2.

After the choice of a mesh size distribution and the turbulence model, we have developed the model for our specific case. The test chamber of the test rig represents the computational domain (figure 2.19 and figure 2.23). The computational domain is discretized by an unstructured polyhedral mesh, with about two millions cells. The mesh at the wall under the jets is refined with ten prism layers with a total thickness of 4.5% of the nozzle diameter (figure 2.24b) and it is refined also at the nozzle and at the free-jet region where the target cell size is 10% of the jet diameter.

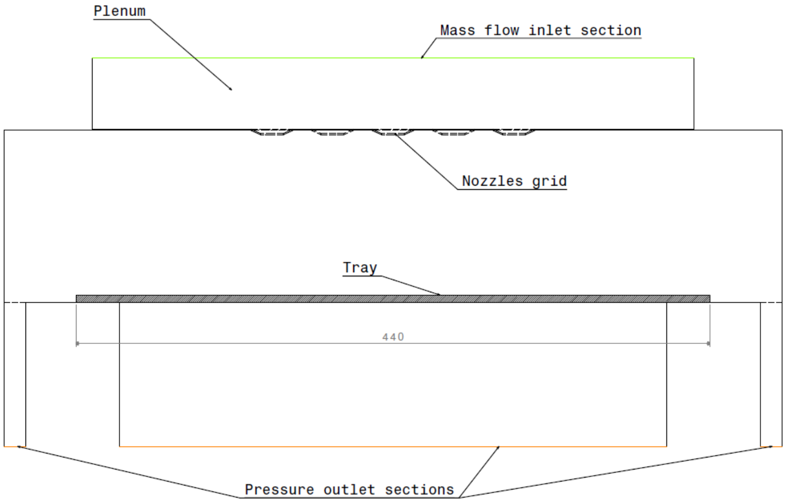

Figure 2.23: A visualization of the midsection of the test chamber with the boundary conditions indicated.

The governing equations are solved in transient state; here we report the set of RANS equations for incompressible flow of a Newtonian with constant viscosity, where the capital letters and the prime refer to the mean and fluctuating

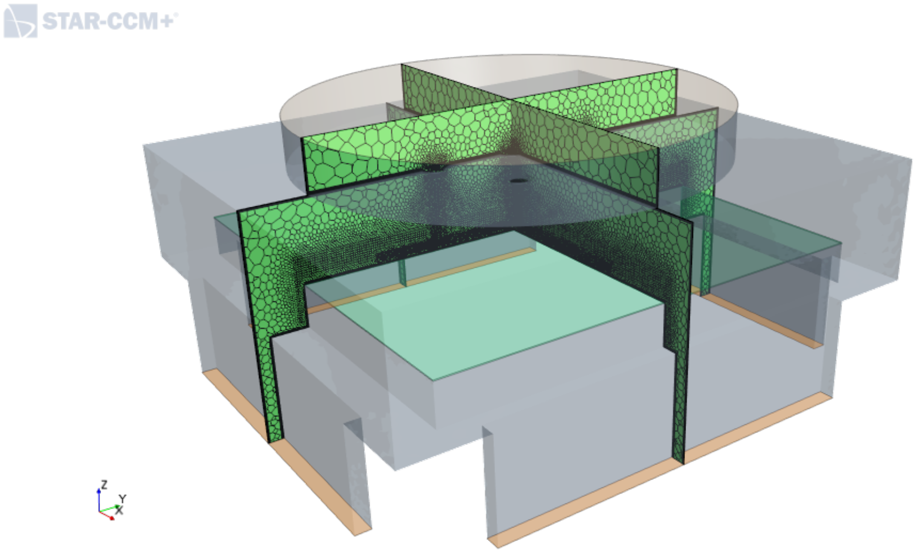

(a) A view of the mesh used in the simulations.

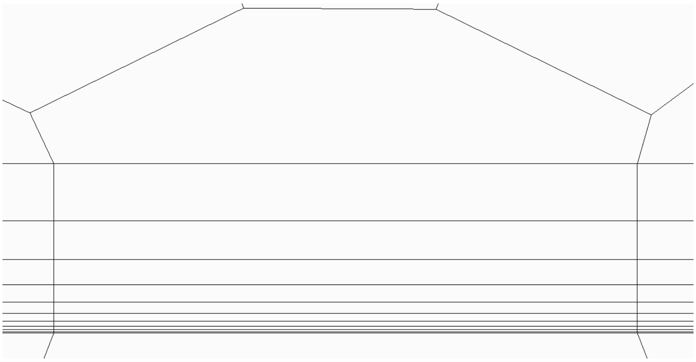

(b) A detail about the prism layers

Figure 2.24: The mesh

components of the Reynolds decomposition (e.g. $u = U + u'$):

$$\begin{aligned}
&\nabla \cdot (\mathbf{U}) = 0 \\
&\frac{\partial U}{\partial t} + \nabla \cdot (U\mathbf{U}) = -\frac{1}{\rho}\frac{\partial P}{\partial x} + \nu \nabla \cdot (\nabla U) + \frac{1}{\rho}\left[\frac{\partial(-\rho\overline{u'^2})}{\partial x} + \frac{\partial(-\rho\overline{u'v'})}{\partial y} + \frac{\partial(-\rho\overline{u'w'})}{\partial z}\right] \\
&\frac{\partial V}{\partial t} + \nabla \cdot (V\mathbf{U}) = -\frac{1}{\rho}\frac{\partial P}{\partial y} + \nu \nabla \cdot (\nabla V) + \frac{1}{\rho}\left[\frac{\partial(-\rho\overline{u'v'})}{\partial x} + \frac{\partial(-\rho\overline{v'^2})}{\partial y} + \frac{\partial(-\rho\overline{v'w'})}{\partial z}\right] \\
&\frac{\partial W}{\partial t} + \nabla \cdot (W\mathbf{U}) = -\frac{1}{\rho}\frac{\partial P}{\partial y} + \nu \nabla \cdot (\nabla W) + \frac{1}{\rho}\left[\frac{\partial(-\rho\overline{u'w'})}{\partial x} + \frac{\partial(-\rho\overline{v'w'})}{\partial y} + \frac{\partial(-\rho\overline{w'^2})}{\partial z}\right] \\
&\frac{\partial \Phi}{\partial t} + \nabla \cdot (\Phi\mathbf{U}) = \nabla \cdot (\Gamma_\Phi \, \nabla \Phi) + \left[\frac{\partial(-\overline{u'\phi'})}{\partial x} + \frac{\partial(-\overline{v'\phi'})}{\partial y} + \frac{\partial(-\overline{w'\phi'})}{\partial z}\right] + S_\Phi
\end{aligned} \tag{2.9}$$

where Φ is a generic scalar (e.g. total energy per unit mass). Air is treated as an ideal gas, with constant thermophysical properties. The Reynolds-stresses and Reynolds-fluxes pose a closure problem, that is resolved by relating these quantities to the mean velocity and mean scalar concentration via model assumptions. The $SST\, k - \omega$ model (equations (2.10)) is used in the present work.

$$\begin{aligned}
&\frac{\partial \rho k}{\partial t} + \nabla \cdot (\rho k \mathbf{U}) = \nabla \cdot \left[\left(\mu + \frac{\mu_t}{\sigma_k}\right)\nabla(k)\right] + P_k - \beta^* \rho k \omega \\
&\frac{\partial \rho \omega}{\partial t} + \nabla \cdot (\rho \omega \mathbf{U}) = \nabla \cdot \left[\left(\mu + \frac{\mu_t}{\sigma_{\omega,1}}\right)\nabla(\omega)\right] + \gamma_2 \left(2\rho S_{ij} \cdot S_{ij} - \frac{2}{3}\rho\omega \frac{\partial U_i}{\partial x_j}\delta_{ij}\right) \\
&-\beta_2 \rho \omega^2 + 2\frac{\rho}{\sigma_{\omega,2}\omega}\frac{\partial k}{\partial x_k}\frac{\partial \omega}{\partial x_k}
\end{aligned} \tag{2.10}$$

In equations (2.10) the Einstein nomenclature is used, the reader can find further details in Versteeg and Malalasekra (2007). The Menter $SST\, k - \omega$ model considers a hybrid modelling using: the $k - \omega$ modelling in the near-wall region and the $k - \varepsilon$ model in the fully turbulent region far from the wall. This new hybrid model maintains the good performance of the $k - \varepsilon$ model in the free stream (because it is less sensitive to the arbitrary assumed values) and the good performance of the $k - \omega$ model for boundary layers with adverse pressure gradients (Versteeg and Malalasekra (2007)).

In the plenum the airflow tends to have a uniform, undisturbed velocity profile, thus it seems convenient to define in an orizontal section placed within the plenum an inlet section where a *mass flow inlet* boundary condition is assigned. Empirical correlations for pipe flows, reported in equations (2.11), can be used to define the turbulence boundary conditions at the inlet section in terms of *turbulence* *intensity,* I_t and *length scale, l*. These values are used to estimate k and ω on the inlet boundary (Versteeg and Malalasekra (2007)).

$$\begin{aligned}
I_t &= 0.16\,(\mathrm{Re}_{D_h})^{-1/8} \\
l &= 0.07\,D_h \\
k &= \tfrac{3}{2}(I_t v)^2 \\
\omega &= \tfrac{\sqrt{k}}{L(\beta^*)^{1/4}}
\end{aligned} \tag{2.11}$$

where v is the local velocity magnitude and β^* is a $SST\,k-\omega$ coefficient.

At the outlet section a *pressure outlet* boundary condition is assigned, which consists in giving a pressure condition and all the other scalars are reconstructed by the gradients; this section is defined at 100 mm downstream the tray to minimize the influence of this condition on the test chamber and to avoid reversed flows.

The *no-slip* condition is used for the velocity components at solid walls, with the *all y+* wall treatment: it is a hybrid treatment that emulates the *low Re* wall treatment for finer meshes and the *wall function* wall treatment for coarser meshes (STAR-CCM+ (2017)). The walls of the test chamber are considered adiabatic, as they are insulated externally by a thick layer of low-conductivity material. Each solid item placed under the array of jets is interested by heat conduction in its interior and by conjugate heat transfer with the fluid region on its surface. As initial conditions we assume that the air in the whole chamber is at rest and at uniform temperature and that each item is at constant uniform temperature. The SIMPLE algorithm (Patankar (1980)) is adopted to solve the pressure-velocity coupling, the 2nd order Upwind scheme is used to approximate the convective fluxes and the temporal scheme is 2nd order accurate(Versteeg and Malalasekra (2007)). The transient simulations are solved with a fixed time-step, derived from the Courant-Friedrichs-Lewy (CFL) condition with a lower limit to $5\ \cdot 10^{-4}$ s. The CFL condition is 1 on average within the computational domain.

2.3.5.1.1 Effect of the buoyancy forces

The buoyancy forces are not considered in the present work since their effect is negligible on the results, as confirmed by CFD simulations adding the buoyancy term to the model. In figure 2.25 the temporal profile of the Nusselt number at a stagnation point is reported for the simulation with the buoyancy term activated and for the simulation without the buoyancy term. The buoyancy term doesn't have any influence on the Nusselt number profile, as it can be seen in details in figure 2.26.

The buoyancy forces are the responsible of the natural convection, a thermal mechanism that is dependent on the temperature differences within the fluid domain. In particular since the temperature of the solid object varies in time, the intensity of natural convection varies as well. In the present case the forced

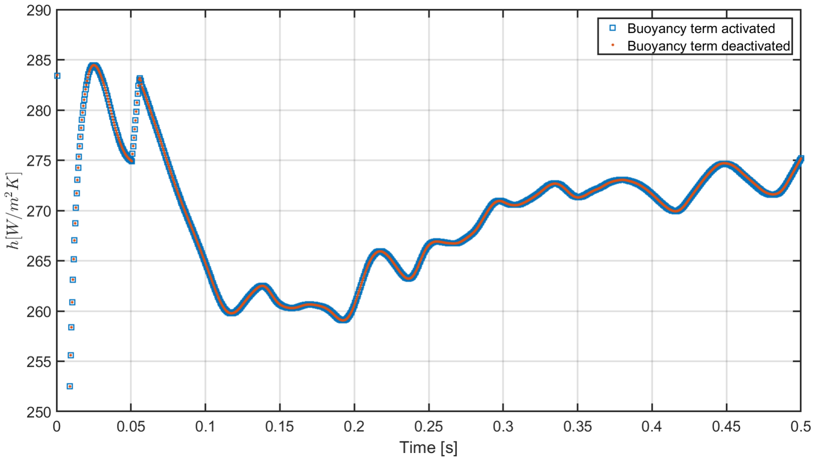

Figure 2.25: Influence of the buoyancy forces on the convective heat transfer coefficient profile, for Re=21000 and H/D=5.

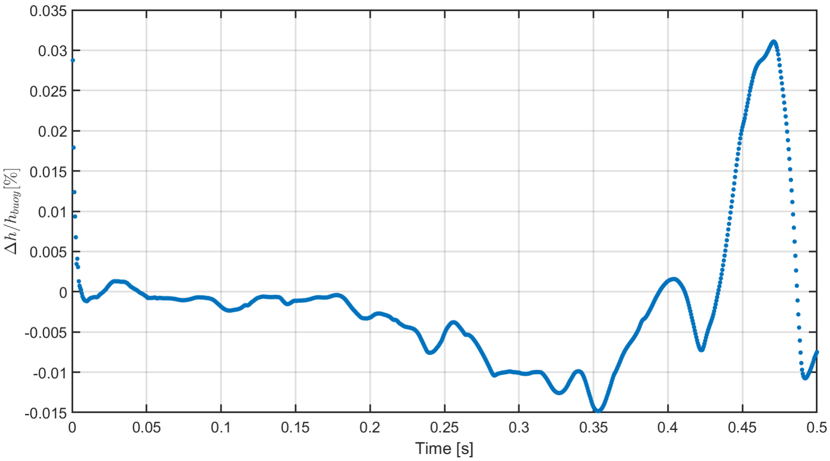

Figure 2.26: Convective heat transfer coefficient difference between the simulation with the buoyancy term activated and deactivated, for Re=21000 and H/D=5.

convection is predominant on the natural convection and this result is crucial to permit the study of the distribution of the heat transfer coefficient at the beginning of the process and to keep the distribution constant over the time till the end of the process, as found by other researchers (Kim and Camci (1995)). This result can be confirmed also by calculating the Richardson number, defined in (2.12): if $Ri > 10$, the natural convection dominates respect to the forced convection, if $0.1 < Ri < 10$ the mixed convection occurs and both the natural and the forced convection need to be taken into account, if $Ri < 0.1$ the forced convection dominates (Bejan (2004)).

$$\begin{aligned}
Ri &= \frac{Ra}{Pr\,Re^2} \\
Ra &= \frac{\beta g L^3 (T_\infty - T_w)}{\nu\alpha} \\
Re &= \frac{|\mathbf{v}|_\infty D}{\nu} \\
Pr &= \frac{\nu}{\alpha} \\
Nu &= \frac{hD}{\lambda} = \frac{q_w D}{\lambda(T_\infty - T_w)}
\end{aligned} \tag{2.12}$$

For the Rayleigh number we consider as characteristic length L the maximum height of the chamber (L=0.13 m), all the fluid properties calculated at $(T_\infty + T_w)/2$ and we consider the Reynolds number Re calculated as in (2.12): the maximum value of Ri (calculated for the lower Re number of 17000 and for the highest temperature difference $\Delta T = 28K$) is 0.038. In (2.12) we define also the Nusselt number, considering the nozzle diameter D as characteristic length and the jet inlet temperature as reference temperature.

2.3.5.2 FDHCM

After the CFD model the Nusselt number distribution is used as boundary condition of a simpler numerical model. In particular the Nusselt number distribution is calculated by the CFD model for each configuration of H/D and with the presence of the item within the computational domain with the Conjugate Heat Transfer method. The H dimension is calculated as the minumum vertical distance between the exit section of the jets and the surface of the item. In each simulation with the simpler model the boundary condition of the heat transfer coefficient is always calculated numerically. For the purpose, a 3-D explicit finite difference model is developed to describe the thermal behaviour of the solid item. The volume of the item is represented by a 3D uniform Cartesian grid, and each node is representative of a small portion of material. Each internal node communicates with the others by means of conductive resistances, while the superficial nodes exchange heat flux also with the surroundings by means of convective heat transfer and radiation heat transfer (if the radiation flux is relevant). The pertinent governing equation with boundary conditions is

$$
\begin{aligned}
&\frac{\partial(\tilde{H})}{\partial t} = \nabla\cdot(\lambda\nabla(T)) \\
&\lambda(T)\frac{\partial T}{\partial x}\Big|_{x=x_{min}} = h_{x_{min}}(T(x_{min},y,z,t)-T_\infty(t)) \\
&-\lambda(T)\frac{\partial T}{\partial x}\Big|_{x=x_{max}} = h_{x_{max}}(T(x_{max},y,z,t)-T_\infty(t)) \\
&\lambda(T)\frac{\partial T}{\partial y}\Big|_{y=y_{min}} = h_{y_{min}}(T(x,y_{min},z,t)-T_\infty(t)) \\
&-\lambda(T)\frac{\partial T}{\partial y}\Big|_{y=y_{max}} = h_{y_{max}}(T(x,y_{max},z,t)-T_\infty(t)) \\
&\lambda(T)\frac{\partial T}{\partial z}\Big|_{z=z_{bottom}} = U_g(T(x,y,z_{bottom},t)-T_\infty(t)) \\
&-\lambda(T)\frac{\partial T}{\partial z}\Big|_{z=z_{top}} = h_{z_{top}}(x,y)(T(x,y,z_{top},t)-T_\infty(t)) \\
&T(x,y,z,0) = T_0
\end{aligned}
\tag{2.13}
$$

The model considers half-in-size volume elements at the surface, quarter-in-size volume elements at the edge and eighth-in-size volume elements at the corners (Chau and Gafney (1990) and Erdogdu and R. Singh (2005)). The set of equations used in the model is reported in (2.13). The discretization schemes are retrieved from the traditional finite-difference methods, described in details in Grossmann and Roos (2007). The set of discretized equations is written and solved in Matlab$^{\text{TM}}$ R2017b. The mesh is refined near the surfaces in contact with the fluid (typically a reference size of 0.001 m is used). The mesh size sensitivity analysis is reported in figure 2.27.

The time-step is set according to the stability criterion $\frac{\alpha\Delta t}{\Delta z^2} \leq \frac{1}{2}$, where Δz is the minimum spatial difference between the nodes of the mesh. On the interface between the fluid and the solid item the convective boundary condition is used: the spatial variation of the convection coefficient h is retrieved from the CFD model by interpolating locally the values for each surface node. On the bottom surface, in contact with the tray, a uniform global heat transfer coefficient is used, considering the conductivity of the tray on which the food item lies and a constant convective coefficient for the air below the tray. The model doesn't take into account mass transfer equations: as described in §2.3.4, during heating and cooling processes the food can exchange mass with the surroundings due to evaporation or condensation phenomena and mass diffusion in the food structure. This effects, known as *food weight-loss*, might affect the temperature distribution within the item: therefore, each food item is wrapped into a thin layer of plastic film to limit its transpiration and preserve the validity of a heat conduction model.

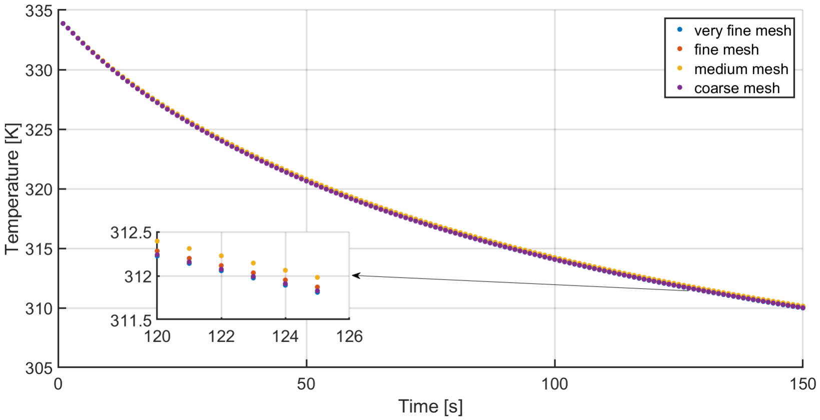

Figure 2.27: Mesh size independence analysis for the FDHCM, the reference size is: 0.004 mm for the coarse mesh, 0.003 mm for the medium mesh, 0.002 mm for the fine mesh and 0.001 mm for the very fine mesh.

2.4 Results and discussion

2.4.1 Validation of the design procedure

2.4.1.1 Velocity field

In the first simulations the CFD model has been tested to reproduce the velocity field which develops within the test chamber without the presence of solid items. Numerical and experimental velocity profiles along the jet axis are compared for the geometry shown in figure 2.28a. The experimental measurements are taken by a single-wire, hot-wire anemometer. The study of the deceleration region is very important because in this zone the interactions between the jet and the fluid at rest extend throughout the center of the jet: the shear layer, that is generated by this interaction, is the primary source of large, turbulent eddies (Zuckerman and Lior (2006)).

In figure 2.28a the array of nozzles used for the experiments is shown. The measurements with the hot wire anemometer have been carried out along the axis of the three jets marked in red. The wire is placed orthogonally to the direction of the velocity vector (supposed in this region to be along the z axis, figure 2.28b). The nozzle-to-plate distance is H/D=5 and the measurements have been acquired up to z/D=3.5 with 20°C as operating temperature of the jets. Particular care is required to keep the temperature of the jets constant, as the temperature of the airflow tends to increase due to the internal heat generation by friction that is produced in the blower; thus the chiller has been used to keep the temperature

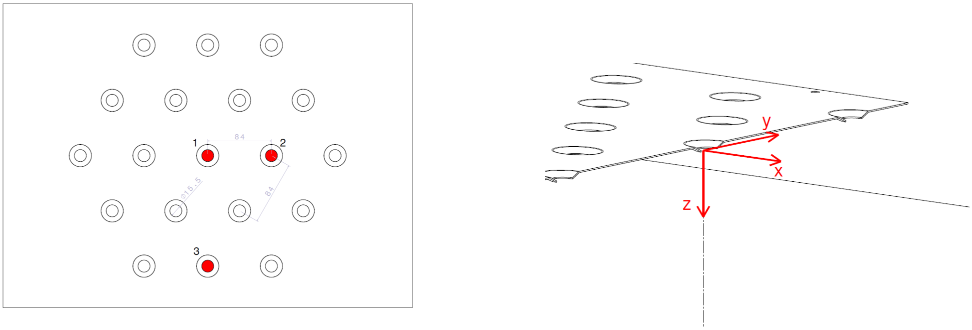

(a) A view of the nozzle array used for the fluid-dynami study: in the array the configuration of the active nozzle is reported; the nozzle analysed with the anemometer are marked in red.

(b) Reference system for the hot wire measurements

Figure 2.28: Geometric details for the hot wire measurements

stable at 20°C. The choice to limit the measurements to the mentioned region is motivated by the uncertainty of the flow direction in the stagnation region, due to the presence of cross-flow from the adjacent jets. In figures 2.29, 2.30 and 2.31 the comparison between numerical and experimental data is shown, the whole profile of velocity is scaled with the velocity at the nozzle exit. Each experimental result is obtained by three repeats (N=3) and the error is calculated by the *t-Student* approach with *two-side* 95% confidence level. The statistical approach with the *t-Student* is widely used when few repeats can be done: in this case 2 degrees of freedom (DOF) are present (DOF=N-1), thus the standard deviation calculated (which is typically used for normal distribution) needs to be corrected with the Student parameter t=4.3 for a confidence interval equal to 95%, and the error relative to the measurement can be described by $\pm t\sigma$, where σ is the standard deviation (Fisher (1925)). The potential core region is easily recognizable, and it ends between z/D=2 and z/D=3 where the velocity starts to decay and reaches the 95% of the value at the nozzle exit (Zuckerman and Lior (2006)). The agreement between numerical and experimental data is good, especially up to z/D=3; the higher mismatch at z/D=3.5 could be an indication of the arise of flow instabilities and fluctuations, which affect the axial measure by a single-wire anemometer.

2.4.1.2 The cross-flow effect

In confined, multi-jet impingement the cross-flow influences the flow field and consequently the heat transfer mechanism. In figure 2.32 the velocity iso-surfaces relative to 15 m/s are plotted in gray color: the typical deformation induced by cross-flow streams is evident and it is relevant near the stagnation region, as

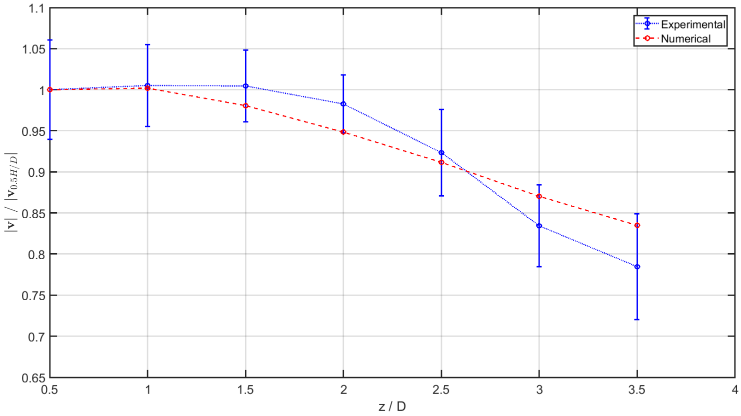

Figure 2.29: Comparison between numerical and experimental data for the nozzle 1, at Re=21000

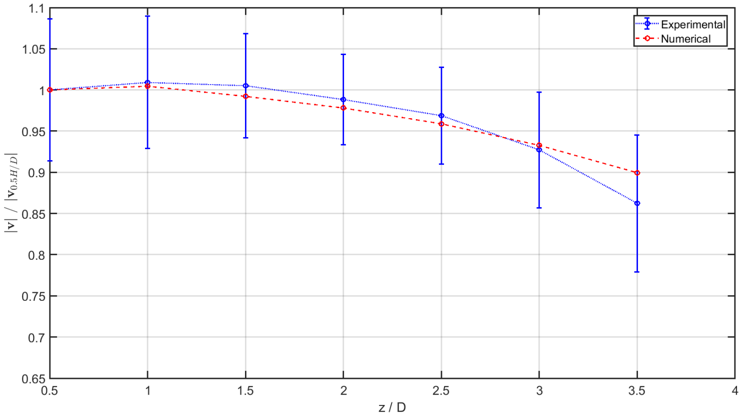

Figure 2.30: Comparison between numerical and experimental data for the nozzle 2, at Re=21000

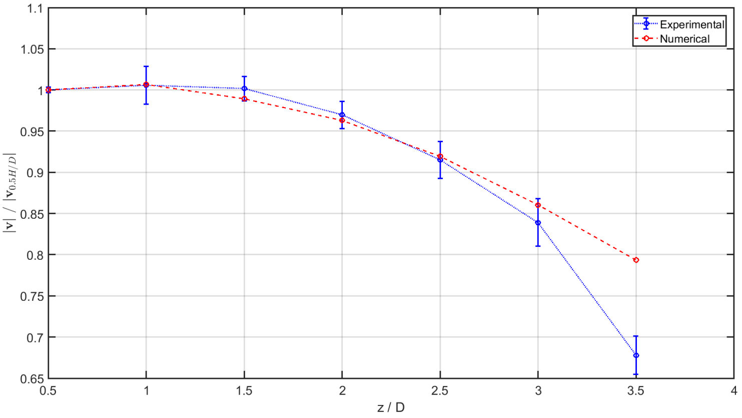

Figure 2.31: Comparison between numerical and experimental data for the nozzle 3, at Re=21000

confirm of the difficulties found in the data sampling with the anemometer. This deformation in the shape of the jet flow is clearly visible also on the Nusselt number distribution (figure 2.33), where the iso-lines of the heat flux at the stagnation region are not regular and rounded (as for single rounded jet flow).

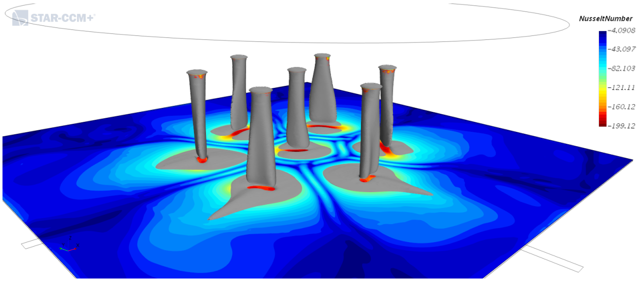

Figure 2.32: Velocity iso-surfaces representation for Re=23000 and H/D=5

In figure 2.33 the effect of the interaction between the wall jet streams is evident from the presence of secondary peaks of the Nusselt number.

2.4.1.3 Nusselt distribution

The heat transfer mechanism between the airflow and the solid object has been investigated by the comparison of experimental and numerical values of the Nusselt number. The micro-calorimeter technique, described in §2.3.3, has been used to calculate the distribution of the Nusselt number. The CFD model takes

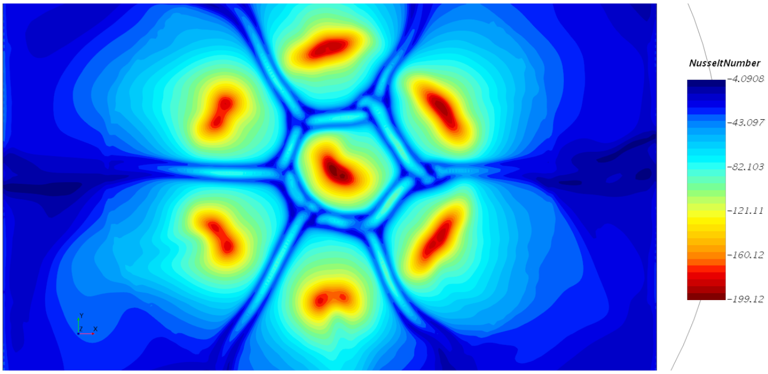

Figure 2.33: Nusselt number distribution for Re=23000 and H/D=5

into account the presence of seven jets for the array as a compromise between computational weight of the model and presence of interaction between adjacent jets.

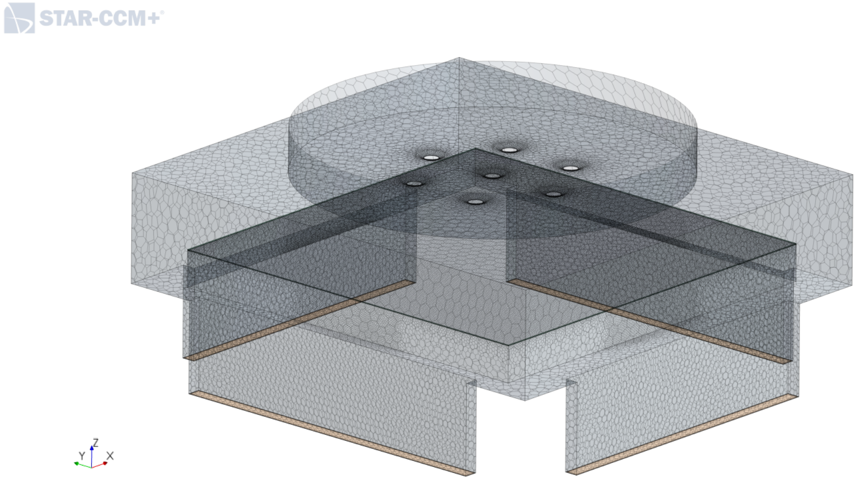

Figure 2.34: A view of the superficial mesh used for the simulation, at the center of the figure the array of seven jets is easily recognizable.

In figures 2.36 and 2.37 the comparison between the numerical and experimental Nusselt number distributions is shown. The numerical Nusselt number at each location is the result of the time average operation when the profile reaches stability (figure 2.35); in particular the average is made on a time interval of 4-5 resident time of a fluid particle within the test chamber. The temporal profile of the Nusselt number is characterized by a steep rise, gradually settling on a stationary value, as found by other researchers (Kim and Camci (1995)).

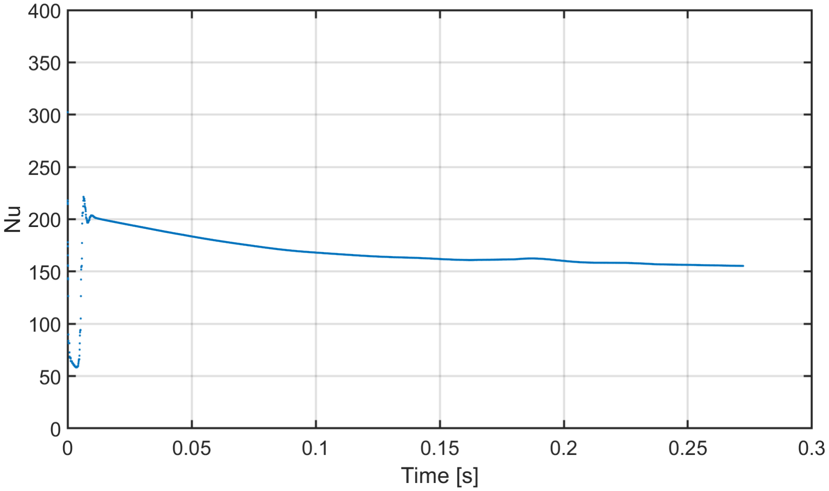

Figure 2.35: A view of a local Nu time-dependent profile on the solid surface below the array of jets.

For both the Reynolds numbers the average relative error between numerical and experimental results is about 20% (see table 2.1). This value is considered acceptable and in line with the uncertainty of the measurement technique of heat transfer coefficients with transient methods (the typical range of error reported in literature is from 10% to 15% at 95% confidence level, Sarkar and R. Singh (2003)). The error can be ascribed to two main factors: first of all, the change in weight and shape of each copper disk after the welding process of the thermocouples; then, epoxy insulating material is used to isolate laterally the thermocouples and to create the lumping system, but in the simulation the plate is considered uniform.

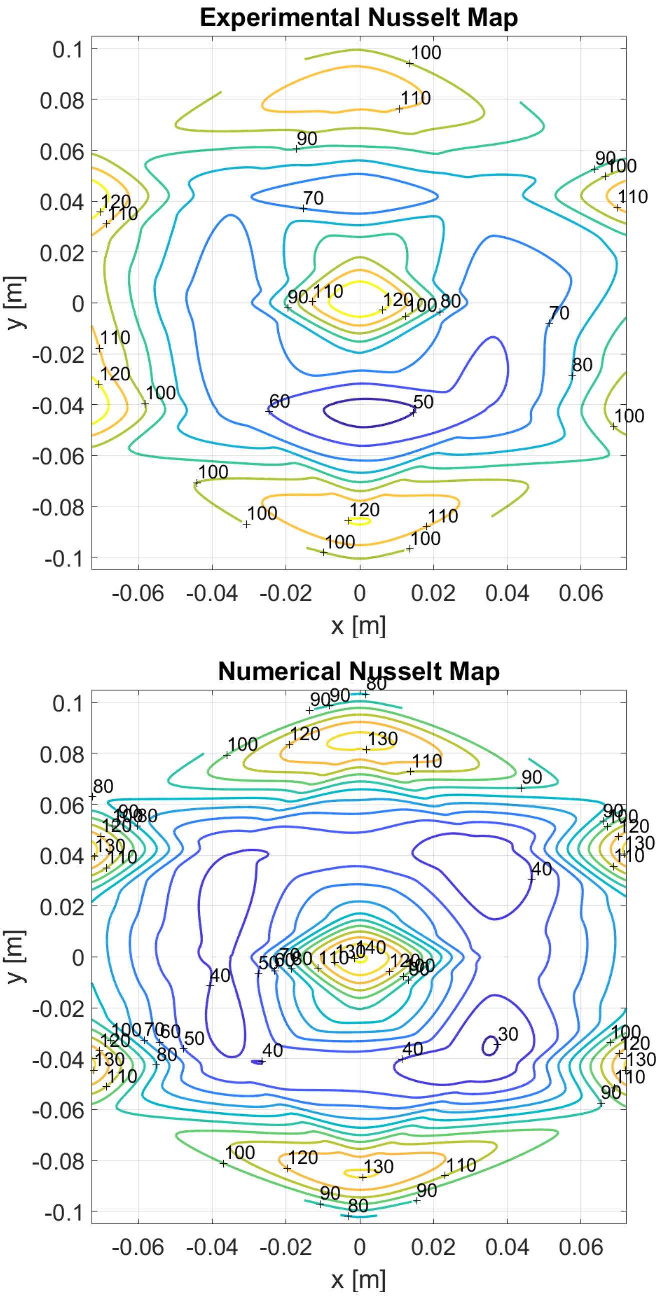

Figure 2.36: Nusselt maps for Re=16000

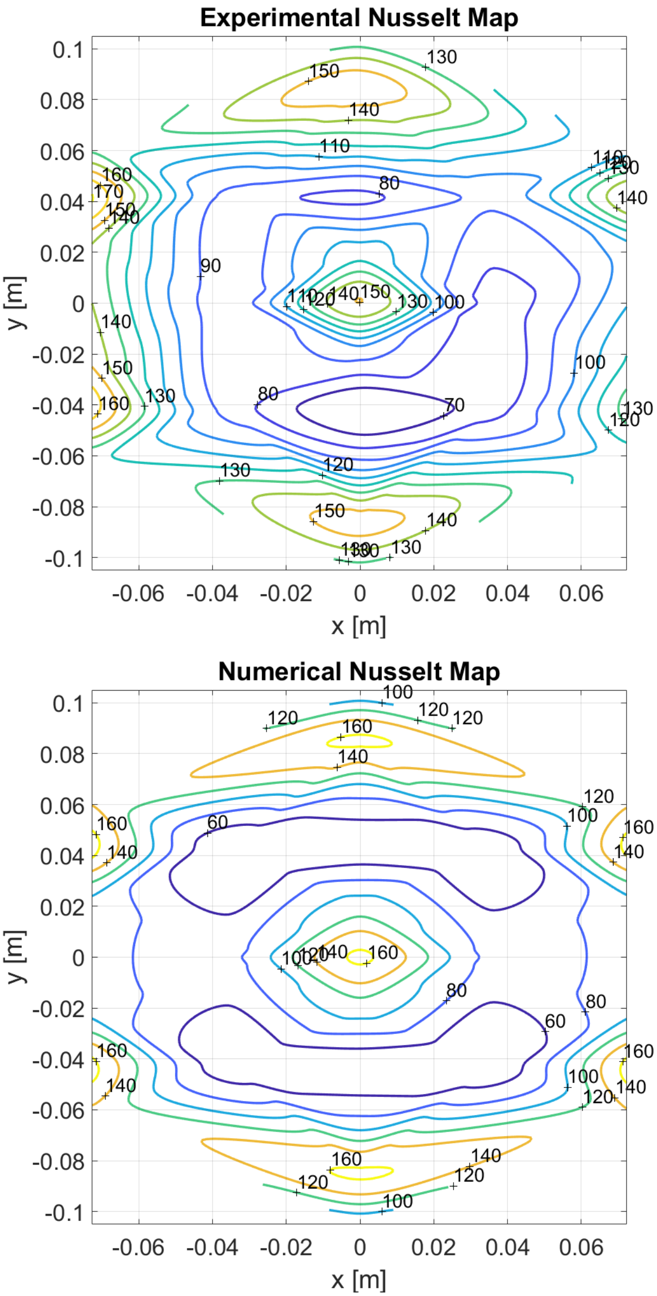

Figure 2.37: Nusselt maps for Re=21000

Nr. micro @Re=16000	Nu exp.	Nu num.	Nr. micro @Re=21000	Nu exp.	Nu num.
MC1	91.42±9.88	96.62	MC1	114.93±3.19	138.17
MC2	109.01±8.89	132.27	MC2	134.29±11.58	166.03
MC3	97.15±12.98	80.94	MC3	120.57±17.21	95.56
MC4	83.19±11.45	77.33	MC4	106.11±14.65	95.09
MC5	117.31±2.10	133.85	MC5	150.26±10.56	165.08
MC6	81.50±6.77	82.14	MC6	101.67±14.12	136.97
MC7	61.07±11.04	32.13	MC7	76.94±7.61	45.83
MC8	62.61±10.53	46.32	MC8	76.53±2.50	75.75
MC9	75.83±20.70	34.42	MC9	93.18±23.54	47.73
MC10	92.77±6.86	70.90	MC10	124.98±2.47	80.35
MC11	119.74±5.18	130.33	MC11	153.17±2.88	161.62
MC12	71.90±9.58	68.82	MC12	93.31±8.48	81.61
MC13	46.87±8.24	43.55	MC13	60.85±4.89	48.40
MC14	78.19±24.94	89.20	MC14	91.61±15.11	107.07
MC15	128.78±16.27	140.54	MC15	149.95±30.45	162.30
MC16	96.59±3.97	71.02	MC16	113.50±39.56	107.16
MC17	61.84±4.13	46.31	MC17	78.61±3.40	50.08
MC18	91.97±14.23	72.74	MC18	122.39±16.78	81.50
MC19	116.13±19.19	132.58	MC19	155.89±18.61	161.69
MC20	92.06±11.55	75.16	MC20	121.52±12.98	80.27
MC21	68.18±16.64	42.09	MC21	87.40±7.81	49.44
MC22	64.09±10.42	39.33	MC22	84.60±6.46	75.25
MC23	72.72±21.91	41.55	MC23	88.10±15.52	43.52
MC24	92.55±11.05	93.36	MC24	121.53±15.91	135.54
MC25	127.63±15.94	132.29	MC25	164.72±20.10	164.95
MC26	113.78±8.96	85.06	MC26	147.26±3.57	95.27
MC27	105.33±19.46	79.65	MC27	138.32±31.95	95.63
MC28	127.39±21.23	133.98	MC28	170.49±39.58	166.02
MC29	96.31±11.97	79.94	MC29	126.29±8.76	138.14

Table 2.1: Comparison between experimental and numerical Nusselt numbers. The micro-calorimeters are numbered as shown in figure 2.15. The errors are calculated considering three repeats and the *t-Student* approach, with *two-side* 95% confidence interval (DOF=2 and t=4.3).

2.4.1.4 Temperature distribution on the metal slab

As already mentioned, the calculated maps of Nusselt number are used to derive the temperature distribution within a target object, placed under the jet streams. We consider two test cases, where the targets are a metal slab and a Tylose brick respectively, in terms of temperature data. The metal slab is a very thin object with a high thermal diffusivity and a fast response, while the Tylose brick has a high thermal inertia. An array of seven jets is used for both test cases, as reported in figure 2.38 (where the seven nozzle projections are shown on the surface of the metal slab). The metal slab is heated by an external heating element up to 65°C, then the heating element is swiftly removed and the metal slab is cooled by the airflow from the jets down to 27°C. Eleven thermocouples, type-T (36 gauge, with ± 1°C accuracy in the range -200°C/350°C), are welded on the bottom surface of the slab, as reported in figure 2.38: the ones marked in red are exactly under stagnation points, the others are placed halfway between neighbouring stagnation points (hereinafter called *intermediate zones*).

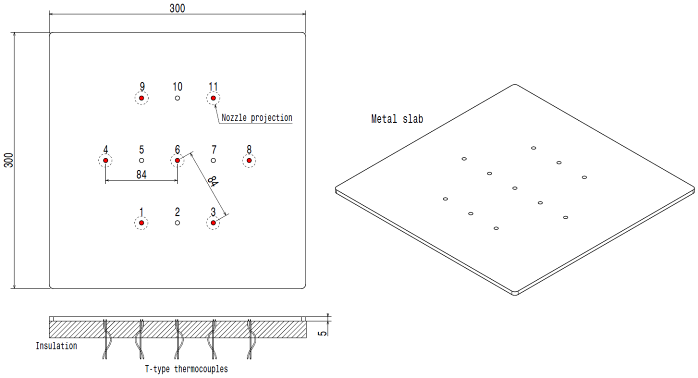

Figure 2.38: Metal slab assembly: the thermocouples located under the stagnation points are marked in red (dimensions in mm)

.

The metal slab is made of AISI 304 stainless steel ($\lambda = 17\,W/mK$, $\rho = 7800\,kg/m^3$ and $c = 480\,J/kgK$). In figures 2.40, 2.41, 2.42 and 2.43 the numerical and experimental dimensionless temperatures are compared. Each experimental graph is the result of three replicates. A good agreement is found both in the stagnation points and at the intermediate points and a noticeable difference is found looking at the cooling rates. This is strictly related to the importance of a detailed distribution of the Nusselt number, as the one shown in figure 2.39, related to Re=16000. It is interesting to consider how the results change if a constant heat transfer coefficient is used on the top surface of the FDHCM. In literature several semi-empirical correlations have been developed to describe the jet impingement heat transfer mechanism (Martin (1977) and Zuckerman and

Lior (2006)): typically for array of jets the correlations provide an average heat transfer coefficient. In the present work the Martin's correlation (Martin (1977)), explained in the set of equations (2.14), is used. This analysis is important to check if the error introduced by the averaging process of the distribution of the Nusselt number, by the use of the correlations, is acceptable, especially at the stagnation points.

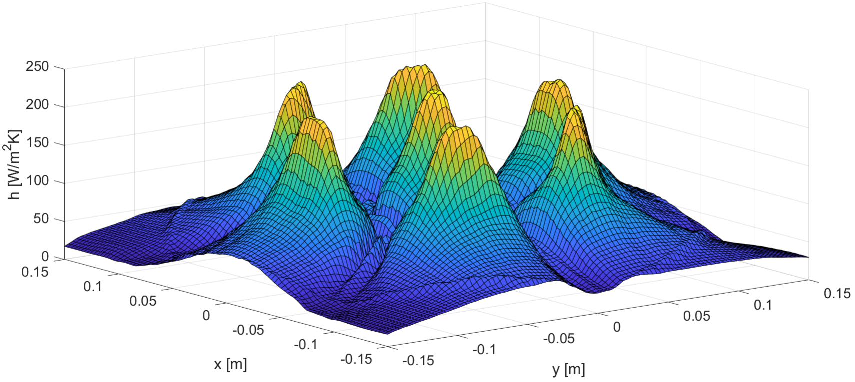

Figure 2.39: Map of heat transfer coefficients for Re=16000

.

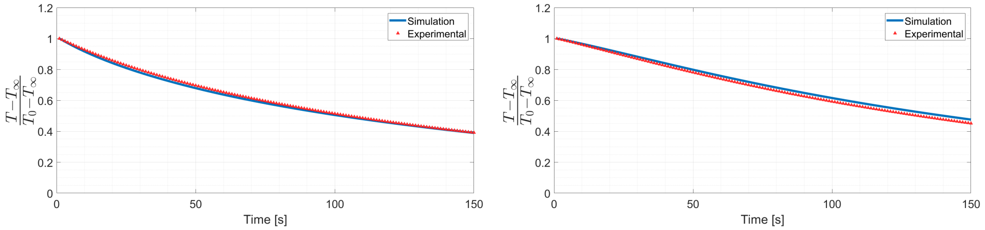

(a) TC1

(b) TC2

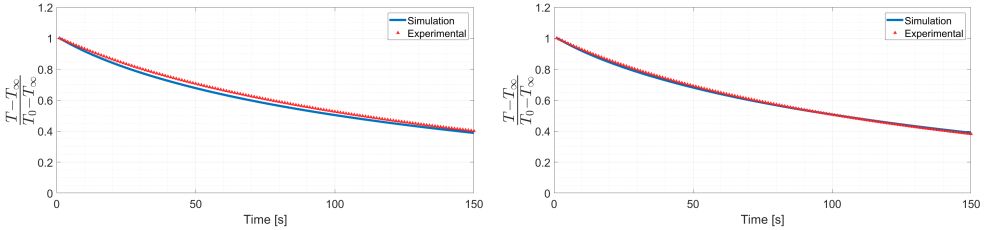

(c) TC3

(d) TC4

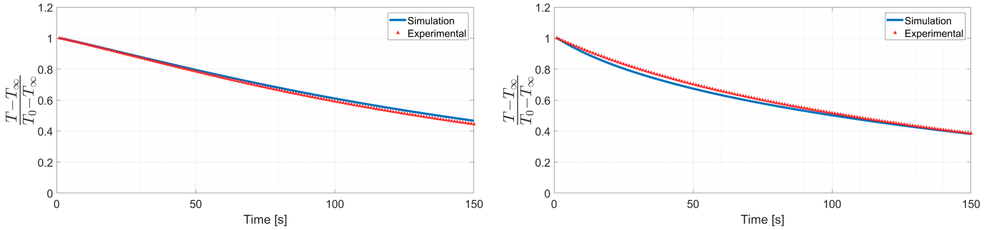

(e) TC5

(f) TC6

Figure 2.40: Comparison of experimental results versus model predictions of six locations for Re=16000

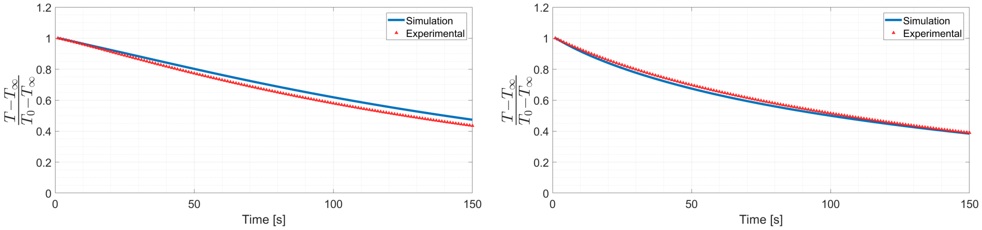

(a) TC7

(b) TC8

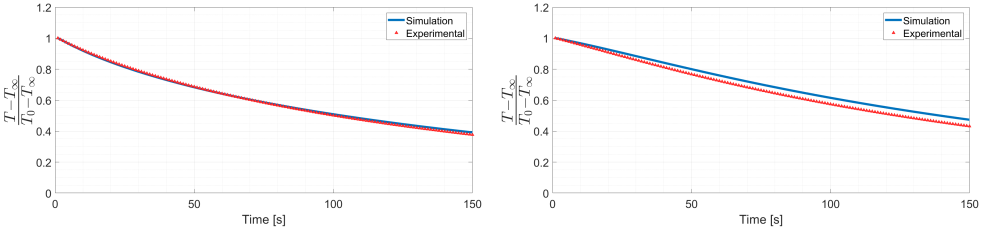

(c) TC9

(d) TC10

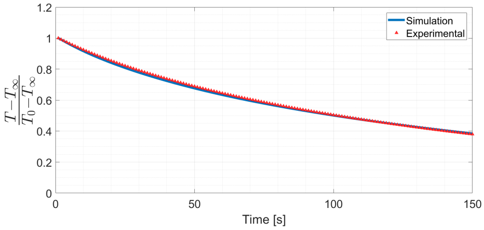

(e) TC11

Figure 2.41: Comparison of experimental results versus model predictions of five locations for Re=16000

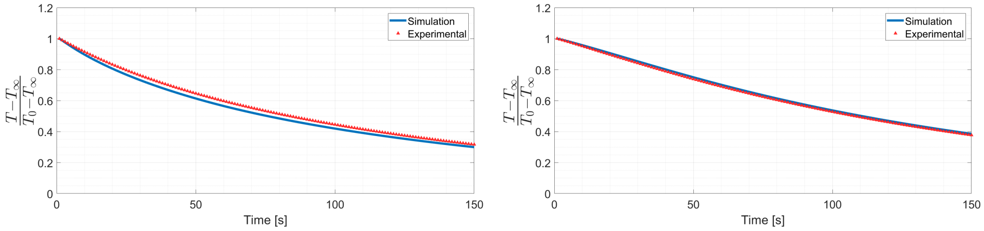

(a) TC1 (b) TC2

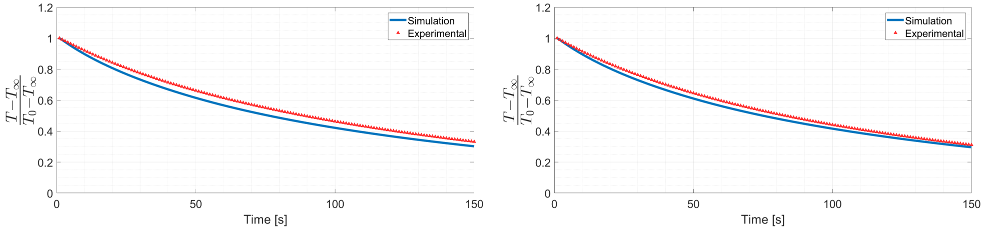

(c) TC3 (d) TC4

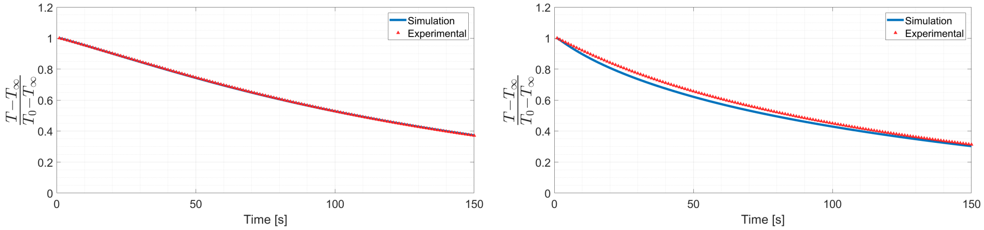

(e) TC5 (f) TC6

Figure 2.42: Comparison of experimental results versus model predictions of six locations for Re=21000

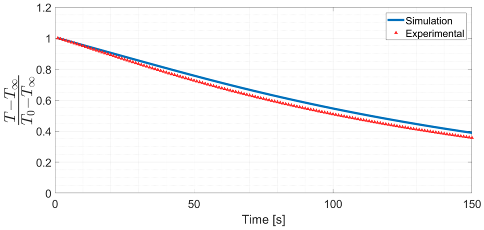

(a) TC7

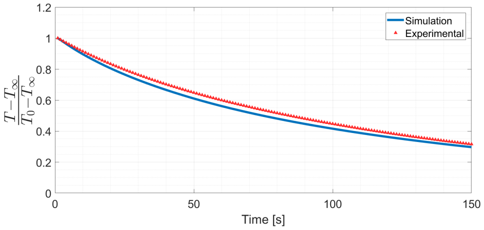

(b) TC8

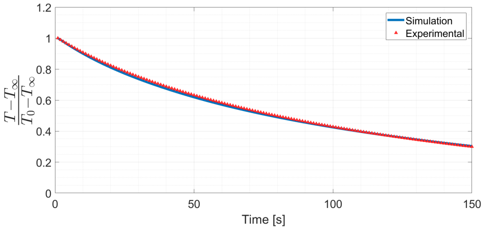

(c) TC9

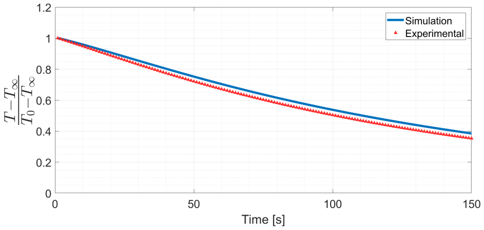

(d) TC10

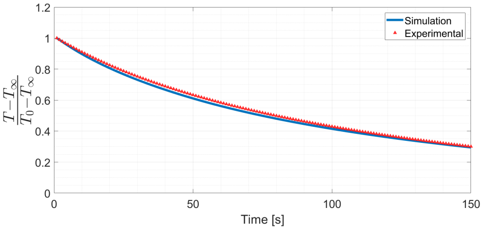

(e) TC11

Figure 2.43: Comparison between experimental and numerical predicted results of five locations for Re=21000

Source: Martin (1977)
Range of validity: $2000 < Re < 100000$, $0.004 \leq f \leq 0.04$ and $2 \leq H/D \leq 12$.
Equations:

$$\begin{cases} \overline{Nu} = Pr^{0.42} K(H/D, f) G(H/D, f) F(Re) \\ K = \left(1 + \left(\dfrac{H/D}{0.6/\sqrt{f}}\right)^{6}\right)^{-0.05} \\ G = 2\sqrt{f}\dfrac{1 - 2.2\sqrt{f}}{1 + 0.2((H/D) - 6)\sqrt{f}} \\ F = 0.5 Re^{2/3} \end{cases} \tag{2.14}$$

where f is the *relative nozzle area*, given by the ratio of the nozzle exit cross section to the area of the hexagon ($A_{hexagon}$) attached to it, as in figure 2.44.

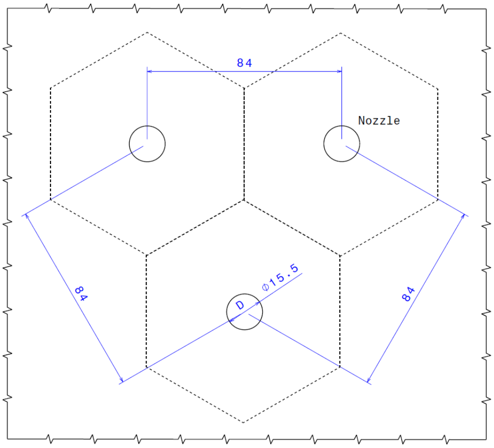

Figure 2.44: Hexagonal areas considered in the present work to use the Martin's correlation (dimensions in mm).

$$f = \frac{\pi/4D^2}{A_{hexagon}}$$

Martin indicates that, for sharp-edged nozzles, the set of equations (2.14) can be used if the contracted cross-sectional area is used instead of the geometric one. Consequently, the exit velocity, the nozzle diameter and the relative nozzle area must be replaced using the formula below. Here ζ means the *contraction coefficient*, i.e., the ratio of the narrowest cross section of the jet to the geometric nozzle exit cross section. The narrowest cross section is calculated as the section where the axial velocity is maximum.

$$|\tilde{\mathbf{v}}| = |\mathbf{v}|/\zeta \qquad \tilde{D} = D\sqrt{\zeta} \qquad \tilde{f} = f\zeta$$

In the present work, three different convective boundary conditions are compared: the first is the detailed spatial distribution provided by the CFD model ($h(x,y)_{CFD}$), the second is the surface average value of the detailed CFD distribution ($\bar{h}_{CFD}$) and the third is the average convective coefficient obtained by the Martin's correlation ($\bar{h}_{Martin}$). The comparison is made for two representative locations (figures 2.45 and 2.46), respectively a stagnation zone (TC9) and an intermediate point between two stagnation zones (TC5), visible in 2.38.

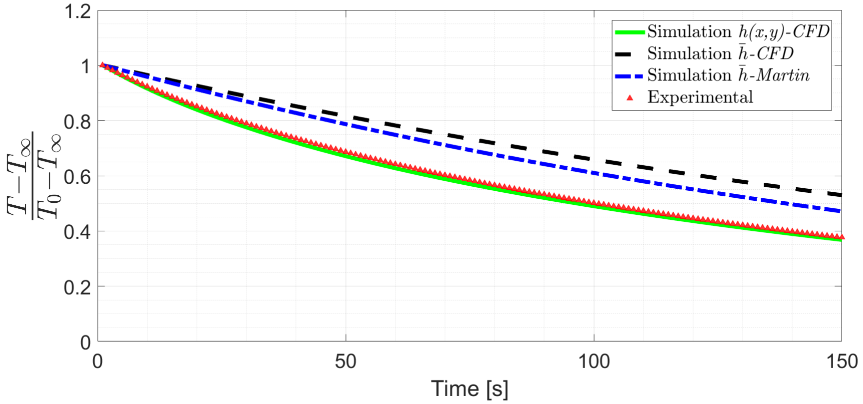

Figure 2.45: Effect of spatial variation of Nusselt number for Re=16000 at a stagnation zone (TC9)

It appears evident that both $\bar{h}_{CFD}$ and $\bar{h}_{Martin}$ slow down remarkably the cooling process, especially at the stagnation point, while the effect is substantially reduced in the intermediate zone. The difference between the results of the two average coefficients is due to the *border effects*: indeed the Martin's correlation considers an infinite array of jets, resulting in a higher heat transfer coefficient. In this particular case (cooling process) the higher value yields better accuracy than the $\bar{h}_{CFD}$. The reported sensitivity analysis confirms the importance of taking into account the spatial variation of the convective coefficient to obtain accurate results.

2.4.1.5 Tylose brick thermal field

In this section the thermal field within the Tylose brick is compared with the experimental data, obtained from the experimental tests described in §2.3.4. The third type boundary condition is imposed on the surfaces of the Tylose brick

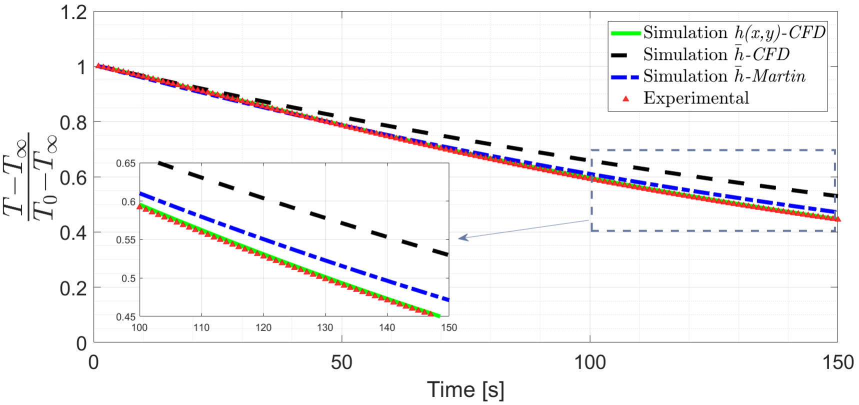

Figure 2.46: Effect of spatial variation of Nusselt number for Re=16000 at an intermediate zone (TC5)

exposed to the air flow and each convective heat transfer coefficient is calculated by CFD. In figures 2.47 and 2.48 the numerical and experimental temperature data are reported for the locations described in figure 2.18b. In Appendix 5 we report all the graphs referred to the nine configurations (combinations of three H/D and three Re). Three distinct thawing phases can be identified. During the first phase the temperature increases very fast, due to the high temperature difference between the item and the air, the low specific heat and the high thermal conductivity of the Tylose. This phase is followed by the *de-freezing* phase, characterized by high values of specific heat and low values of thermal conductivity (figure 2.17), moreover the temperature difference between the solid item and the air tends to decrease. This phase is typically the longest phase of a thawing process and the presence of this phase differentiates a thawing process from a tempering process (Y. Li et al. (2018)). The final phase is characterized again by a steep rise of the temperature due to the decrease of the specific heat. The temperature profiles, at the locations 6 and 7, are slightly different from the others, because the de-freezing phase is significantly more rapid. Indeed the two locations are closer to the upper surface of the Tylose brick, consequently they receive a higher heat flux. The importance of a spatial variation in the distribution of the Nusselt number has been shown previously for the metal slab. In this section we want to investigate further this aspect for a thicker material. In fact very thick, low conductivity materials have the characteristic to uniform spatially the heat flux along the thickness, loosing the information of the spatial variation from the surface to the interior. Considering the volume average value of the temperature in figure 2.48 it is evident that the use of the average value of the Nusselt distribution leads to the same profile than the detailed distribution. However if we look in detail at some regions we will discover that close to the surface, at 1 mm below the stagnation point, the temperature evolution is quite different using the two approaches (figure 2.51). While the time rate of change of the volume average temperature of the system is accurately reproduced by the simplified approach, consisting in using a uniform distribution of the Nusselt number on the surface of the body, a very detailed representation of the thermal field within the food item implies some knowledge about the spatial distribution of the heat transfer coefficient, especially if we aim to identify localized, overheated zones within the food. In figure 2.49 temperature contours are reported for the midsection x=0 (which correspond to the section A-A in figure 2.18b). The colors in the *color-bar* are: blue if the temperature is below 270 K, red if the temperature is above 273 K and yellow-green if the material is in the range 270-273 K (which correspond about to the phase change). The effect of the high Nusselt number at the stagnation zones is easily recognizable from the shape of the de-freezing front, as clear as the presence of the border effects which are always critical for the uniformity.

In figure 2.52 the comparison between the traditional air forced convection cabinet and the jet impingement technology is presented. The efficiency of the jet impingement permits to save almost the 50% of the process time in this specific condition. It is also clear that the use of the jet impingement technology introduces some complexities compared to a traditional thawing cabinet (Electrolux-Thawing (2014)), in terms of components, space and air pumping power. Consequently it is interesting to evaluate a trade-off in terms of thermofluid-dynamic efficiency, fan power and geometry complexity, in order to find the best setup. The present model represents a powerful tool to investigate different configurations in a computationally efficient way.

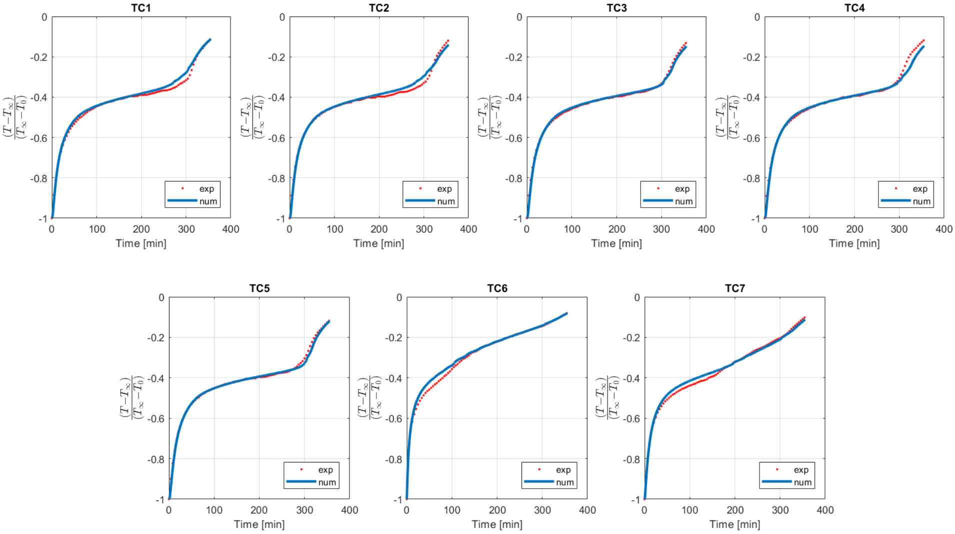

Figure 2.47: Comparison of the numerical and experimental dimensionless temperature histories for Re=34000 and H/D=2

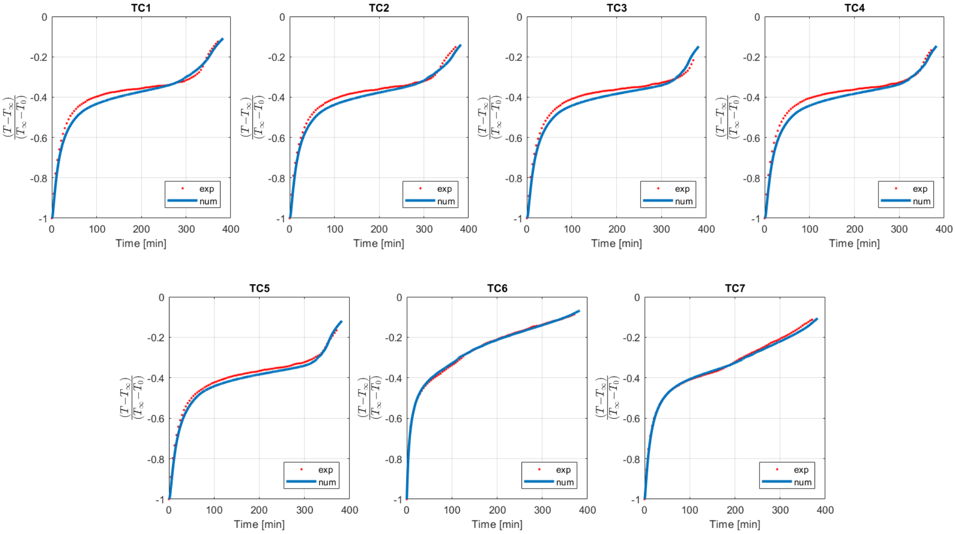

Figure 2.48: Comparison of the numerical and experimental dimensionless temperature histories for Re=17000 and H/D=5

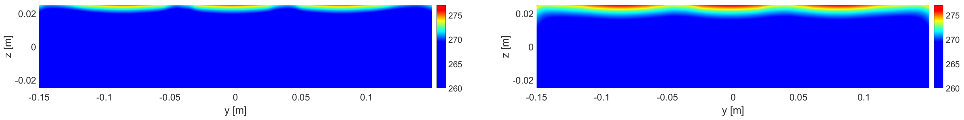

(a) t=1000 s

(b) t=2000 s

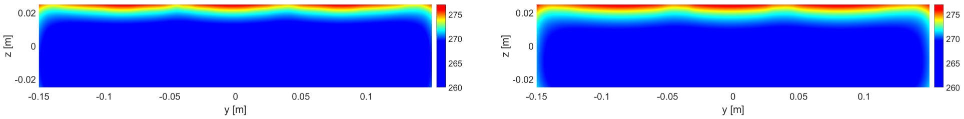

(c) t=3000 s

(d) t=4000 s

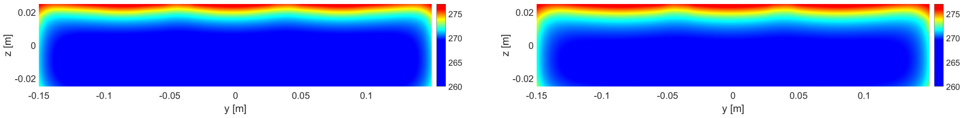

(e) t=5000 s

(f) t=6000 s

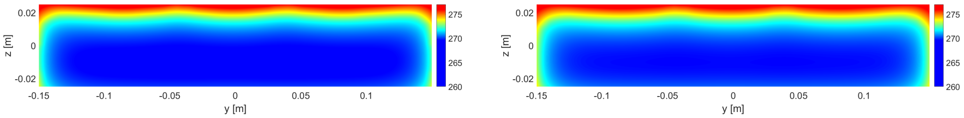

(g) t=7000 s

(h) t=8000 s

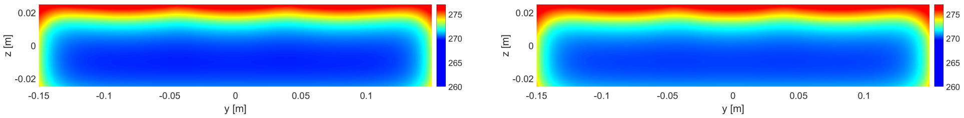

(i) t=9000 s

(j) t=10000 s

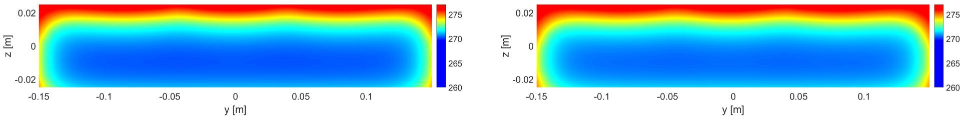

(k) t=11000 s

(l) t=12000 s

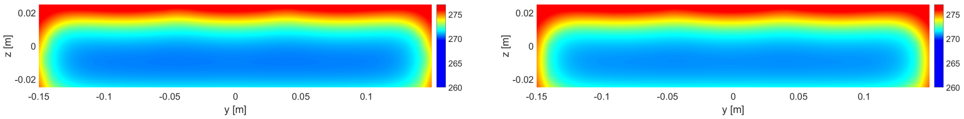

(m) t=13000 s

(n) t=14000 s

Figure 2.49: Temperature contours for x=0 midplane at different times, for H/D=5 and Re=23000.

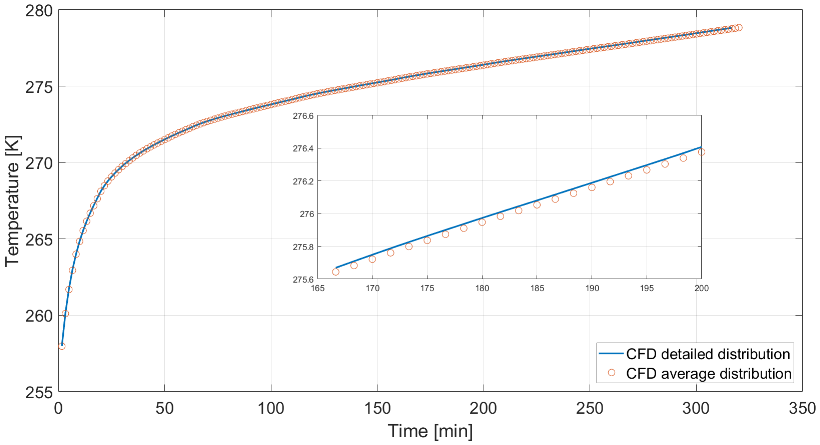

Figure 2.50: Comparison between the detailed Nusselt distribution and average Nusselt value in terms of volume average temperature of the Tylose brick.

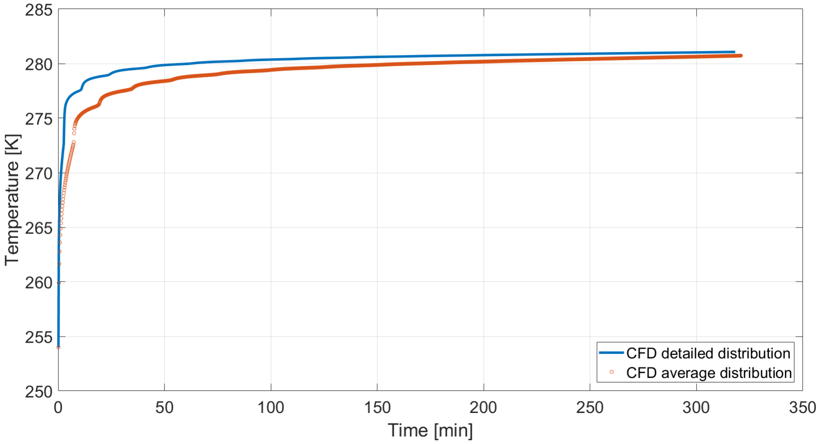

Figure 2.51: Comparison between the detailed Nusselt distribution and average Nusselt value in terms of local temperature of the Tylose brick near the stagnation zone.

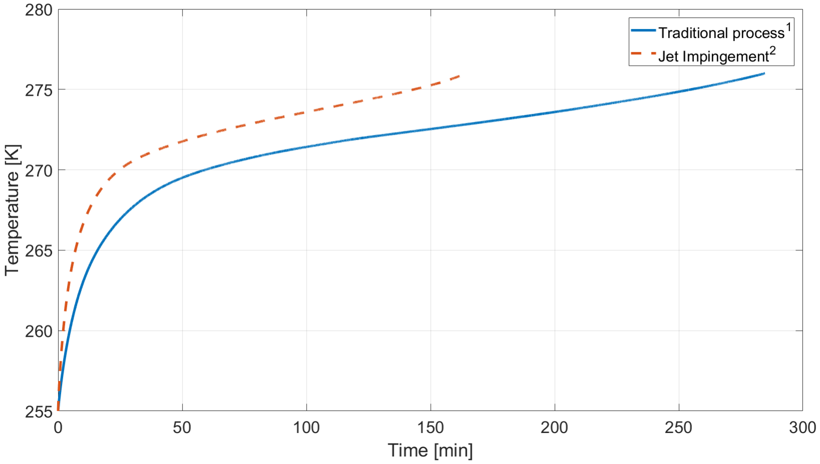

Figure 2.52: Comparison between the traditional thawing process and the jet impingement thawing process. [1] A uniform convective heat transfer coefficient, equal to 30 W/m^2K is used as boundary condition on the whole surface of the 20 mm height brick. [2] The convective heat transfer distribution is referred to Re=17000 and H/D=5. For both the simulation the air temperature is kept at 5°C.

2.4.2 Performance analysis of thawing professional appliances

2.4.2.1 Thawing indicators

The performance indicators for the considered thawing process are calculated for different operating conditions. In particular the numerical models (CFD+FDHCM) are used to describe the thawing process of a Tylose brick of 25 mm in height. The aim is to find some correlations of these indicators with some parameters linked to the jet impingement technology, as nozzle-to-plate distance (H/D), Reynolds number and the temperature of the jets, in order to understand which of the aforementioned parameters are more influent on the thawing performance. The results show a moderate effect of the Reynolds number on the performance (figure 2.53); this could be explained considering that the increase in the convective coefficient is no more efficient if the conductive resistance of the brick becomes the bottleneck of the thermal process. This is particularly true for the TrUI and VI indicators, while for the SRI the effect is more relevant. On the contrary, the effects of the temperature of the jets are clearly more evident on the indicators; the higher temperature difference between the air and the food item tends to accelerate the process on one side, but it has also a direct impact on the value of SRI, because the regions close to the surface remain at high temperature for a longer period of time. SRI is not monotonic, revealing two competing effects:

increasing the temperature of the jets speeds up the thawing process, while concurrently increasing the temperature gap between the surface of the target and its interior. This phenomenological picture is sustained by the trends of the TrUI and VI indicators (see figure 2.54). Consequently the curve presents a maximum at the dimensionless temperature of about 1.3. As for the TrUI, the increase in the temperature of the jets implies a higher heat flux, consequently higher temperature gradients within the food due to the low value of the thermal conductivity.

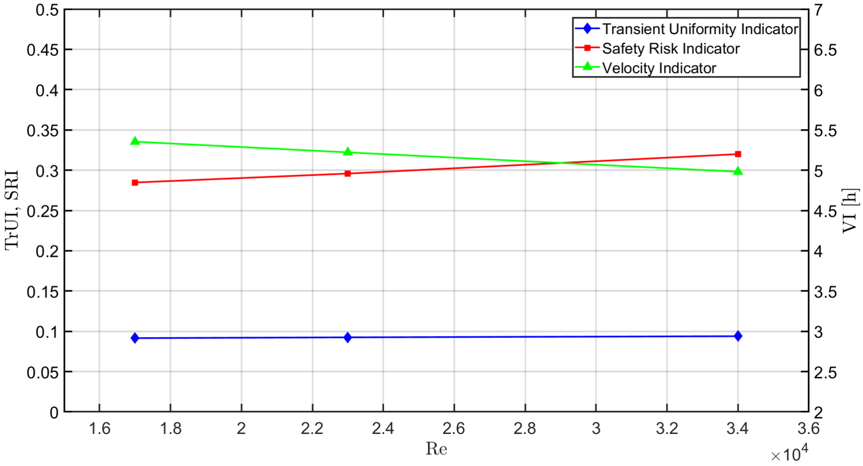

Figure 2.53: Performance indicators vs Reynolds, for $T_\infty = 9$ °C and H/D=5.

Finally, we have not found a clear dependence of the thawing parameters on the nozzle-to-plate distance. This result can be explained considering firstly that the H/D number has usually a more moderate effect than the Re number on the Nu distribution (Martin (1977),Zuckerman and Lior (2006)). Moreover the Tylose brick has a low thermal conductivity, which can become the dominant thermal resistance and can govern the thermal process (Mascheroni (2012)), mitigating the small differences in the heat transfer coefficient distribution on the surface, especially for the temperature histories related to the core of the brick.

This circumstance can be quantified and confirmed by calculating the Biot number (equation (2.15)): the value of the Biot number varies in time, since the thermal conductivity is dependent on the temperature. In figure 2.55 the Biot number is shown for two test cases, T_∞ equals to 10 °C and 15°C respectively: the Biot number presents an increasing trend at the beginning, when the value of the thermal conductivity has a sharp decrease due to the melting of the frozen water and then the Biot settles on the value of 6 because the thermal conductivity

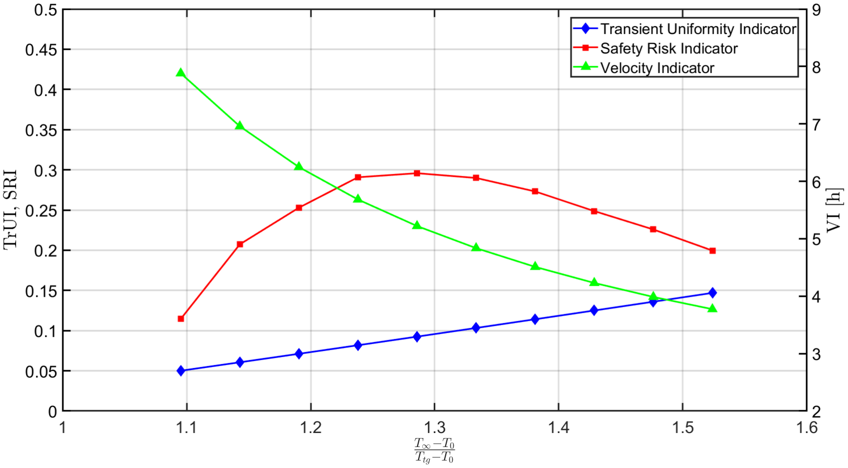

Figure 2.54: Performance indicators vs dimensionless temperature, with T_∞ from 5 °C to 14°C, $T_0 = -18$ °C and $T_{tg} = 3$ °C), for Reynolds 23000 and H/D=5.

of the liquid phase is rather independent of temperature (figure 2.17).

$$Bi(t) = \frac{V \int_A h(x,y)dA \cdot L/2}{A \int_V \lambda(x,y,z,t)dV} \tag{2.15}$$

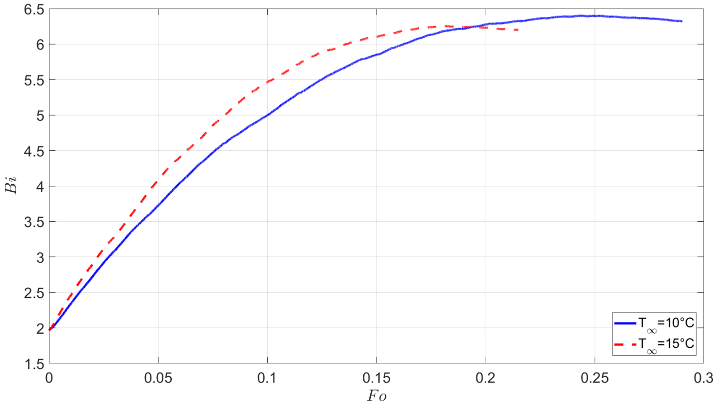

Figure 2.55: Biot number for two test conditions: T_∞ equals to 10 °C and 15°C, both with Reynolds 23000 and H/D=5.

An interesting comparison is between the use of the detailed Nusselt number distribution and the semi-empirical correlations provided by Martin (Martin (1977)), and previously used. The main concern is due to the implementation of the correlations in the case of a 3D shaped object, because actually these correlations are valid for flat surfaces. Consequently we decided to apply the correlations on the horizontal surface of the Tylose brick and on the lateral, vertical surfaces a series of different boundary conditions are applied.

	Detailed Nu distribution	Martin[1]	Martin[2]	Martin[3]
TrUI	0.049	0.021	0.052	0.053
SRI	0	0	0	0
endtime [h]	2.74	3.39	2.96	2.94

Table 2.2: Comparison between the use of the detailed Nusselt number distribution and the use of the Martin's correlation for a brick with dimensions (300 mm x 100 mm x 20 mm), for Re=17000, H/D=5, T_∞=5°C. Boundary condition on the vertical surfaces of the brick: [1] adiabatic; [2] average value of the CFD detailed distributions; [3] the Martin's correlation is applied everywhere.

As previously seen, the use of an average coefficient on the surface of the Tylose brick gives acceptable results in terms of global parameters (as the thawing indicators). However if we look at the local temperature evolution, we will find that in the stagnation regions the thawing rate is much lower using averaged coefficient. This lead to an underestimation of the localized overheated zones, as shown in figure 2.56).

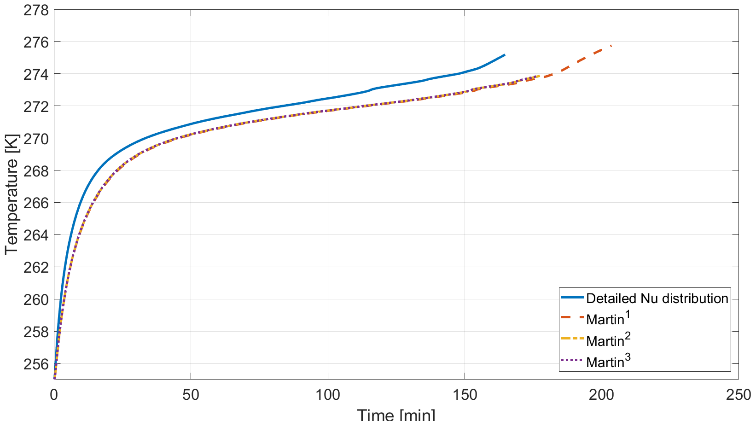

Figure 2.56: Comparison of the temperature history at a stagnation point between the use of the detailed Nusselt number distribution and the use of the Martin's correlation for a brick with dimensions (300 mm x 100 mm x 20 mm), for Re=17000, H/D=5, T_∞=5°C.

2.4.2.2 Comparison of one- and two-side impingement for thawing operations

The jet impingement is a technology that relies on the high heat transfer rates on the surface below the array of jets. Differently from the volumetric heat generation technologies (e.g. microwave or radio-frequency), the heat is conveyed from the surface to the interior of the item. Consequently the uniformity of the heating process within the food item is dependent on the amount of surface in contact with the jet airflow.

The jet impingement technology can be further improved by placing a second array of jets below the food item, creating a *two-side* configuration (figure 2.57). In the proposed example, a second array (completely identical to the first) is placed below the food item. Two mass-flow inlet conditions are assigned on two symmetric sections placed within two symmetric plenum regions. The airflow leaves the domain through lateral openings. The food item is placed on a tray, made of stainless steel (AISI 304, $\lambda = 17\,W/mK$ and 1 mm of thickness), which induces an additional thermal resistance to the heat transfer at the lower surface.

The first analysis is referred to the evaluation of the analogies between the two distributions of the Nusselt number on the top and bottom surfaces. Consequently a CFD simulation has been carried out considering the tray and the food item placed between the two arrays of jets and the Nusselt number distribution is calculated on the top and bottom surfaces. Therefore, we have compared the two distributions of the convective coefficient on the two surfaces and, at the same time, the distribution referred to the CFD simulation with the *one-side* configura-

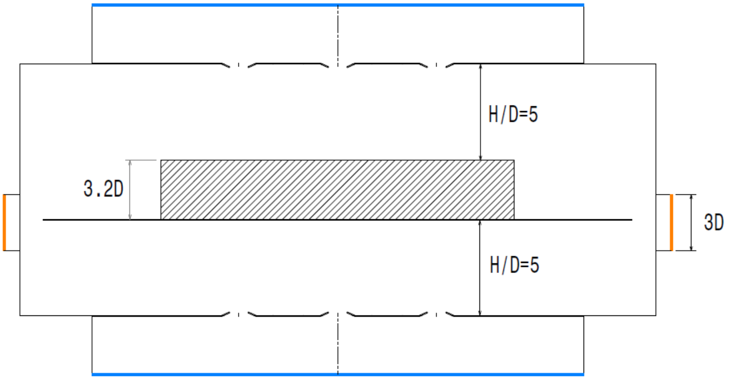

Figure 2.57: A view of the two-side configuration: the two inlet sections are marked in blue, the outlet sections are marked in orange.

tion. Figure 2.58 shows a negligible difference between the three distributions, suggesting the possibility to use the one-side CFD model to study the two-side configurations, with a considerable saving of computational effort.

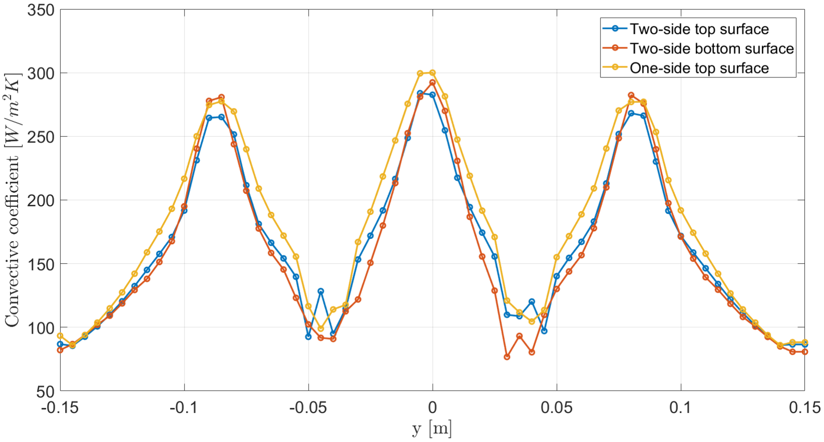

Figure 2.58: Comparison between the distributions of the convective heat transfer coefficient for the one-side and two-side configurations

The use of a two-side impingement is evaluated comparing its results with the ones referred to the one-side impingement, in terms of thermal-field and thawing indicators. In figure 2.59 the profile of the volume average temperature are plotted against time for the two configurations: the two-side impingement leads to a remarkable time saving.

Figure 2.60 reports the dependence of the thawing indexes on the dimension-

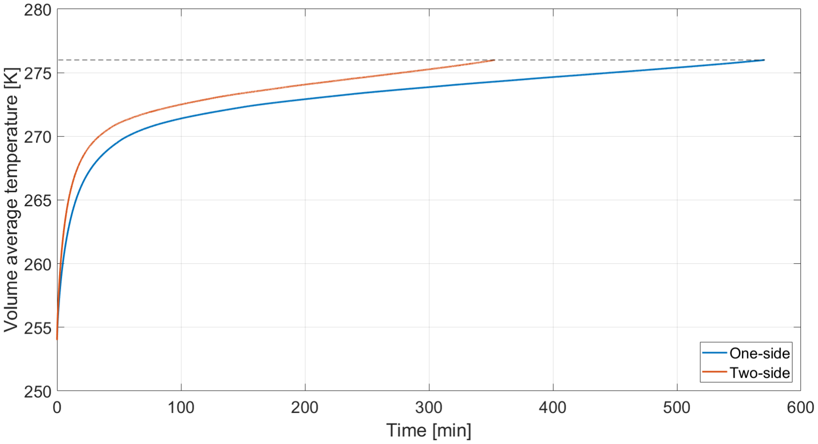

Figure 2.59: Volume average temperature comparison between one-side and two-side impingement

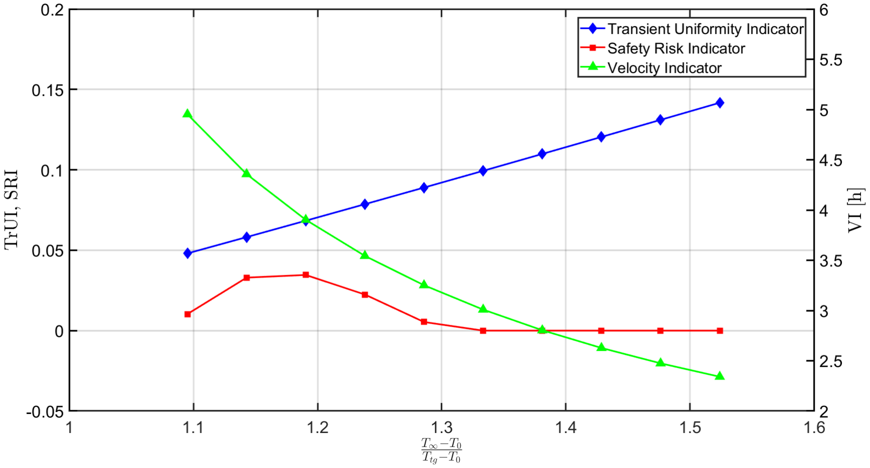

Figure 2.60: Performance indicators vs dimensionless temperature, with T_∞ from 5 °C to 14°C, $T_0 = -18$ °C and $T_{tg} = 3$ °C), for Reynolds 23000 and H/D=5 and two-side impingement configuration.

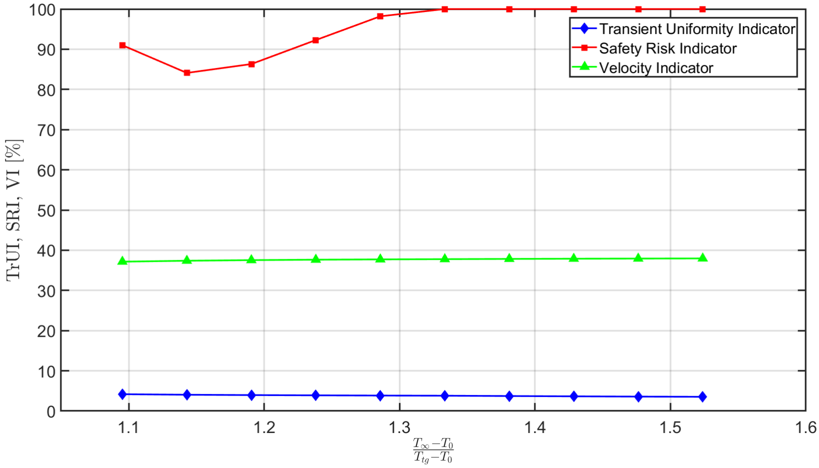

Figure 2.61: Relative difference between two- and one-side configurations in terms of thawing performance indicators varying the dimensionless temperature, with T_∞ from 5 °C to 14°C, $T_0 = -18$ °C and $T_{tg} = 3$ °C), for Reynolds 23000 and H/D=5.

less temperature of the jets. This graph can be compared with the corresponding results for the one-side configuration (figure 2.54). The SRI function is not monotonic as for the one-side, but the higher thawing rate ensures a completely safe process for dimensionless temperatures larger than about 1.35, because the entire process time is within the dangerous zone time limit (e.g. in this case we used 3h). The performance indicators for the one- and two-side configuration are compared first in figure 2.61 and then in table 2.3. The indicators are calculated at the end of the thawing process. The two-side configuration bears some advantages both in terms of reduced thawing time and safety. In particular, since the TrUI index doesn't change remarkably, the lower SRI is essentially due to the reduction of the time in which some zones within the brick remain at *dangerous* values of temperature. The two-side ensures a significant (38%) reduction of thawing time.

When it comes to thawing indicators, as shown in table 2.3 the two-side configuration bears some advantages both in terms of productivity and safety. The TrUI index doesn't change remarkably, thus the lower SRI is essentially due to the reduction of the time in which some zones within the brick remain at *dangerous* values of temperature.

	Thawing time [h]	Safety Risk Index	Transient Uniformity Index
One-side	6.25	0.25	0.071
Two-side	3.9	0.035	0.068
Relative difference	-38%	-86%	-4.2%

Table 2.3: Comparison between one and two-side impingement at air temperature of 7°C, τ_{max}=3h, H/D=5 and Reynolds 23000

2.5 Concluding remarks

In the present chapter we have proposed and validated experimentally a design tool for jet impingement thawing appliances. The method combines reliability and low execution time and consists in the combination in cascade of two numerical models, a CFD model and a FDHCM respectively. During the development of the models an extensive experimental campaign has been performed to provide data for the validation process. Firstly, the airflow velocity field has been measured by the use of a hot wire anemometer, which has been calibrated and then used to study the velocity profile along the jet axis for three representative jets. The experimental velocity profiles are in good agreement with the CFD simulations for all the three jets. Consequently, the CFD model has been used to investigate the thermofluid-dynamic behaviour of the jet impingement technology and to calculate the effects of the jets on the surface in terms of heat transfer coefficients. In particular, the micro-calorimeters technique has been implemented experimentally: it consists of the use of small lumped-capacitance elements, which are used as calorimeters to retrieve the local convective heat transfer coefficient from the temperature profile during a cooling or heating process. The matrix of micro-calorimeters has been assembled in-house, using small copper disks welded with high resolution thermocouples. The experimental maps of the Nusselt coefficient are compared with the respective CFD model and an excellent agreement has been found. The next step has been the study of the thermal field within the solid objects placed in the jet chamber. For this purpose the FDHCM model has been developed: in particular the distribution of the Nusselt number, retrieved by the CFD model, is used as boundary condition for a computationally-efficient model (FDHCM), which is used to evaluate the thermal field within the solid objects. The use of such model permits to have great savings in terms of time if it is compared to the use of a CFD model for the entire thermal process. The FDHCM has been validated for two test cases: a thin metal slab and a Tylose brick. In the first case a 5 mm in height metal slab is placed in the test chamber, heated by an external source and cooled then by the airflow from the jets. The agreement between experimental and numerical data is very good, moreover the importance of a spatial distribution for the Nusselt number has been remarked comparing it with a constant distribution found in literature. For the second test case the thawing process of a Tylose brick has been studied. The Tylose is a meat analog material, commonly used in food processing investigations. The thermal field within the brick has been investigated at seven locations and the experimental temperature data are compared with the numerical ones, finding an excellent agreement. Therefore the use of jet impingement for thawing processes has been investigated more deeply by the use of thawing indicators, in particular to evaluate the effects of some parameters (H/D, temperature of the air and Reynolds) in terms of productivity and quality of the thermal process. It has been concluded that the Reynolds has a moderate effect, while the temperature of the air has a big effect on the quality of the process, in particular an excessive increase of the temperature leads to a bad quality of the thawing process. Finally, we have studied the effects of a two-side impingement, that is the use of a double array of jets in order to exchange heat also from the lower surface of the food. The use of a two-side configuration leads to a higher productivity and at the same time to a safer thawing process.

We can conclude that the validated numerical method represents a valid tool to analyse the jet impingement technology for food processing professional appliances. In particular it is very useful during the design process, thanks to its efficiency in terms of computational time and reliability.

Chapter 3

Robust industrial-design tool for gas boilers for professional combi-ovens

3.1 Introduction and state of the art

Professional ovens are among the most widely used appliances in the food-service field. Innovative design tools are considered strategic during the development of such machines, especially if the methods are reliable and computationally-efficient at the same time. In the present work we present a design tool to describe the thermal behaviour of a gas-fired steam generator, or gas boiler, which is used for the production of steam during cooking operations.

Gas boilers can be integrated into professional ovens for the *instantaneous* production of saturated water vapor, thus providing *combined* cooking modes with different concentrations of water vapor (Electrolux-Oven (2017)). In most of these appliances the vapor is produced at slightly above-atmospheric pressure and thereby is driven into the cavity of the oven. Restaurants are extremely energy intensive, using about 5 to 7 times more energy per square foot than other commercial buildings, such as office buildings and retail stores (ENERGYSTAR (2015)). Mudie et al. (2016) state that combi-ovens are responsible for 12% of the energy consumption in commercial kitchens: thus, the need for advanced, reliable and time-efficient design and optimization strategies for professional ovens is self-evident (Yadav et al. (2014), Yang et al. (2015), Mohanty et al. (2016)).

Several numerical models of water boilers have been proposed so far. Collazo et al. (2012) set forth a simplified model for solid-fuel combustion and apply it to the numerical simulation of a small-scale boiler. The biomass combustion is explicitly simulated within the packed bed, considered as a porous medium. The bed is represented by an aggregate of particles in different stages of combustion: drying, pyrolysis and char combustion. The radiation heat transfer cannot be neglected in solid-fuel combustion due to the presence of soot and is modelled by the Discrete Ordinates (DO) approach (Yin et al.; Howell et al. (2017; 2016)).Gómez et al. (2017) simulate the combustion within a biomass domestic boiler, with rated power of 27 kW. The packed bed is represented by a porous zone, modelled by the Volume-Averaging approach (Gray et al.; Whitaker (1993; 1999)). The calculated heat transfer rate, flue gas temperature and CO_2 emissions are in good agreement with the reported experimental measurements. Drosatos et al. (2017) simulate the combustion and heat transfer process taking place in a wood gasification household boiler, with nominal power of approximately 50 kW. An ad-hoc thermodynamic model yields the characteristics of the syngas, produced under steady-state conditions. The heat is exchanged with a volume of boiling water; the presence of the water is recovered by assigning a constant temperature boundary condition.

Athanasios et al. (2015) use the steady state model of a wood-log fired boiler to optimize the placement of a deflector, with the aim of increasing the gas residence time into the combustion chamber. Buczyński et al. (2015) propose a CFD model of a domestic central heating boiler fired with solid fuel. The burner shape is modified to increase the swirl component of the burning gases, thereof increasing the residence time in the radiant section of the combustion chamber and achieving a more uniform temperature distribution inside the boiler. Zhang et al. (2017) propose a numerical model of a hot water boiler and validate it by comparison with experimental measurements. Inorganic heat pipes are used as heat exchangers between the hot gas and the water due to their high efficiency: the lower part of the heat pipe is heated by convection and radiation from the combustion chamber and the upper part of the heat pipe is in contact with water. The combustion process is not explicitly modelled: the inlet temperature of the combustion products derives from experimental data. The DO radiation model is used to compute the radiative heat transfer within the combustion chamber. The relative error between numerical and experimental results is 10% for the heat load and 2.2% for the temperature of the flue gas at the outlet of ring-shaped flue area. We propose a simple, reliable and computationally-efficient CFD model for gas boilers. Its outcomes are in excellent agreement with experimental measurements for different operating conditions. The innovative characteristic of the proposed method is the simplification of complex phenomena, which would require a high computational effort. Indeed the combustion kinetics is not explicitly modelled: instead, the composition and thermodynamic properties of the gas mixture released from the burner is set according to the energy balance for an ideal combustion. The diffusion, convection and turbulent dispersion of the different gas species are neglected, hence the composition of the exhaust gas is constant and uniform. On the water side, the boiling process and the consequent phase change are not explicitly considered and a uniform temperature, corresponding to water saturation at ambient pressure, is assumed on the water side of the heat exchange surface. The proposed model allows to study hundreds of boiler configurations with low computational effort and with a low number of tuning parameters.

3.2 Materials and methods

3.2.1 Test rig

An experimental facility has been designed to obtain data for the validation of the numerical model. The apparatus, shown in figure 3.1, is a open-loop circuit: air is taken from the environment and mixed suddenly with the methane at the blower inlet. The flow through the impeller ensures a high degree of uniformity of the mixture. The blower (ebm-papst RG128/1300-3612) is a centrifugal fan, controlled by the PWM technique (Peddapelli (2017)) according to the power requested from the oven and it is also responsible of the switch-off of the machine in dangerous conditions (several sensor are placed in the experimental setup to ensure safety conditions). The mixture is conveyed at the combustion chamber where the premixed combustion occurs. The gas valve (848 SIGMA air/gas modulating valve) modulates the gas flow according to the under-pressure measured at the blower inlet, in order to ensure a constant value of the *air-fuel equivalence ratio*, with a value of 1.15-1.17 (lean combustion) to have a low formation of CO and NO_x. [1]. A water level sensor is responsible of the refill of the water by the activation of an electro-valve and a second water sensor is used to check if the water level decreases under the safety threshold. A data acquisition station is used to monitor the experimental tests: a digital multi-meter AGILENT 34972A is used to monitor the temperatures and a gas analyzer Testo340 [2] is used to verify the gas composition at the exhaust exit pipe. The dry gas meter Elster G4-10, which operates in the range $[40\,dm^3/h \div 10\,m^3/h]$ with maximum operative pressure of 0.5 bar, is used to monitor the gas flow rate. All the sensors are acquired by the software LabVIEW 2016 (© National Instruments). The ambient temperature is maintained between $15°C$ and $20°C$.

---

[1] The air-fuel equivalence ratio is defined as the ratio of the mass of air used in the combustion and the stoichiometric mass of air

[2] The concentrations are measured by a Testo 340 industrial flue analyzer (LTD ()), with accuracy for individual gas species of: ± 2 ppm in the range $0 \div 39.9$ ppm for CO; $\pm 0.2\%$ Vol for O_2; ± 10 ppm in the range $0 \div 199$ ppm for NO_2; ± 5 ppm in the range $0 \div 99$ ppm for NO.

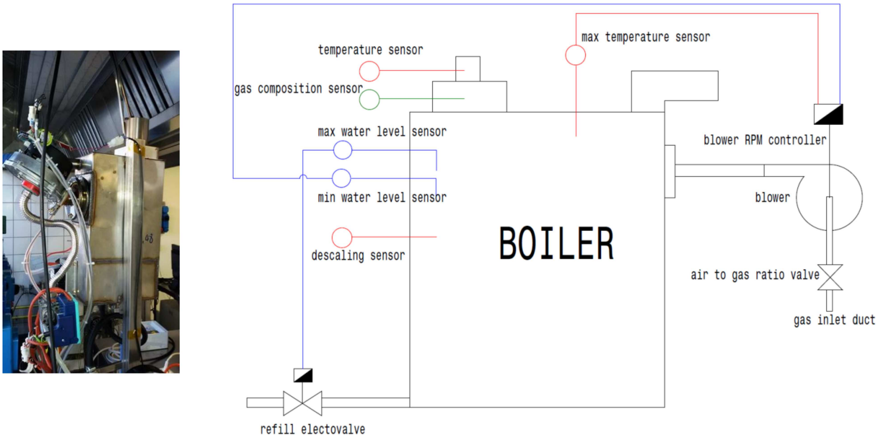

Figure 3.1: Experimental setup.

3.2.2 The proposed design tool

3.2.2.1 Physical model

The proposed design tool consists of a computationally-efficient finite-volume CFD model for the flow and heat transfer within the combustion region of the boiler. The computational domain comprises the combustion chamber, where a premixed combustion of methane and air takes place, and a corrugated tube, named *fire tube*, where heat is transferred by convection from the hot combustion products to the surrounding, boiling water. The corrugated profile ensures a higher exchanging surface and increases the turbulence. The gas region is enclosed in a stailness steel (AISI 304) case 1.5 mm thick, surrounded by water. The boiling process occurs at nearly atmospheric pressure and the vapour produced exits the boiler from an opening on the top of the device. The nominal power of the considered boiler is about 10 kW.

In figure 3.3 a schematic representation of the boiler and of the considered domain is shown: the water region is not explicitly modelled.

3.2.2.1.1 The combustion process

A premixed combustion of methane takes place within the considered boiler, with air-fuel equivalence ratio $e \approx 1.15$. This type of combustion is characterized by low values of toxic exhaust gases. In table 3.1 the concentrations of O_2, CO, CO_2, NO and NO_2 are reported, for operating conditions corresponding to 68%, 90% and 100% of the rated power. Due to the remarkably low concentrations of

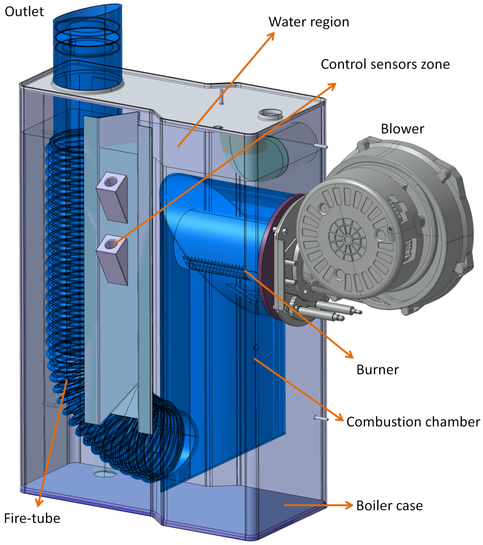

Figure 3.2: Scheme of the considered gas boiler. The exhaust gas zone is easily recognizable in blue.

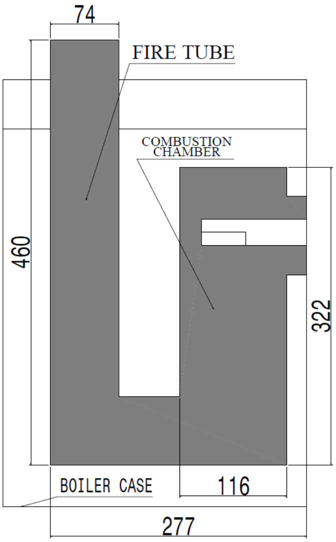

Figure 3.3: Computational domain, gas region (dimensions in mm).

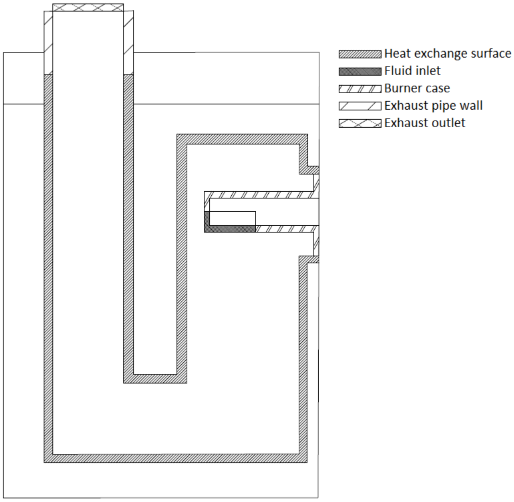

Figure 3.4: Computational domain, boundaries.

NO_x and CO measured in the exhausts, an ideal combustion is assumed:

$$CH_4 + 2\,e\,\left(O_2 + 3.76\,N_2\right) \longrightarrow 2\,H_2O + CO_2 + 7.52\,e\,N_2 + 2\,\left(e-1\right)\,O_2 \qquad (3.1)$$

The proposed model does not account directly for the combustion kinetics, as suggested by Zhang et al. (2017). The exhaust gas, modelled as a mixture of ideal gases with constant composition, enters the combustion chamber with a temperature calculated by an energy balance (as explained in §3.2.2.1.4). The thermophysical properties of the exhaust gas are calculated as mass-weighted average of the corresponding properties of the constituent species, in turn evaluated using well-established correlations, listed in table 3.2, and reported in graphical format in figure 3.5.

3.2.2.1.2 Radiation heat transfer

The combustion processes are commonly characterized by intense radiation heat transfer. This is particularly true when high temperature differences occur within the considered domain, as for boilers. The modelling of the radiation heat transfer may account for or disregard the interaction with the interposed fluid medium (i.e. considering only the radiation heat transfer between surfaces). Two

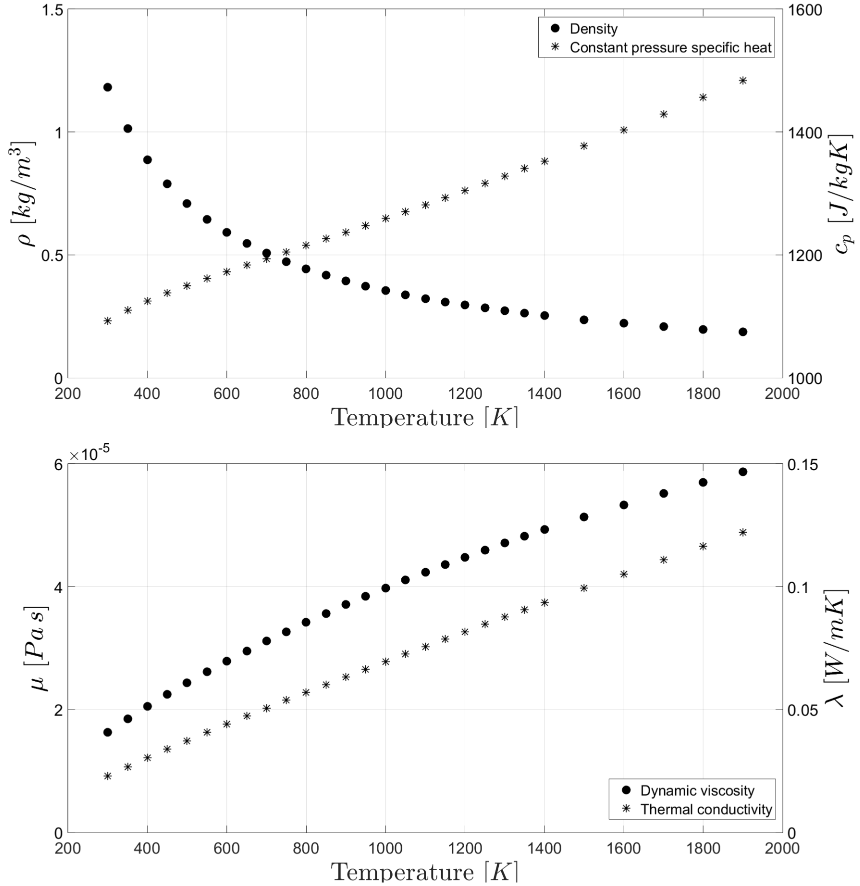

Figure 3.5: Thermophysical properties of the considered gas mixture at normal atmospheric pressure.

% rated power	O_2[%Vol] (ideal combustion)	CO[ppm] (dry)	CO_2[%Vol] (ideal combustion)	NO[ppm]	NO_2[ppm] (dry)	e
68	2.96 (2.5)	3 (3.49)	10.05 (8.4)	50.0	52.5 (61.12)	1.15
90	3.09 (2.5)	3 (3.52)	9.98 (8.4)	45.0	47.5 (55.70)	1.15
100	3.42 (2.8)	4 (4.78)	9.79 (8.2)	37.4	39.3 (46.97)	1.17

Table 3.1: Measured concentrations of different gas species in the flue gas at the exhaust outlet.

Thermodynamic property	Chemical species			
	Oxygen	Nitrogen	Water vapor	Carbon dioxide
Thermal conductivity	ST	ST	CLS	ST
Dynamic viscosity	SL	SL	SL	SL
Specific heat (constant pressure)	ED	ED	ED	ED
Density	IGL	IGL	IGL	IGL

Table 3.2: Models used for the calculation of thermophysical properties of gas species (see, e.g., Green and Perry; Pitzer (2008; 1955)). Models are identified as follows: ST – Stiel-Thodos Green and Perry (2008), CLS – Chung-Lee-Starling Green and Perry (2008), SL – Sutherland law Green and Perry (2008), ED – experimental data from literature Green and Perry (2008), IGL – ideal gas law.

physical models, representative of the two approaches, are briefly outlined in this section.

Participating Media

The first model, called *Participating Media* model (PM hereinafter), takes into account the interaction of the radiation with the medium that fills the space between the irradiating surfaces. During this interaction the medium absorbs, emits and scatters radiation; even if gaseous combustion products do not scatter radiation significantly, CO_2 and $H_2O(v)$ are strong selective emitters and absorbers of radiation (Siegel and Howell (1992)). The degree of absorption is described by the averaged absorption coefficient, which is calculated by the *Weighted Sum of Gray Gases* (WSGG) model and then it is used for the radiation intensity equation Yin et al. (2017). The WSGG method uses the Hottel charts (Siegel and Howell (1992)) and *sum-of-gray-gases* models for a mixture containing CO_2 and/or $H_2O(v)$ only. In particular, the definition of emissivity (ϵ) is used to find a weighted value of the absorption coefficient $\bar{a}$ of the mixture of exhaust gases, using the Bouguer-Lambert law and the concept of *Optical Path Length* S (Siegel and Howell (1992)). The equation (3.2) is used to calculate ϵ: the values of a_k are calculated with the Hottel charts, the *Optical Path Length* S is derived from equation (3.30) and b_k denotes the mass concentrations of the gaseous combustion products (N is the total number of combustion products).

$$\epsilon = \sum_{k}^{N} b_k (1 - e^{-a_k S_k}) \tag{3.2}$$

The value of ϵ is then used to calculate the weighted absorption coefficient $\bar{a}$ from the equation (3.3):

$$\epsilon = 1 - e^{-\bar{a}S} \tag{3.3}$$

The weighted absorption coefficient is used in the Radiative Transfer Equation (hereinafter RTE, here in its general formulation for an arbitrary wave-number ν):

$$\frac{dI_\nu}{ds} = -\beta_\nu I_\nu(s) + a_\nu I_{\nu b}(s) + \frac{\sigma_{\nu s}}{4\pi} \int_0^{4\pi} I_\nu(s, \omega_i) \Phi'(\nu, \omega, \omega_i) d\omega_i \tag{3.4}$$

where

$$I_{\nu b} = \frac{2C_1}{\nu^5 \left(e^{C_2/\nu T} - 1\right)} \tag{3.5}$$

with $C_1 = 0.595522 \cdot 10^{-16}\, Wm^2/s$ and $C_2 = 0.01439\, mK$. The equation 3.4 describes the *change in radiation intensity with s*: the first term is the loss by absorption and scattering ($\beta_\nu = a_\nu + \sigma_{\nu s}$), the second term is the gain by emission and the the third term is the gain by scattering into s direction (Φ' is the *Phase Function*, ω is the solid angle and ν is the wavelength, Siegel and Howell (1992)). In the present model the scattering is neglected and consequently $\beta_\nu = a_\nu = \bar{a}$. The equation is solved numerically with the *Discrete Ordinates Method* Siegel and Howell (1992). The resulting radiation intensity field (for gray gases) is then used to compute the radiation heat flux that crosses a generic surface with normal $\hat{\mathbf{s}}$

$$\mathbf{q''_R} = \int_{4\pi} I(\hat{\mathbf{s}}_\mathbf{i})(\hat{\mathbf{s}}_\mathbf{i} \cdot \hat{\mathbf{s}})\hat{\mathbf{s}}\, d\omega \tag{3.6}$$

The radiative flux $\mathbf{q''_R}$ contributes to the energy equation:

$$\rho c_v \frac{DT}{Dt} = \nabla \cdot (\lambda \nabla T) - p\nabla \cdot \mathbf{u} + \Phi - \nabla \cdot \mathbf{q''_R} \tag{3.7}$$

where Φ is the *Dissipation Function* Versteeg and Malalasekra (2007).

Surface to Surface

In the second approach only the solid walls contribute to the radiation heat transfer mechanism, and this approach is consequently called *Surface to Surface* (S2S hereinafter). For each surface the radiant fluxes are obtained by enforcing radiation equilibrium on the entire closed set of surfaces for each radiation spectrum independently. For each patch, the net rate (q_i) at which radiation leaves the surface i, is equal to the difference between the surface radiosity (J) and irradiation (G) (Bergman et al. (2011)).

$$q_i = (J_i - G_i) \tag{3.8}$$

The radiosity is calculated as:

$$J_i = E_i - \rho_i G_i \tag{3.9}$$

where E is the surface emissivity power.

For an opaque ($\rho_i = 1 - \epsilon_i$), diffuse (the emissivity is independent of the direction), gray surface (the emissivity can be considered a fraction of the black body emissivity and it is independent of the wavelength), the radiosity may be expressed as:

$$J_i = \epsilon_i E_{bi} + (1 - \epsilon_i) G_i \tag{3.10}$$

where E_{bi} is the black body surface emissivity power.

The irradiation of the surface i can be expressed from the radiosities of all the surrounding surfaces j

$$A_i G_i = \sum_j A_j F_{ji} J_j = \sum_j A_i F_{ij} J_j \tag{3.11}$$

After some calculation for each surface i is valid the following equation:

$$J_i = \epsilon_i E_{bi} + (1 - \epsilon_i) \sum_j F_{ij} J_j \tag{3.12}$$

The corresponding set of equations is solved and the net radiating flux is calculated for each surface. The total heat flux at each wall is calculated as sum of radiation and convection heat flux. Despite the PM model, we need to solve only a set of equations for the surface nodes and this simplification allows to significantly reduce the computational effort. The flame near the burner is assumed to provide the most significant contribution to the radiation field inside the boiler, therefore the idea is to give to the inlet surface specific radiative conditions in order to reproduce the effects of the flame. The thermodynamic conditions imposed in this surface are discussed in detail in the paragraph §3.2.2.1.4.

3.2.2.1.3 Governing equations

The heat transfer process is calculated solving the mass, momentum and energy balance equations: for the S2S model the radiation fluxes are obtained by enforcing radiation equilibrium on the entire closed set of surfaces (STAR-CCM+ (2017)), on the contrary for the PM model the radiation is considered with the RTE, as described in §3.2.2.1.2. The RANS *Realizable* $k-\varepsilon$ model (Versteeg and Malalasekra (2007)) is used for turbulence modelling. The *realizability* conditions for turbulent stresses require the positivity of normal stresses:

$$\overline{u_i' \, u_i'} \geq 0 \tag{3.13a}$$

and that the shear stresses satisfy the following Cauchy-Schwarz inequality Pope (2000):

$$-1 \leq \frac{\overline{u_i' \, u_j'}}{\sqrt{\overline{(u_i')^2} \, \overline{(u_j')^2}}} \leq 1 \tag{3.13b}$$

It is well-known that the *Standard* $k-\varepsilon$ turbulence model may locally violate the realizability conditions in regions of intense shear: indeed, this circumstance occurs with the considered flow configuration.

In figure 3.6 it is evident that the realizability condition (3.13a) is violated by the *Standard* $k-\varepsilon$ model for the *y* velocity component in the connecting region between the combustion chamber and the fire-tube, where the streamlines bend sharply. Due to the aforementioned inconsistencies, the *Realizable* $k-\varepsilon$ turbulence model is used for the reported simulations, as it inherently satisfies the conditions (3.13a) and (3.13b).

3.2.2.1.4 Boundary conditions

The boundary of the computational domain is subdivided into five distinct surfaces, denoted by *Fluid inlet*, *Burner case*, *Heat exchange surface*, *Exhaust pipe wall* and *Exhaust outlet*.

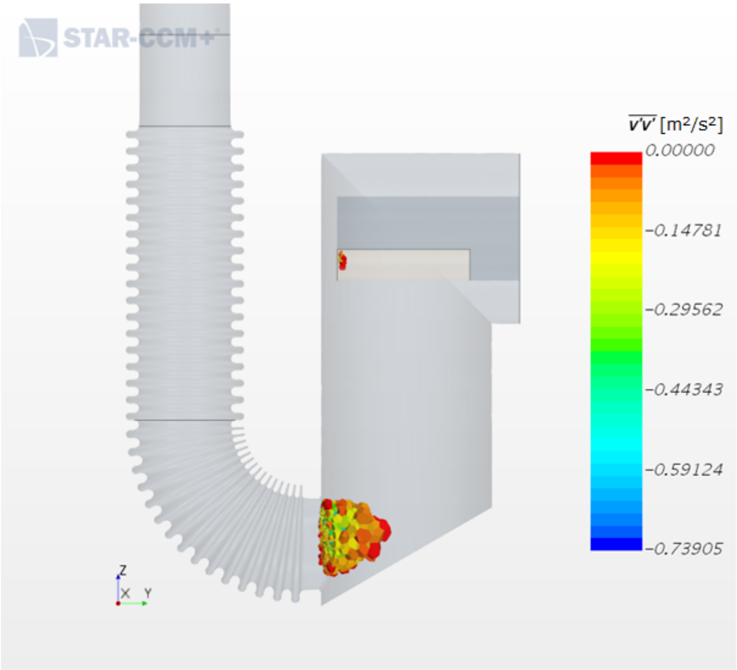

Figure 3.6: Cells where the realizability condition is violated.

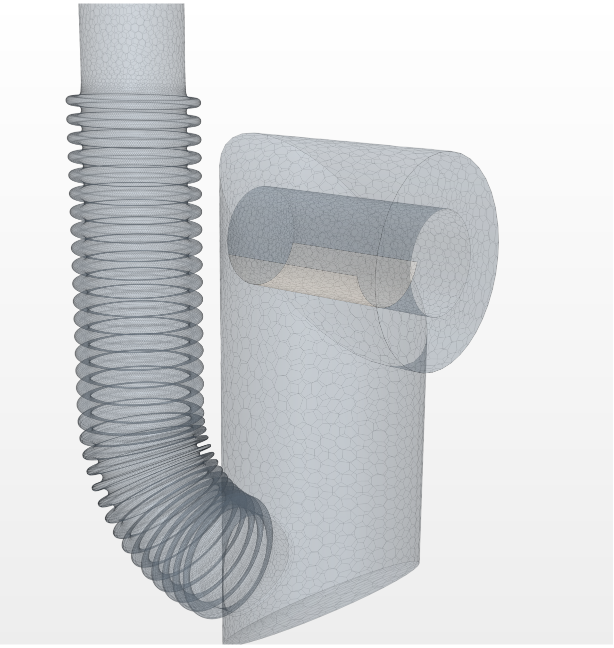

Figure 3.7: Geometry and surface mesh used in the simulation.

Fluid inlet

This boundary covers part of the lateral, cylindrical mantle of the burner (figures 3.3, 3.4, 3.7) and admits the exhaust gas into the combustion chamber, with uniform mass flux and at uniform temperature T_{in}.

Let Q (< 0) denote the heat transfer rate transferred from the exhaust gas towards the boiling water and Q_D (< 0) the heat transfer rate released to the surroundings through the case of the boiler. The steady-state energy balance for the boiler yields (Cavallini and Mattarolo (1990)):

$$\begin{aligned} |Q| + |Q_D| &= \dot{m}_c \ \mathrm{LHV}^0 + \dot{m}_c \ (i - i_c^0) + \dot{m}_a \ (i_a - i_a^0) \\ &- \dot{m}_f \ (i_f - i_f^0) - \dot{m}_v \ (i_v - i_v^0) \end{aligned} \tag{3.14}$$

where the subscripts f and v denote dry gases and water vapour respectively, while the superscript ^{0} denotes the reference conditions. The combustion products enter the computational domain at specified inlet conditions. The energy balance for the boiler becomes:

$$|Q| + |Q_D| = Q_r + (\dot{m}_f + \dot{m}_v) i_f^{in} - (\dot{m}_f + \dot{m}_v) i_f^* \tag{3.15}$$

where i_f^* denotes the specific enthalpy of the exhaust gas leaving the boiler and Q_r denotes the radiative heat transfer:

$$\dot{m}_f^* i_f^* = (\dot{m}_f + \dot{m}_v) i_f^* = \dot{m}_f \; i_f + \dot{m}_v \; i_v \tag{3.16}$$

Comparing (3.14) with (3.15) yields

$$\begin{aligned} Q_r + \dot{m}_f^*(i_f^{in} - i_f^*) \quad &= \quad \dot{m}_c \; \mathrm{LHV}^0 + \dot{m}_c \; \left(i_c - i_c^0\right) + \dot{m}_a \; \left(i_a - i_a^0\right) \\ &- \quad \dot{m}_f \; \left(i_f - i_f^0\right) - \dot{m}_v \; \left(i_v - i_v^0\right) \end{aligned} \tag{3.17}$$

Assuming $i_c \sim i_a \sim i_0$ (no fuel preheating), equation (3.17) simplifies as:

$$\dot{m}_c \; \mathrm{LHV}^0 = Q_r \quad + \dot{m}_f^*(i_f^{in} - i_f^{*0}) \tag{3.18}$$

Under the ideal gas assumption, equation (3.18) becomes:

$$Q_r \quad + \dot{m}_f^* \, c_{p,f} \; (T_{in} - T_0) = \quad \dot{m}_c \; \mathrm{LHV}^0 \tag{3.19}$$

This equation is used for the setup of the S2S model, while for the setup of the PM model it is assumed $Q_r = 0$.

With the S2S radiation model the fluid inlet boundary is considered as a radiant surface, with emissivity ϵ_{in} and radiation temperature T_{rad}, which are used by the solver to calculate the radiation heat exchanged with the surrounding Q_r. The fluid inlet temperature T_{in} and the emissivity ϵ_{in} are assumed as tuning parameters, while T_{rad} is set equal to the adiabatic flame temperature, with 1.15 air-fuel equivalence ratio (FireBridge (2017)). A value of 0.3, typical of blue flames (Sherman (1933)), is taken as first guess for ϵ_{in}.

When using the PM radiation model, the inlet surface is assumed as a diffusely, purely-reflecting surface, while the total temperature (T_{in}) of the injected gas is assumed as the only tuning parameter. The inlet conditions are derived from:

$$\dot{m}_f^* \, c_{p,f} \; (T_{in} - T_0) = \quad \dot{m}_c \; \mathrm{LHV}^0 \tag{3.20}$$

The fluid enters the combustion chamber with uniform velocity, normal to the boundary and with high turbulence intensity of 10% (Westenberg and Rice (1959)).

Burner case

The case of the burner is considered as an adiabatic, solid wall. Its surface emissivity is taken as high as $\epsilon = 0.95$, as both the case of the burner and the heat exchange surface get burnished by the intense heat of combustion.

Heat exchange surface

The heat exchange surface is considered as an isothermal, solid wall with surface emissivity $\epsilon = 0.95$. The assumed wall temperature of 373 K corresponds to the water saturation temperature at normal atmospheric pressure. A similar approach is successfully used by (Buczyński et al. (2015)) to model a small-scale, coal-fired, domestic boiler. In the present configuration of the boiler, the gas region is almost entirely enclosed in the water chamber and surrounded by boiling water: consistently, keeping the entire bounding surface at a uniform temperature proves to be a simpler yet accurate strategy. The convective thermal resistance on the water side is at least two orders of magnitude smaller than that on the exhaust gas side and, therefore, can be neglected. The relevance of the thermal conduction resistance of the solid surfaces is assessed by carrying out a simulation, where all solid boundaries have a thickness of 1.5 mm and a thermal conductivity of 20 W/mK, representative of AISI 304 stainless steel. The discrepancy between the two models is limited to only a $\Delta T = 1K$ in the outlet temperature of the exhaust gas and a difference of 0.1% in the boiler efficiency (defined in (3.22)). In view of these results the thermal conduction resistance of the heat transfer surface can be neglected without impairing the reliability of the model.

Exhaust pipe wall

The exhaust pipe wall (see figure 3.4) is modelled as a solid wall, featuring a specific thermal resistance of 0.2 m^2 K/W. Its inner surface is exposed to the hot combustion gas, while its outer surface is exposed to the atmosphere at temperature ($T_a = 15°$C).

Exhaust outlet

The exhaust outlet is represented by a pressure-outlet boundary condition, where the static pressure of the gas is assigned. As for radiation, the surface is modelled as a black isothermal surface kept at ambient temperature ($T_a = 15°$C).

3.2.2.2 Numerical model

The numerical simulations have been carried out using the commercial, finite-volume package STAR-CCM+ v.11.04.10, with an unstructured polyhedral mesh, whose corresponding surface mesh is shown in figure 3.7. The unstructured polyhedral mesh has been chosen as it allows for an automatic mesh generation process even for complex geometries. The governing equations are solved in *segregate mode* (Ferziger and Perić (2002)), with the SIMPLE algorithm for pressure-velocity coupling and a 2-nd order upwind scheme for the discretization of the convective term. Grid size independence is attained with meshes encompassing about five millions cells, as verified by the convergence of the averaged Nusselt number, reported in figure 3.8. Four millions cells provides a good compromise between accuracy and computational cost.

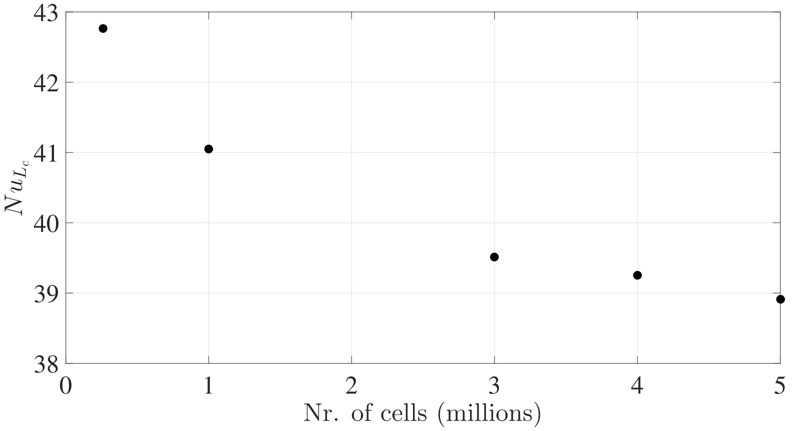

Figure 3.8: Grid size independence based on Nu number.

The Nusselt number, used for the mesh sensitivity analysis, is defined as

$$\text{Nu} \equiv \frac{\overline{q''}\, L_c}{\lambda\, (T_{ref} - T_w)} \tag{3.21}$$

where $\overline{q''}$ is the averaged heat flux through the heat exchange surface, L_c is a characteristic length defined by the ratio of the volume of the gas region to the heat transfer surface area, T_{ref} is the adiabatic flame temperature (at a fixed air fuel equivalence ratio), λ is the thermal conductivity of the combustion gas at T_ref and T_w is the water boiling temperature at normal atmospheric pressure.

3.3 Results and discussion

3.3.1 Selected outcomes of the numerical simulations

3.3.1.1 Reliability of the isothermal condition for the heat exchange surface

The water saturation temperature at ambient pressure is imposed on the outer side of the heat exchange surface. The validity of this assumption is confirmed experimentally, monitoring the temperature at several points on the aforementioned surface (figure 3.10).

The measured temperature on the water side of the fire-tube oscillates within a range of $-1°C \div +2°C$ about the water saturation temperature, under any operative condition of the boiler. The measured steam temperature over the

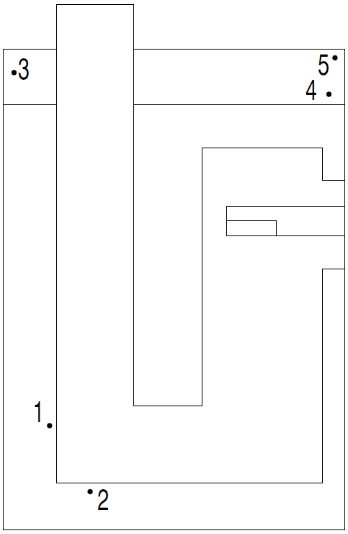

Figure 3.9: Experimental water and steam sampling positions P1, P2, P3, P4, P5.

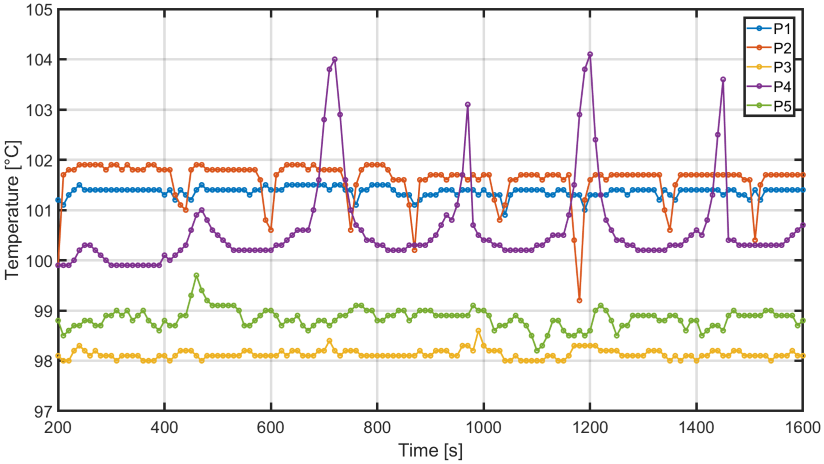

Figure 3.10: Experimental values of water and steam at the external side of the fire tube.

boiling volume does not exceed the value of $105°$C (figure 3.10). The steam temperature exceeds the saturation water temperature due to the decrease of the boiling water level before the refill, when the vapour is exposed to the hot surface of the fire-tube. This condition lasts only few seconds and does not affect significantly the mean steam temperature during the tests (table 3.3).

A sensitivity analysis is carried out to assess the dependence of the exhaust gas temperature T_f and of the boiler efficiency η on the temperature T_b enforced on the outer surface of the exhaust gas zone. The boiler efficiency η is defined as:

$$\eta = 1 - \frac{Q_f}{\dot{m}_c LHV^0} \tag{3.22}$$

where Q_f is the heat lost through the outlet of the flume:

$$Q_f = \dot{m}^*_f c_{p,f}(T_f - T_a) \tag{3.23}$$

The efficiency η for gas boilers can be measured indirectly, according to the prescriptions of the technical regulations (UNI-10389-1:2009 (2009)), which provide the following equation:

$$\frac{Q_f}{\dot{m}_c LHV^0} 100 = \left(\frac{0.66}{21 - [O_2]} + 0.01 \right) (T_f - T_a) \tag{3.24}$$

where $[O_2]$ is the volumetric concentration of oxygen in the exhaust.

Temperature [°C]	P3	P5	P4
Averaged	98.1	100.8	98.9
Standard dev.	0.1	1.2	0.3
Maximum	98.8	105.5	101.3
Minimum	98.0	99.9	98.2

Table 3.3: Experimental steam temperature values.

The results of the sensitivity analysis are shown in figure 3.11. The Logarithmic Sensitivity Factor (LSF) is used as quantitative sensitivity parameter (Buczyński et al. (2015)):

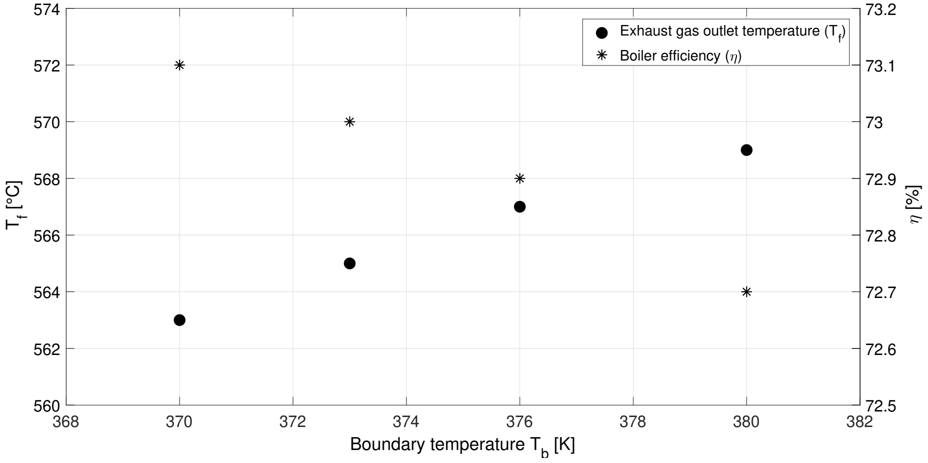

Figure 3.11: Sensitivity analysis for the *heat exchange surface* boundary condition.

$$LSF = f_i = \frac{\partial y}{\partial x}\frac{x}{y} \tag{3.25}$$

where x stands for a model parameter and y represents the model outcome. In the present case:

$$f_1 = \frac{373}{T_f(T_b = 373)}\frac{dT_f}{dT_b} = 0.27 \tag{3.26}$$

$$f_2 = \frac{373}{\eta(T_b = 373)}\frac{d\eta}{dT_b} = -0.2 \tag{3.27}$$

According to the values of f_1 and f_2, variations of T_b induce moderate alterations of T_f and η.

3.3.1.2 Effects of radiation heat transfer in the fire-tube

The marginal difference in the results between the S2S and PM models needs to be further investigated. To this end, we consider the dimensionless Boltzmann number, *Bo*, which provides a quantification of the relative importance of the heat transferred by forced convection and by radiation.

It is defined as (Kunes (2012)):

$$Bo = \frac{\rho c_p u}{\epsilon \sigma T^3} \tag{3.28}$$

The *optical thickness* τ provides an order of magnitude for the attenuation of the radiant intensity through a participating medium:

$$\tau = \bar{a} S \tag{3.29}$$

where $\bar{a}$ is the averaged absorption coefficient and S is the *optical path length*, defined, for arbitrary geometries (Bergman et al. (2011)), as:

$$S = 3.6 V / A \tag{3.30}$$

where V is the volume of gas and A is the radiating surface of V. If $\tau \ll 1$ the following modified Boltzmann number is considered (Kunes (2012)):

$$Bo' = \frac{Bo}{2\tau} \tag{3.31}$$

Even for low Bo, the relative importance of the radiation heat transfer may be minor if τ is very small. The characteristic temperature is defined as the *bulk temperature*; the bulk temperature in each section is then averaged along the entire tube length L.

$$T_{bA} = \frac{\displaystyle\int_A \rho c_p |\mathbf{v}| T dA}{\displaystyle\int_A \rho c_p |\mathbf{v}| dA} \tag{3.32}$$

$$T_b = \frac{\displaystyle\int_L T_{bA} dl}{L} \tag{3.33}$$

$$\overline{Bo} = \frac{\rho(T_b) c_p(T_b) \overline{u}}{\overline{\epsilon} \sigma T_b^3} \tag{3.34}$$

$$\overline{Bo'} = \frac{\overline{Bo}}{2\overline{\tau}} \tag{3.35}$$

where $\overline{u}$ and $\overline{\epsilon}$ are properties averaged inside the corrugated tube zone. The values of the Boltzmann numbers (3.34) and (3.35) are reported in table 3.4, for the case of 100% of thermal power inlet with the PM model:

T_b $[K]$	$\bar{\tau}$	$\rho[kg/m^3]$	$c_p[J/kgK]$	$\bar{u}$ $[m/s]$	$\bar{\epsilon}$	$\overline{Bo}$	$\overline{Bo'}$
1134.7	0.0426	0.32	1281	4.16	0.59	34.81	408.9

Table 3.4: Evaluation of the influence of radiation heat transfer in the corrugated tube zone

According to table 3.4 the impact of radiation heat transfer by the exhaust gas in the corrugated zone is low compared to convection, supporting the use of the S2S radiation model, as it is less expensive than PM. This assumption is confirmed also by the results reported in figure 3.12, showing the radiation heat flux incident onto the heat exchange surface both for the S2S and PM models. The radiation heat transfer is very intense in the combustion chamber, while it is strongly reduced as the exhaust gas flows through the fire tube. In particular, for the S2S model the distribution of the radiant heat flux reflects the main assumption of the model: the radiant heat from the combustion products is intense only near the fluid inlet boundary. In the PM model the volumetric radiation makes the flux more evenly distributed all over the combustion chamber boundary.

3.3.1.3 Validation of the proposed model

Different operative conditions are taken into account in the validation phase, which are representative of the working conditions of the boiler in professional ovens. Experimental and numerical results are compared in table 3.5, for the exhaust gas outlet temperature and for the boiler efficiency. We have chosen these two parameters since are the most important for the energy characterization of such devices. The difference between the numerical and the experimental values of efficiency η does not exceed the experimental error (approximately 2% for all tests, according to the technical regulations, UNI-10389-1:2009 (2009)). The temperature differences for T_f are lower than 10°C. Both the S2S and PM models are in substantial agreement with the experimental measurements, though they require a different computational effort, as reported in table 3.6. The PM model is more computationally-intensive due to the need of solving the Radiative Transfer Equation (3.7) in the whole domain.

In the last column of table 3.5 it is reported the coefficient ε_{th}, defined as if the boiler were a heat exchanger treated with the $\varepsilon - NTU$ method. Of course the analogy needs the assumption that the inlet temperature at the gas side is fixed as the adiabatic flame temperature of the combustion.

$$\varepsilon_{th} = \frac{Q_w}{Q_{max}} = \frac{Q_w}{\dot{m}c_p(T_{ad} - T_w)} \tag{3.36}$$

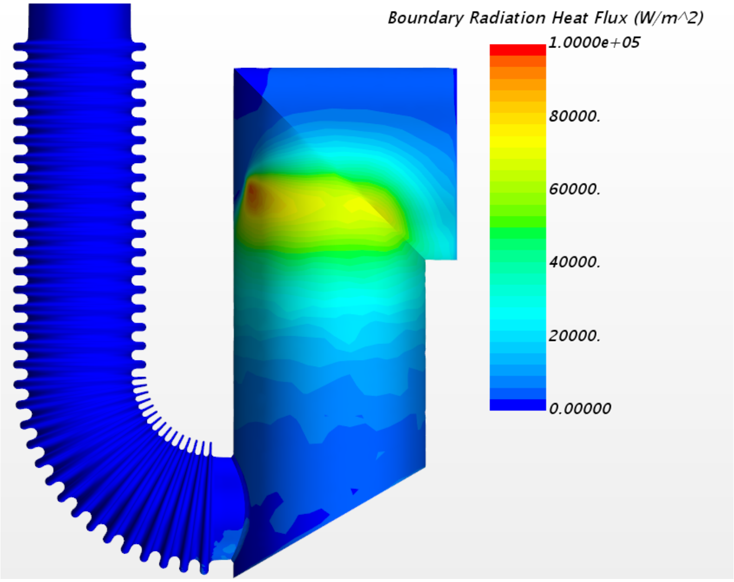

(a) S2S model

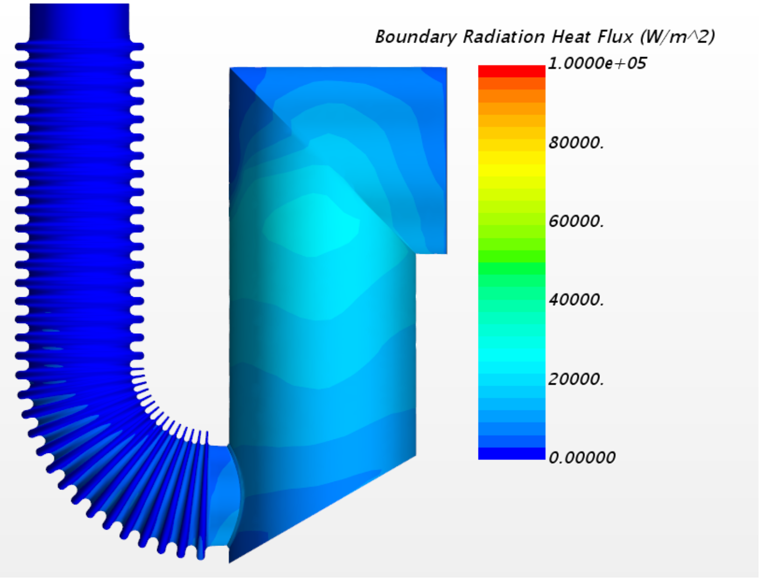

(b) PM model

Figure 3.12: Boundary radiation heat flux.

where T_{ad} is the adiabatic flame temperature, Q_w is the heat power exchanged at the wall, T_w is the water boiling temperature, $\dot{m}$ is the exhaust airflow and c_p is the specific heat calculated at T_{ad}.

rated power [%]	Test	Q_{input} [kW]	η * [%]	T_{out} [°C]	T_{in}/T_{rad}[°C]	ε_{th} **
100	exp.	10.50	74.0 ± 2	564 ± 1.5	-/-	68.6
100	S2S	10.49	73.0	565	1577 / 1627	67.7
100	PM	10.48	73.3	558	1877 / -	68.0
90	exp.	9.44	75.5 ± 2	536 ± 1.5	-/-	70.1
90	S2S	9.43	75.4	540	1577 / 1627	70.0
90	PM	9.42	74.4	535	1877 / -	69.0
68	exp.	7.15	77.9 ± 2	479 ± 1.5	-/-	73.6
68	S2S	7.20	77.1	488	1577 / 1627	72.8
68	PM	7.21	77.9	471	1877 / -	73.6

Table 3.5: Measured and simulated data. exp.: experimental; S2S: simulated results with S2S radiation model; PM: simulated results with PM radiation model; *: according to UNI 10389 for experimental results; **: considering the inlet temperature of the exhausts as the adiabatic flame temperature.

Hardware specification and elapsed time	
CPUs	3 × Intel Xeon Sandy Bridge E5-2670 2.66 GHz
No. iterations to convergence	1000
Elapsed time (S2S model) [s]	4308
Elapsed time (PM model) [s]	14613

Table 3.6: Hardware specification and elapsed time to complete each simulation.

3.3.1.4 Thermal-hydraulic efficiency

The corrugated fire tube yields higher heat transfer rates and pressure drops compared to a smooth pipe. The combined *thermal-hydraulic efficiency* (Stalio and Nobile (2003)) of the corrugated tube and of a smooth fire tube with the same mean diameter are compared. In figure 3.13 the turbulent kinetic energy production (TKP) term (Versteeg and Malalasekra (2007)) is shown on a vertical midplane for the corrugated and the smooth fire-tube. It is evident that the corrugated wall induces a higher TKP, thereby increasing the heat transfer coefficient. Moreover a high value of TKP is present also in the center of the tube: this can be explained by the presence of a shear layer between the outgoing gas flow and the stagnation region, which can be readily identified in figure 3.15, showing the velocity magnitude on a vertical midplane. The induced drag is increased as well. These two effects are compared in terms of the parameter ξ (*thermal-hydraulic efficiency*), defined as (Stalio and Nobile (2003)):

$$\xi = \frac{2St_c/C_{Dc}}{2St_s/C_{Ds}} \tag{3.37}$$

where the subscript *c* and *s* refer to the corrugated and smooth profile of the fire tube, respectively. Only the zone downstream to the elbow, after the combustion chamber, is considered. The Drag Coefficient (C_D) and the Stanton number (St) are defined as:

$$C_D = \frac{F_D}{1/2\rho_b u_b^2 A} \tag{3.38}$$

$$St = \frac{Nu}{RePr} = \frac{\overline{h_c}}{\rho_b c_{pb} u_b} = \frac{\overline{q''}}{(T_b - T_w)\rho_b c_{pb} u_b} \tag{3.39}$$

The subscript *b* indicates *bulk* properties. The radiation heat transfer is of minor importance in this zone of the boiler: therefore, it seems reasonable to use $(T_b - T_w)$ as the representative temperature scale in equation (3.39). The heat flux q'' and the heat transfer coefficient h are averaged over the surface in contact with water.

	T_b $[K]$	Re_{D_h}	Pr	Nu_{D_h}	C_D	St	F_D $[N]$	St/C_D
Corrugated tube	1036	2157	0.67	18.9	0.115	0.0131	0.02	0.114
Smooth tube	1264	1756	0.65	14.4	0.023	0.0127	0.0018	0.552

Table 3.7: Thermal-hydraulic parameters in the fire-tube zone

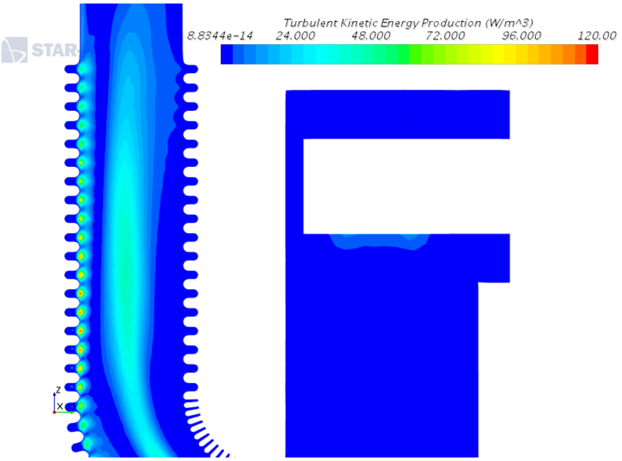

(a) Corrugated fire-tube

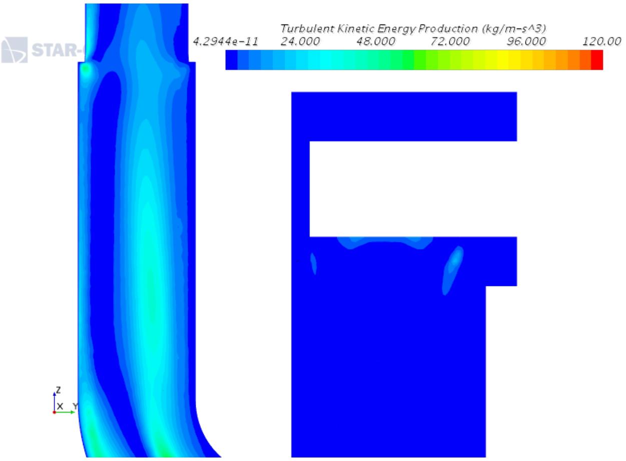

(b) Smooth fire-tube

Figure 3.13: Turbulent kinetic energy production.

According to table 3.7, the corrugated wall features higher Nu_{D_h}, St and C_D. The resulting efficiency ξ is 21%, which means that the pressure drop increases more than the heat transfer.

Exhaust gas temperature contours are shown in figure 3.14 on a vertical midplane. The outer profile of the elbow is very effective in transferring heat, because the stream tends to *squeeze* over it (figure 3.15), resulting in high values of the heat transfer coefficient (figure 3.16). The inner side of the corrugated wall is less efficient, because it is interested by a low velocity region.

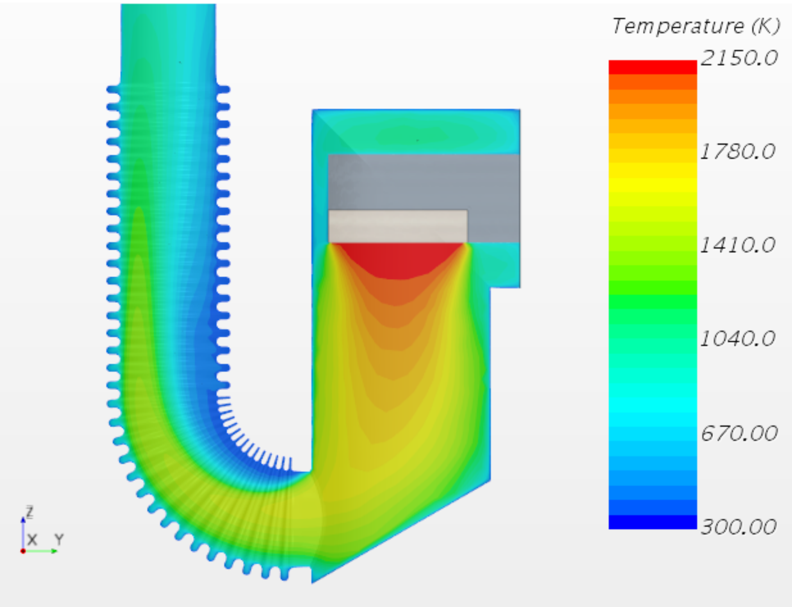

Figure 3.14: Temperature field.

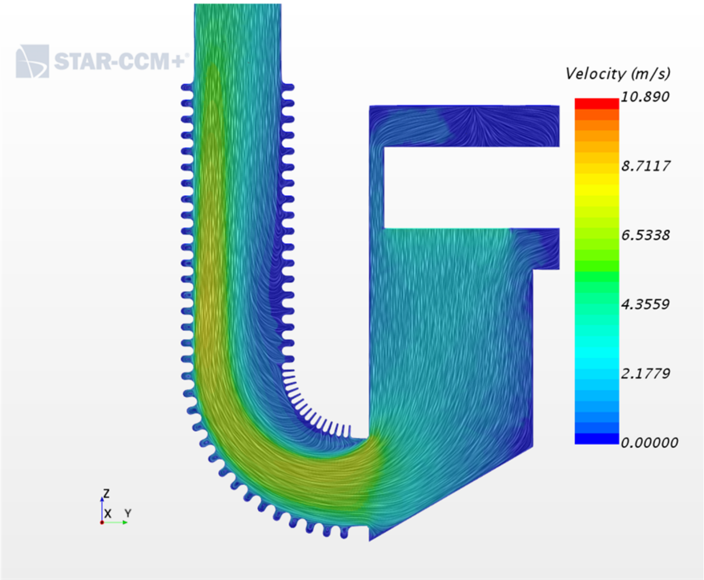

Figure 3.15: Velocity magnitude line integral convolution, Cabral and Leedom (1993).

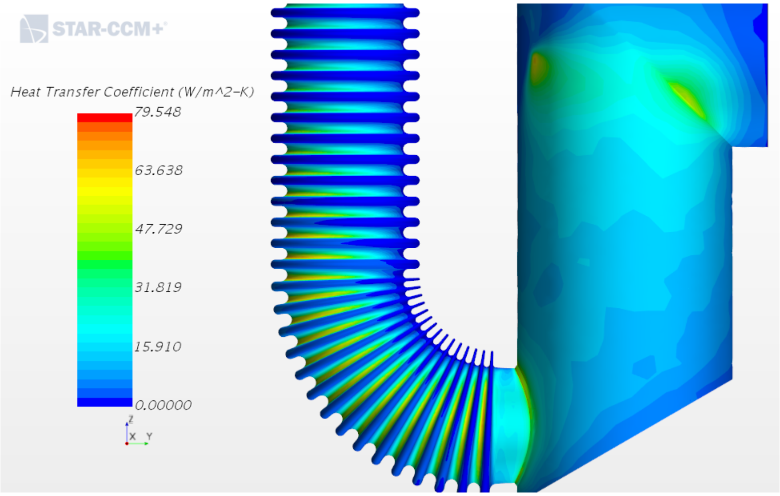

Figure 3.16: Convective heat transfer coefficient referred to the adiabatic flame temperature.

3.4 Concluding remarks

In the present work a numerical tool is proposed to simulate the thermal behaviour of a professional steam generator, or *boiler*, which is used in food service professional ovens. The major difficulties are related to the simulation of the boiling process and the combustion. We propose and validate a reliable and computationally-efficient numerical model for professional gas boilers, which takes into account a simplified modelling of the two aforementioned phenomena. In the first part of the work the thermal model of the boiler is presented, describing in details the thermal system and the boundary conditions. An entire section is dedicated to the simulation of the radiative heat transfer, since it is a very important heat transfer mechanism inside the combustion chamber: two numerical models are compared, Surface-to-Surface and Participating Media. The outcomes from the two models do not differ significantly, but the S2S model requires almost 30% of the computational cost of the PM model. The other simplification is related to the presence of the boiling water: the model describes the steady-state condition of the boiler and in this condition the experiments show that the temperature of the water varies within a relatively narrow range about the saturation temperature at normal atmospheric pressure. Therefore it seems reasonable to consider the presence of the water just with a constant temperature boundary condition of 373 K. A sensitivity analysis, on the range of temperature measured experimentally, shows that the numerical results are weakly dependent on the value of the temperature of the boundary condition. Finally, we believe that the use of computationally-efficient numerical models can be considered a strategic method in industrial design, since they requires a low number of user-defined parameters and low computational cost, without loosing in accuracy.

Chapter 4

Lumped-parameter model for professional ovens

4.1 Introduction and state of the art

In the present work the author will focus on the thermal description of professional ovens. These machines can use either gas or electricity as energy source and can operate in very different working conditions, as in forced convection with dry air (hereinafter *convection mode*), forced convection with steam (hereinafter *steam mode*) and in *combi-mode* (i.e. the customer can choose the percentage of vapour in the cavity). A big fan is responsible both of the internal circulation of the air and of the introduction of external air to control the level of humidity within the cavity. In the present work we will focus on the energy description of an oven which operates only with dry air. Chhanwal et al. (2010) presented a CFD model of an electric heating baking oven. They focused on the radiation heat transfer mechanism that occurs in the cavity, comparing three different radiation models, namely the Discrete Transfer Radiation Model (DTRM), the Surface-to-Surface model (S2S) and the Discrete Ordinates model (DO). The authors conclude that the three models offer almost the same results in quite good agreement with experimental data. Mistry et al. (2011) developed a transient CFD model to simulate the heat transfer within a domestic gas oven. They modelled the coupling between the forced convective flow field and the radiative heat transfer (with participating media). Their model doesn't take into consideration a direct modelling of the flow-thermals through the burner, because they simulate a domain where the burner zone is recovered through a boundary condition. The presented methodology was validated by comparison with experimental data, showing less than 6% discrepancy in thermal field during the preheating phase of the oven. Díaz-Ovalle et al. (2017) presented a CFD model of a domestic electric oven, to study some strategies to reduce the energy consumption during the pre-heating phase. They studied the influence of the geometry of a precise component (the *baffle plate*), on the temperature distribution within the cavity and the time spent to reach the set-point. CFD models are quite computationally-expensive and a very detailed simulation can take a long time: therefore it is wise using simpler models to investigate the overall behaviour of an energy system. Abraham and Sparrow (2004) introduced a predictive numerical model to evaluate the heat transferred to a food load in an electrically heated oven. The model, which uses the lumped-capacitance method, takes into account the natural convection and the radiative heat transfer mechanisms, providing good results with low computational effort for a lot of configurations and it is also experimentally validated. Ramirez-Laboreo et al. (2016) developed a numerical dynamic model of heat and mass transfer for an electric oven. The model is based on a linear lumped parameter structure, reproducing the thermal behaviour of the main components of the oven and of the food load placed in the cavity. An experimental fitted expression is used to take into consideration the evaporation process within the food load and there is a good agreement between the model and the experimental data. Ryckaert et al. (1999) proposed a *model-based* methodology to investigate advanced control algorithm for the dynamic behaviour of an oven. For this purpose, a validated mathematical model representing the thermodynamics of the main components is presented.

In the present chapter we propose a dynamic thermal model for professional ovens, which is able to describe the thermal behaviour of the main components during the pre-heating phase and idle conditions. The idle conditions are considered very important for the design phase, especially for the energy tests required by some standards (i.e. ENERGY STAR label). The lumped-capacitance approach is used to describe the convective and radiative heat transfer processes, dividing the domain in two thermal zones, i.e. the power zone and the cooking zone. The proposed model is finally validated with experimental temperature data.

4.2 Materials and methods

4.2.1 Test rig

The experiments are carried out on the oven Electrolux AoS Touchline 10 GN1/1 (figure 4.1), a professional machine that is able to cook up to 10 trays GN 1/1 [1]. The internal cavity of the oven is 760x680x650 mm (height x width x depth), with an internal volume of $0.336 m^3$. The maximum power supply is 17.5 kW (400

---

[1] The standard GastroNorm is used for professional food service trays and in particular GN 1/1 corresponds to a stainless steel AISI 304 tray with 530x325 mm in dimensions

V in AC three-phase 50Hz), when both the resistor heaters of the cavity and of the electric boiler are activated (Air-o-Steam (2017)). Type T thermocouples are used to monitor the temperatures inside the cavity and acquired by the acquisition system Yokogawa MX100. The experimental tests are carried out with the oven in convection mode, during the pre-heating phase and during the steady state in idle mode [2]. The fan rotates at constant speed of 1500 rpm and the temperature set-point is about 190°C with 5 K of dead band.

Figure 4.1: Electrolux AoS Touchline 10 GN1/1

4.2.2 Physical model

In this section we present a physical and numerical model of the professional oven described above. The proposed methodology is applicable to any professional oven that has a working principle similar to the one described here. The main characteristic of this model is the definition of two distinct zones: the *Power zone*

---

[2] The energy consumption in idle mode is important for the technical standards.

and the *Cooking zone*. In figure 4.2 a schematic representation of the oven is presented (in blue the Power zone and in green the Cooking zone). A solid wall, named *suction wall*, separates the cooking region from the region where the fan and the resistors are (figure 4.3). The presence of the suction wall creates a plenum region to uniform the airflow conveyed to all the trays: in particular the central hole of the wall corresponds to the suction zone of the fan and the air is then conveyed from the fan outlet to the cavity through the lateral openings all around the perimeter of the wall.

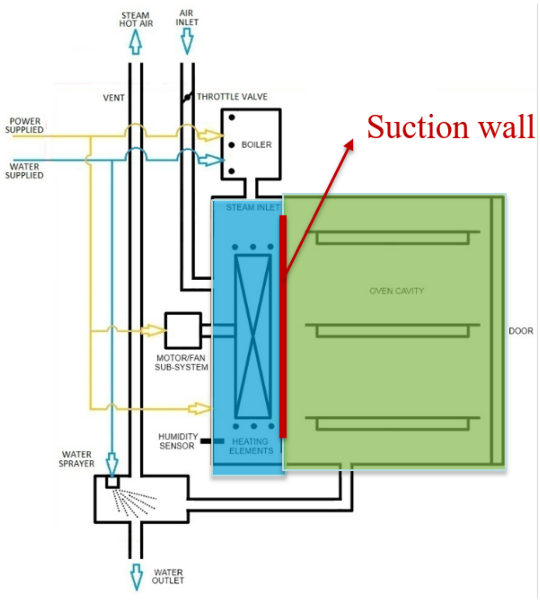

Figure 4.2: The Power zone and the Cooking zone.

The definition of these two zones is due to the impossibility to define a single value of temperature for the air in the cavity, because in the Power zone a high power density is present due to the presence of the heating elements. The thermal behaviour of the oven is modelled by the lumped capacitance method, i.e. all the components are modelled as lumped elements with a specific temperature, capacity, density and volume. The elements can exchange mass and heat (conduction, convection and radiation). The proposed model is analog to an electric circuit, where the potentials are the temperatures, capacitors correspond to the thermal capacity of each element and the electric resistances represent the thermal resistances between the elements. In the present work the air is the only fluid present in the cavity, moreover all the mechanical components (fan, auxiliary equipments, etc.) are represented as thermal masses since they have a big impact on the thermal inertia of the system. The presence of the food is not considered. The

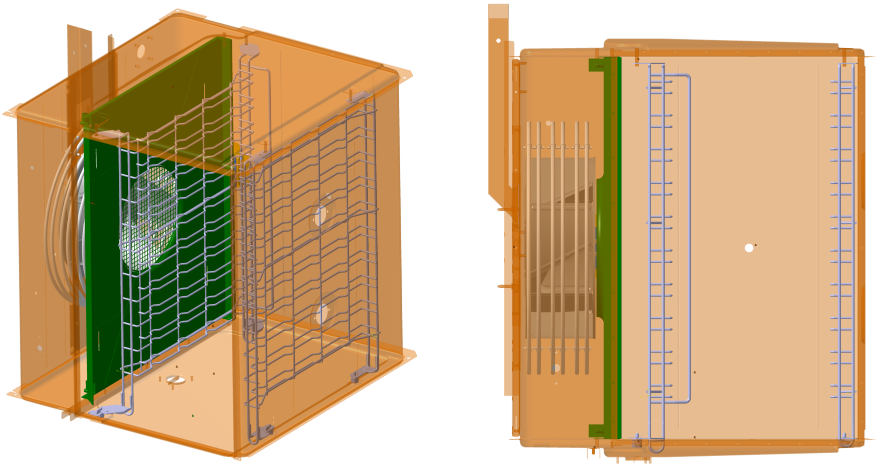

Figure 4.3: CAD representation of the cavity of the oven with the suction wall in green.

case of the oven is made of a metal sheet (AISI 304,$\lambda = 17\,W/mK$, $\rho = 7800\,kg/m^3$ and $c = 480\,J/kgK$), which is covered by a thick layer of fiber-glass insulating material ($\lambda = 0.055 W/mK\,@150°C$, $\rho = 40\,kg/m^3$ and $c = 840\,J/kgK$). Spatial discretization is considered for the walls (hereinafter the i-th wall is indicated with the subscribe w_i), divided mono-dimensionally in isothermal layers. The layers are numbered starting from the external one (hereinafter indicated with the subscribe w_{i1}) to the internal one (hereinafter indicated with the subscribe w_{is}). The total number of walls is indicated with N.

4.2.2.1 Power zone modelling

The logical scheme of the Power zone is represented in figure 4.4: this zone is characterized by the presence of the heaters, which are tubular resistors with an internal region where the thermal power is generated by the Joule effect and an external region. Two nodes are dedicated to the resistors, corresponding to the two regions mentioned and the thermal power is represented by a current generator connected to the internal node. The external node interacts with the internal one by conduction, with the air by convection and with the solid walls by radiation. The fan and the other accessories are considered as lumped thermal mass nodes (with the subscribe mP). The fan is responsible of the enthalpy flux exchanged between the Power zone and the Cooking zone, according to the recirculated mass flow. This mass flow is retrieved by CFD simulations.

The set of algebraic equations, representing the behaviour of the power zone,

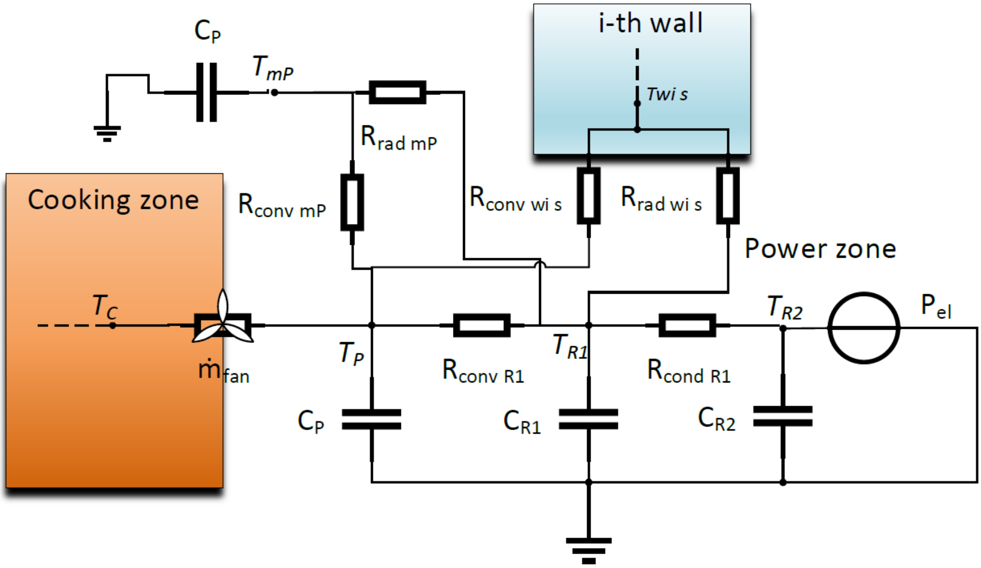

Figure 4.4: The electric scheme of the Power zone.

is presented below:

$$\begin{aligned} V_P \rho_P c_P \frac{T_{P,n} - T_{P,n-1}}{t_n - t_{n-1}} &= \sum_i^N h_{conv\, w_i s} A_{w_i s}(T_{w_i s,n} - T_{P,n}) + h_{conv\, mP} A_{mP}(T_{mP,n} - T_{P,n}) + \\ &+ h_{conv\, R1} A_{R1}(T_{R1,n} - T_{P,n}) + \dot{m}_{fan} c_P (T_{C,n} - T_{P,n}) \end{aligned} \tag{4.1}$$

On the left the capacitive term is discretized by a first order time scheme, on the right side a series of terms represents all the heat exchanges of the Power node (which represent the air) with the surrounding: in order, the convection heat transfer with all the N walls, the convection heat transfer with the thermal mass with the second term, the convection heat transfer with the resistor external node and the enthalpy flux between the Power zone and the Cooking zone due to the air flow recirculated by the fan.

$$\begin{aligned} V_{R1} \rho_{R1} c_{R1} \frac{T_{R1,n} - T_{R1,n-1}}{t_n - t_{n-1}} &= \frac{A_{R1}}{R_{cond\, R1}}(T_{R2,n} - T_{R1,n}) + h_{conv\, R1} A_{R1}(T_{P,n} - T_{R1,n}) + \\ &+ \sum_i^N P_{rad\, w_j s,n} + P_{rad\, mP,n} \end{aligned} \tag{4.2}$$

The equation (4.2) describes the temperature evolution of the external resistor node: on the right side all the terms that contribute to the temperature evolution are shown, namely the conductive heat transfer between the internal node and the external node, the convective heat transfer with the Power node, the radiative heat transfer with the walls and the radiative heat transfer with the items present in the oven (described as thermal masses).

$$V_{R2}\rho_{R2}c_{R2}\frac{T_{R2,n}-T_{R2,n-1}}{t_n-t_{n-1}} = \frac{A_{R1}}{R_{cond\,R1}}(T_{R1,n}-T_{R2,n})+P_{el,n} \tag{4.3}$$

The equation (4.3) describes the temperature evolution of the resistor internal node: the derivative term on the left is balanced by the conduction heat transfer with the external node and the power generation by the Joule effect.

$$V_{mP}\rho_{mP}c_{mP}\frac{T_{mP,n}-T_{mP,n-1}}{t_n-t_{n-1}} = h_{conv\,mP}A_{mP}(T_{P,n}-T_{mP,n})+P_{rad\,mP,n} \tag{4.4}$$

The equation (4.4) shows the thermodynamics of the thermal masses present in the Power zone: the temperature evolution is due to the convective heat transfer with the Power zone node and the radiation heat transfer with the resistor external node.

$$\begin{aligned} V_{w_i s}\rho_{w_i s}c_{w_i s}\frac{T_{w_i s,n}-T_{w_i s,n-1}}{t_n-t_{n-1}} &= h_{conv\,w_i s}A_{w_i s}(T_{P,n}-T_{w_i s,n})+ \\ &+ \frac{\lambda}{\Delta x}A_{w_i s}(T_{w_i s-1,n}-T_{w_i s,n})+\sum_{j}^{N}(1-\delta_{ij})P_{rad\,w_j s,n} \end{aligned} \tag{4.5}$$

The equation (4.5) indicates the temperature evolution of a generic superficial internal wall node of the Power zone: on the right side we can find the convective heat transfer with the Power node, the conduction heat transfer with the adjacent wall node (s-1) and finally the radiation heat transfer with the resistor external node. The subscript j indicates a wall different than the $i-th$.

$$\begin{aligned} V_{w_i s-1}\rho_{w_i s-1}c_{w_i s-1}\frac{T_{w_i s-1,n}-T_{w_i s-1,n-1}}{t_n-t_{n-1}} &= \frac{\lambda}{\Delta x}A_{w_i s-1}(T_{w_i s-2,n}-T_{w_i s-1,n})+ \\ &+ \frac{\lambda}{\Delta x}A_{w_i s-1}(T_{w_i s,n}-T_{w_i s-1,n}) \end{aligned} \tag{4.6}$$

The equation (4.6) describes the temperature dynamics of a generic wall internal node: the only heat transfer mechanism is the conduction with the adjacent nodes.

$$V_{w_i1}\rho_{w_i1}c_{w_i1}\frac{T_{w_i1,n}-T_{w_i1,n-1}}{t_n-t_{n-1}}=\frac{\lambda}{\Delta x}A_{w_i1}(T_{w_i2,n}-T_{w_i1,n})+h_{conv\,e}A_{w_i1}(T_e-T_{w_i1,n}) \tag{4.7}$$

The equation (4.7) is referred to the wall external node in contact with the external environment: thus the node communicates by conduction with the interior adjacent wall node and by convection with the external ambient.

4.2.2.2 Cooking zone modelling

The Cooking zone is represented by the electric scheme shown in figure 4.5: the heat is transferred in this zone by the enthalpy flux exchanged with the Power zone and it is the only zone accessible by the chef by the presence of the glass door. The latter is composed by two layers of 6 mm of glass with an air gap of 45 mm between them and it is modelled with two nodes: the internal node is representative of the internal glass layer (hereinafter with the subscript $g1$) and the external node in contact with the environment (hereinafter with the subscript $g2$). The two *glass* nodes interact with each other by means of an overall thermal resistance due to the air gap (R_g, UNI-EN-ISO-6946:2008 (2008)).

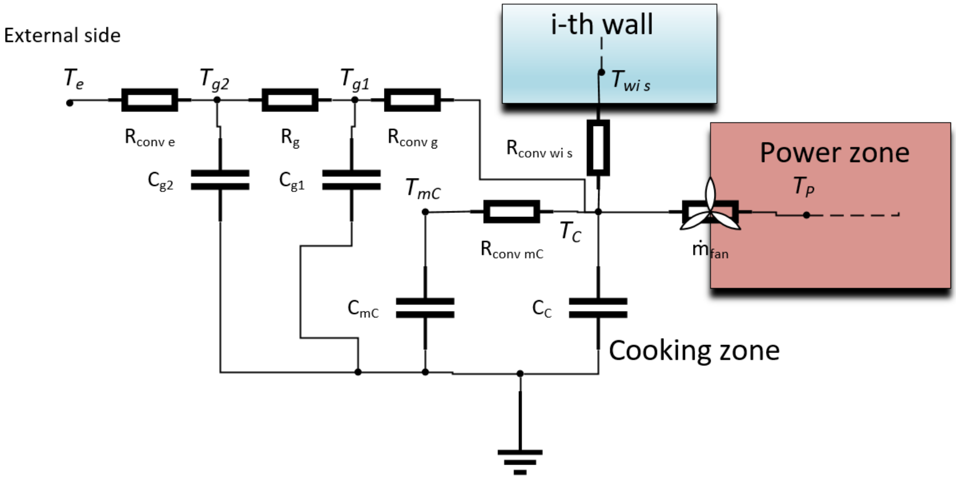

Figure 4.5: The electric scheme of the Cooking zone.

The set of discretized equation for the Cooking zone is shown below:

$$\begin{aligned} V_C \rho_C c_C \frac{T_{C,n} - T_{C,n-1}}{t_n - t_{n-1}} &= \sum_i^N h_{conv\, w_i s} A_{w_i s} (T_{w_i s,n} - T_{C,n}) + \\ &+ h_{conv\, mC} A_{mC} (T_{mC,n} - T_{C,n}) + \dot{m}_{fan} c_C (T_{P,n} - T_{C,n}) \end{aligned} \tag{4.8}$$

The equation (4.8) describes the air temperature evolution of the Cooking zone: the Cooking zone node exchanges convective heat with the N walls, convective heat with the thermal masses and enthalpy flux due to the recirculating fan airflow.

$$V_{mC} \rho_{mC} c_{mC} \frac{T_{mC,n} - T_{mC,n-1}}{t_n - t_{n-1}} = h_{conv\, mC} A_{mC} (T_{C,n} - T_{mC,n}) \tag{4.9}$$

The equation (4.9) indicates the energy balance for the thermal masses present in the Cooking zone: in this case the convective heat transfer with the Cooking zone node is the only term that contributes to the temperature evolution.

$$\begin{aligned} V_{w_i s} \rho_{w_i s} c_{w_i s} \frac{T_{w_i s,n} - T_{w_i s,n-1}}{t_n - t_{n-1}} &= h_{conv\, w_i s} A_{w_i s} (T_{C,n} - T_{w_i s,n}) + \\ &+ \frac{\lambda}{\Delta x} A_{w_i s} (T_{w_i s-1,n} - T_{w_i s,n}) + \sum_j^N (1 - \delta_{ij}) P_{rad\, w_j s,n} \end{aligned} \tag{4.10}$$

The equation (4.10) describes the evolution of the temperature of the superficial internal wall node in the Cooking zone: the equation is analog to the (4.5).

$$V_{g1} \rho_{g1} c_{g1} \frac{T_{g1,n} - T_{g1,n-1}}{t_n - t_{n-1}} = h_{conv\, g1} A_{g1} (T_{C,n} - T_{g1,n}) + \frac{A_{g1}}{R_g} (T_{g2,n} - T_{g1,n}) \tag{4.11}$$

$$V_{g2} \rho_{g2} c_{g2} \frac{T_{g2,n} - T_{g2,n-1}}{t_n - t_{n-1}} = h_{conv\, e} A_{g2} (T_e - T_{g2,n}) + \frac{A_{g2}}{R_g} (T_{g1,n} - T_{g2,n}) \tag{4.12}$$

The two equations (4.11) and (4.12) describes the temperature evolution of the two nodes used to represent the glass door. The internal node (g1) communicates by convection with the Cooking node and by an overall thermal resistance with the external node (g2).

Both the Power zone and the Cooking zone are enclosed by the walls of the cavity, which are sheet metal plates covered by insulating material. The model takes into consideration both the presence of the plates and the insulating material, in figure 4.6 the respective electric scheme is presented.

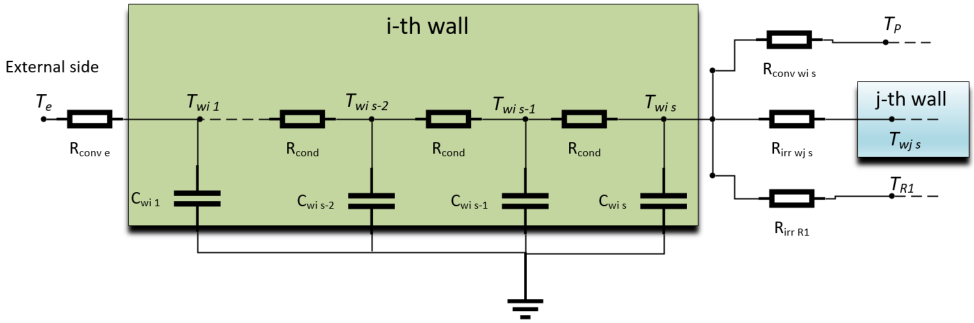

Figure 4.6: The electric scheme of the walls.

4.2.2.3 Radiation heat transfer

The radiation heat transfer is a fundamental mechanism in professional ovens, since it has a big impact due to the high temperature differences between the heaters and the surrounding: this is particularly true for the Power zone in the considered domain. In building energy simulations (Testi et al. (2015) and Grassi et al. (2011)) radiation is commonly modelled by the linearization theory (Bonacina, Cavallini, et al. (1989)), which considers the radiation as a heat transfer coefficient that multiplies the temperature difference between the two elements. In our model, we have decided to treat the radiation without the linearization method, implementing the *net radiation method for enclosures* (Siegel and Howell (1992)). The radiation heat power exchanged by a surface with the surrounding can be expressed by equation (4.13), where *i* is the i-th surface and δ_{ij} is the Kronecker function. Air is considered transparent to the radiation flux.

$$\sum_{j=1}^{N}\left(\frac{\delta_{ij}}{\epsilon_j} - F_{i-j}\frac{1-\epsilon_j}{\epsilon_j}\right)\frac{P_{irr\,w_j s,n}}{A_j} = \sum_{j=1}^{N}(\delta_{ij} - F_{i-j})\sigma T^4_{j,n-1} = \sum_{j=1}^{N} F_{i-j}\sigma(T^4_{i,n-1} - T^4_{j,n-1}) \tag{4.13}$$

The view factors are calculated by the Contour Double Integral Formula (Joy (2014)), implemented numerically in a $Matlab^{©}$ script by Lauzier (2004). The radiation is treated with an explicit scheme, considering for the n-th timestep the temperature of the timestep n-1.

4.3 Results and discussion

4.3.1 Tuning procedure

The presence of the fan inside the cavity implies a strong forced convection heat transfer process between the air and the solid surfaces. A tuning procedure has been implemented to have a good estimation of these coefficients from the comparison with experimental data. The following four coefficients have been selected as tuning parameters:

- The average convective coefficient between air and walls: $h_{conv\,ws}$;
- The average convective coefficient between air and the thermal resistors, $h_{conv\,R1}$;
- The average convective coefficient between air and the thermal masses multiplied by the exchange area, for the Power zone, $h_{conv\,mP}A_{mP}$;
- The average convective coefficient between air and the thermal masses multiplied by the exchange area, for the Cooking zone, $h_{conv\,mC}A_{mC}$.

The tuning procedure considers the match between numerical and experimental temperature data during the pre-heating phase and during the steady-state phase. In particular the power zone experimental temperature has been used in this work. In figure 4.7 the best fitting of experimental and temperature data, obtained from the best combination of the tuning parameters, is shown. The tuning parameters have been investigated in the following ranges: $h_{conv\,ws}$=[10:40] W/m^2K, $h_{conv\,R1}$=[100:160] W/m^2K, $h_{conv\,mP}A_{mP}$=[20:100] W/K and $h_{conv\,mC}A_{mC}$=[20:100] W/K. The choice of the best configuration of tuning parameter is done minimizing the average realtive error between the experimental and the numerical data. In order to check the physical meaning of the resulting values, for the first two coefficients it was possible to compare the results with the values obtained by semi-empirical correlations ((4.14) and (4.15), Lienard IV and Lienard V (2003), Bejan (2004)). In particular for the coefficient between the air and the walls a correlation valid for isothermal flat plates is used and reported in equation (4.14).

$$Nu = \frac{h_{conv\,ws}L}{\lambda} = 0.037Re_L^{4/5}Pr^{1/3} \qquad 5 \cdot 10^5 < Re_L < 10^7 \tag{4.14}$$

where the Reynolds number is retrieved from CFD calculated values of velocity (not reported here for brevity) and L is the characteristic length of the wall. For the convective coefficient between the air and the tubes of the resistors, a correlation valid for the crossflow across tube banks is used and reported in equation (4.15).

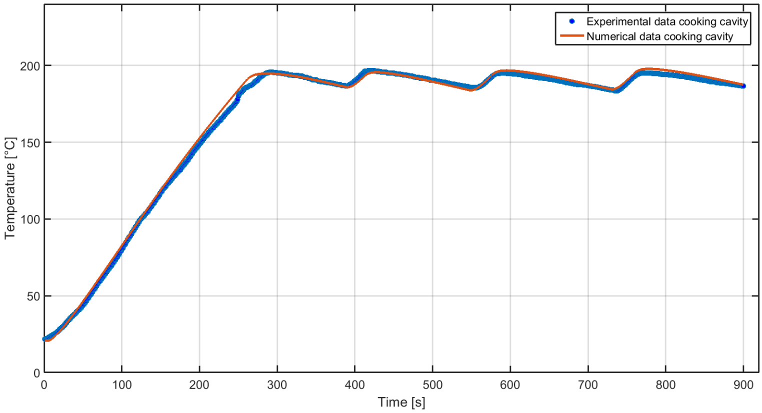

Figure 4.7: The best fitting of the experimental data.

$$Nu = \frac{h_{conv\,R1}D}{\lambda} = C_2 C Re_D^m Pr^{0.36} \qquad 1 < Re_D < 2 \cdot 10^4 \tag{4.15}$$

Where the Reynolds number is always retrieved from the CFD calculations and D is the diameter of the resistors. The coefficients C_2, C, m depend on the geometry of the tubes. For the other two tuning coefficients, respectively $h_{conv\,mP}A_{mP}$ and $h_{conv\,mC}A_{mC}$, we don't have semi-empirical correlations. The results of the tuning procedure are reported in table 4.1.

Coefficient	Tuning value	Correlation value
$h_{conv\,ws}\ [W/m^2K]$	20	27
$h_{conv\,R1}\ [W/m^2K]$	125	141
$h_{conv\,mC}A_{mC}\ [W/K]$	70	-
$h_{conv\,mP}A_{mP}\ [W/K]$	75	-

Table 4.1: Comparison between the values of the unknown coefficients from the tuning procedure and from the correlations.

The order of magnitude of the convective coefficients is in line with the one calculated with the correlations, the results are considered satisfactory.

4.3.2 Thermodynamic behaviour of the oven

In this section we present the simulated thermal behaviour of the oven, considering a set-point of 190°C with 5K of dead band for the activation of the heating power based on the temperature of the Power zone. In figure 4.8 the simulated temperatures are shown: during the ramp-up of the pre-heating phase the temperature of the resistor is much higher than the one of the walls and this leads to a high radiation heat transfer, as it can be seen from figure 4.9. After the pre-heating phase the radiation heat transfer decreases significantly, but in the pre-heating phase it represents an important contribution to the thermal power delivered by the resistors. The figure 4.10 shows that the resistors have a high thermal inertia and require a high amount of power, indeed the total heating power is 16 kW and the maximum thermal power exchanged by the resistor with the surrounding is almost 13 kW at the end of the pre-heating phase. The difference between the total heating power and the power exchanged with the surroundings contributes to the internal energy of the heating elements.

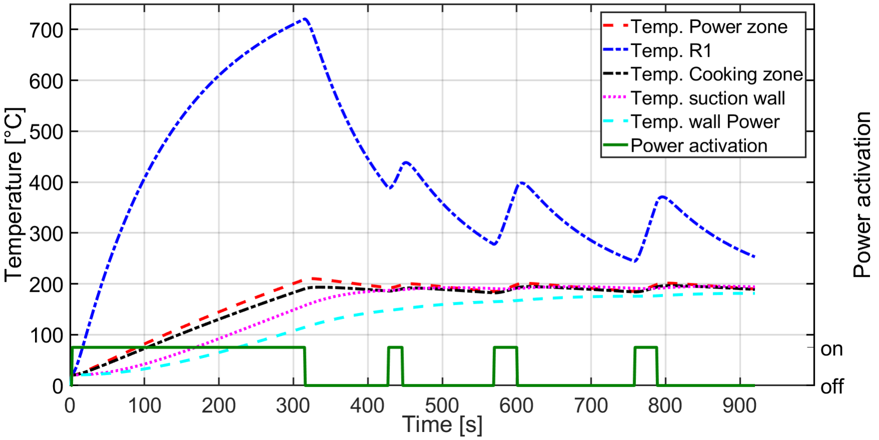

Figure 4.8: Simulated temperature data for the pre-heating and the steady-state.

In figure 4.8 the temperature difference between the cavity walls and the suction wall is shown. The walls that communicate with the insulating layer exchange heat flux with the fiber-glass, consequently they need more time to reach the steady-state. On the contrary the suction wall has a faster dynamics, governed only by the thermal inertia of the layer of stainless steel (1.5 mm), which is present anyway also in the walls. The need of the use of two nodes for the Power zone and for the Cooking zone is clear if we compare the figures 4.8 and 4.11: the Cooking zone has a temperature shift especially during the pre-heating phase and the first period of the steady-state, then the two temperatures tend to

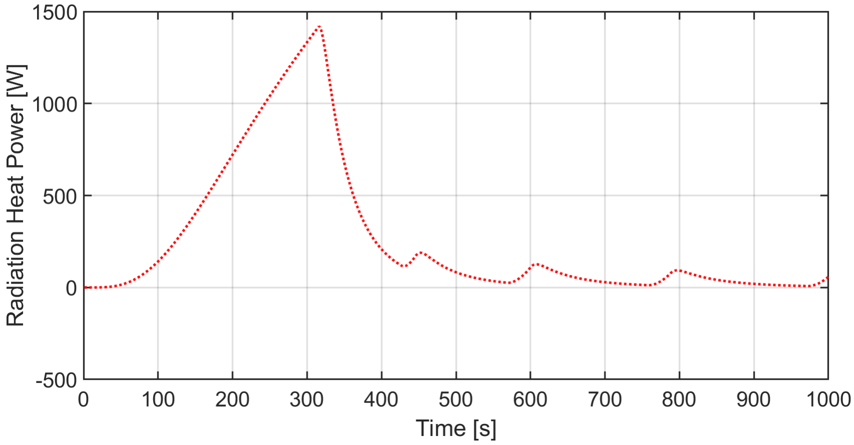

Figure 4.9: Radiative power from the resistors.

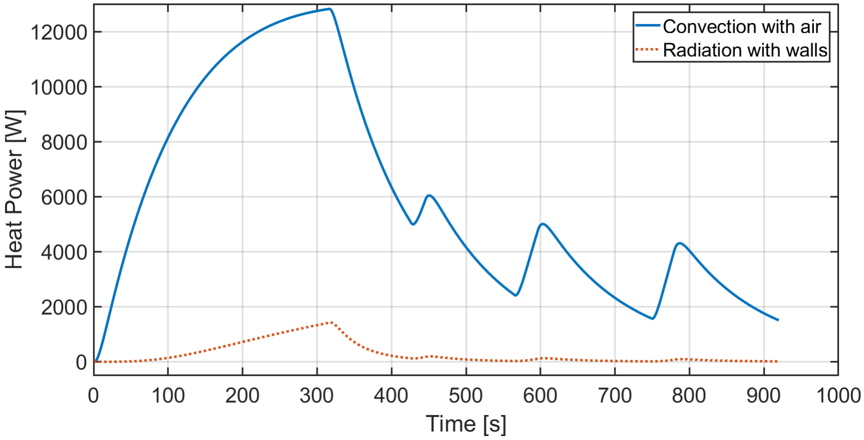

Figure 4.10: Convection and radiative thermal power from the resistors.

equilibrate the gap. For the two nodes of the resistors the gap between the two nodes remains also during the steady-state, mainly due to the high power density that the internal node receives.

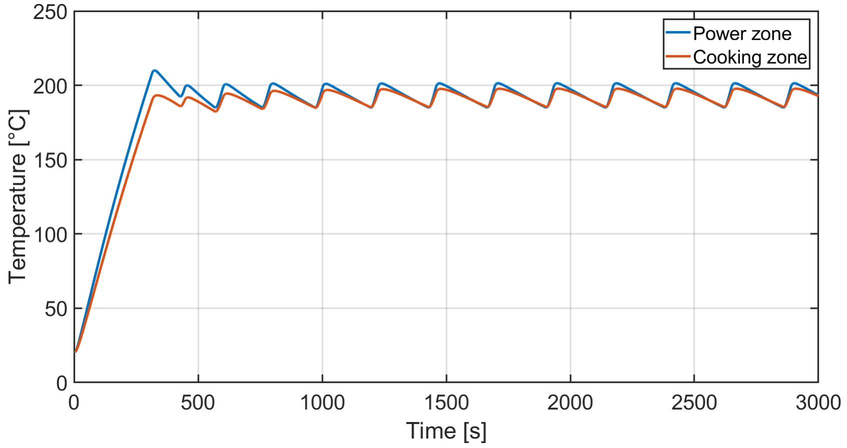

Figure 4.11: The temperature gap between the Power zone and Cooking zone.

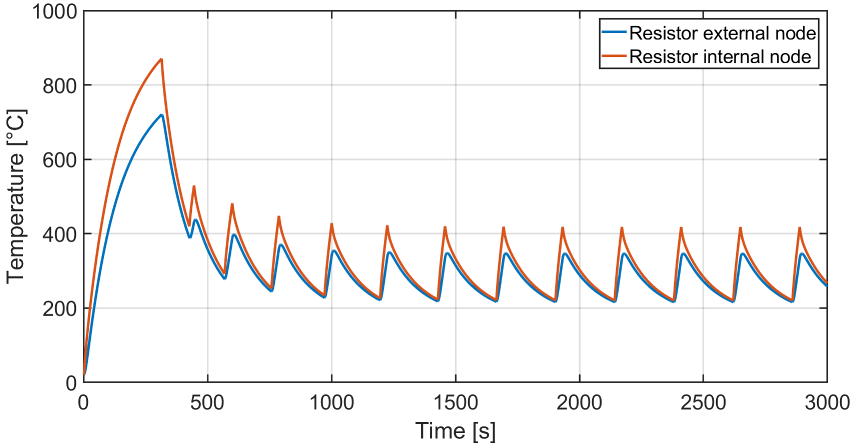

Figure 4.12: The temperature gap between the internal and external nodes of the resistor.

As practical application of the proposed model, here we report the effect of the thickness of the insulating material on the energy consumption (figure 4.13). It is interesting to notice that an increase of thickness above a certain threshold has no more benefits for the energy consumption. This result can be explained by considering that on one side we are increasing the thermal resistance towards the external ambient (except for the losses through the glass door), on the other side we are also increasing the thermal capacity of the insulating layer, spending more energy to reach the steady state. Figures 4.14 and 4.15 show the temperature distributions within a wall for three representative times for two test cases (insulating layers of 4 cm and 10 cm). After 500 seconds in the wall with less insulating material the initial transient phase is ending and the temperature profile becomes linear (steady state condition) after 1000 seconds. On the contrary for the thicker wall after 1000 seconds the insulating material is still in transient state and additional energy is required to reach the linear temperature profile. However with a thicker insulating layer the temperature drop is higher, which means a lower heat power exchanged with the ambient. Finally we can say that after 3000 seconds of working condition, the reduction in heat losses through the external environment with a thicker insulating layer are compensated by the higher energy required to warm up the insulating material itself.

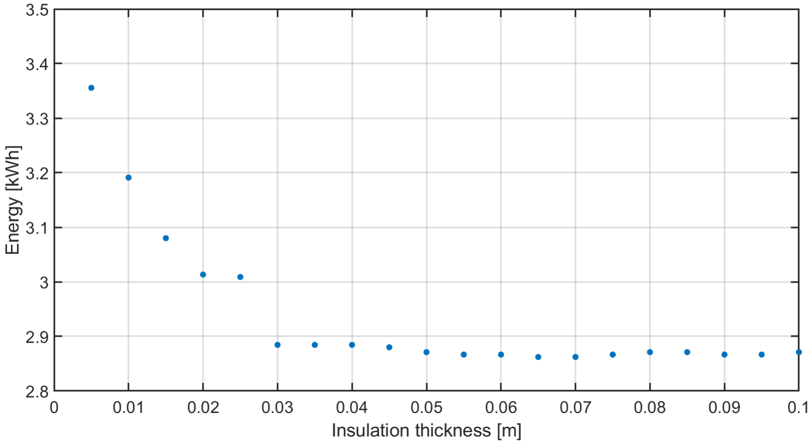

Figure 4.13: The effect of the insulation thickness on the energy consumption.

The present model can be used also for evaluations on energy consumption in idle mode: energy consumption is different between the warm up transient phase and steady state conditions. The warm up transient phase ends when the air temperature reaches the 95% of the set point temperature from a lower or higher set point. During the warm up of the cavity, the energy is prevalently used to heat up the resistors and the thermal masses present in the oven (figure 4.16); only a small percentage is used to bring the air at the set point temperature. In figure 4.16 the energy distribution within the oven for three transient phases are reported: the three graphs represent the energy spent in the transient period until the temperature reaches the 95% of the set point temperature, subdivided in

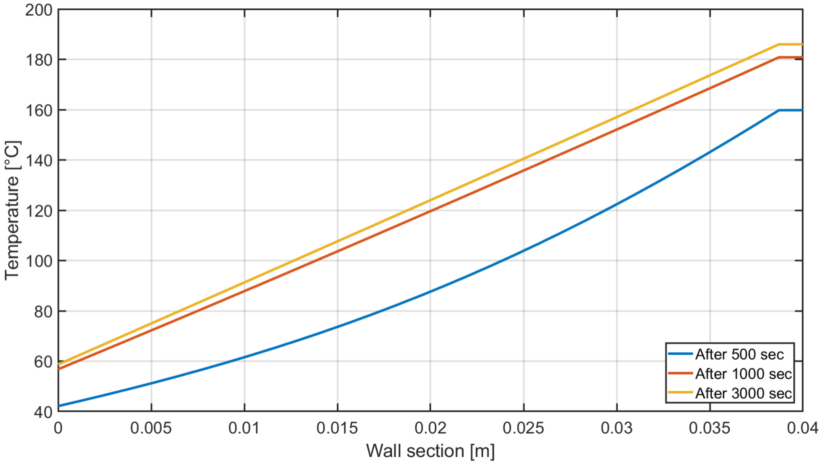

Figure 4.14: Temperature profile within the wall for the insulation thickness of 4 cm.

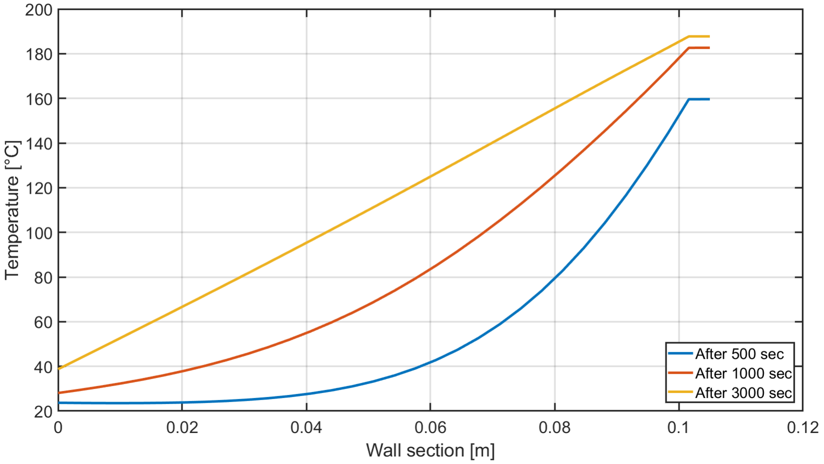

Figure 4.15: Temperature profile within the wall for the insulation thickness of 10 cm.

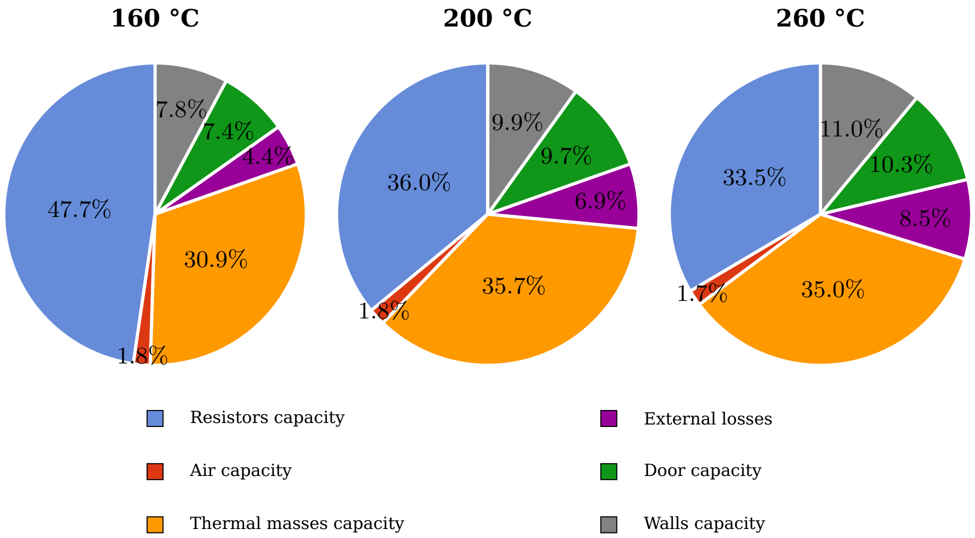

Figure 4.16: Subdivision of the electric energy in the oven during the transient phase, at three different air set point temperatures

several contributions. The set point $160°C$ is achieved in 220 seconds, while $200°C$ is achieved in 300 seconds and $260°C$ is achieved in 380 seconds. The energy lost from the cavity, as expected, increases with the set point temperature and also the energy stored by the thermal masses, walls and door. On the contrary the energy stored by the resistors decreases with the set point temperature, this is because the transient phase becomes longer and after reaching a high temperature they exchange all the heat flux by convection and radiation, without storing energy any-more.

During the steady-state condition all the energy delivered to the thermal system is used to compensate the thermal losses toward the external environment, consequently the heat capacities of the elements don't play a role if we take into account a period sufficiently long to be considered statistically in steady-state.

4.4 Concluding remarks

A numerical lumped-parameter model has been presented in this chapter: the model is based on the lumped-capacitance method, which has the capability of predicting accurately the thermodynamic performance of the oven with low computational efforts. The thermal system is divided in two zones, the power zone and the cooking zone, which are representative respectively of the region in which the thermal power is generated and the region in which the food is placed. The oven works mainly in forced convection, thanks to the presence of a centrifugal fan in the power zone, consequently an estimation of the convective heat transfer coefficient is fundamental to simulate the heat transfer mechanisms. A tuning procedure has been developed to find the values of the unknown convective coefficient that ensure the best fitting of the numerical model with experimental data. The radiation heat transfer is simulated as well, based on the so-called net radiation method for enclosures. The contribute of the radiation can not be neglected, especially during the warm-up phase.

The model is finally used to describe the thermodynamic behaviour of the professional oven, in terms of temperature evolution of the main components and energy evaluations.

Future works are related to:

- A comparison of the model with more experimental data in different cooking modes;
- A complete tuning procedure to make the model more robust when different operative conditions are simulated;
- The introduction of the hygrometric balance to simulate the presence of the steam in combi-mode;
- The simulation of the presence of the food in the cooking zone as thermal load.

Chapter

5

Conclusions

The main objective of the work is to provide accurate, robust and computationally-efficient design methods for selected flow and heat transfer configurations, relevant to the food processing industry. Keep the Physics as simple as possible is the cornerstone of this research: simple models are preferred over complex, yet more accurate ones, provided they require a reduced number of ad-hoc parameters and yield a reasonable accuracy for industrial design. The proposed models are validated over a large range of operative conditions, by comparison with experimental data obtained from test rigs specifically designed and built. Thanks to their characteristics, the models can be easily used in optimization processes, which are considered fundamental during the product development to maximize the efficiency and the performance of industrial machines. The robustness of these models permits to investigate different working conditions and geometries, with a very low number of tuning parameters.

As regards the simulation of the jet impingement technology for thawing processes, a wise strategy consists in combining a three-dimensional, unsteady CFD model for estimating the heat transfer coefficient distribution on the surface of a target object with a computationally efficient heat conduction simulator, aimed at deriving the temperature distribution within the target itself. This approach allows to simulate long thawing processes with reasonable computational cost. Though numerical simulation allows to serive a huge amount of data, it is crucial in industrial design to feature the *performance* of innovative physical processes, devices, operation strategies by a limited set of easy-to-grasp *numbers*, or *performance indicators* (PI). Three PIs are proposed to assess the quality of a thawing process. The performance of one-side and two-side impingement technologies have been assessed, in terms of thawing rate and risk of bacterial contamination. The developed methodology is a solid basis for future studies, which can be focused on several aspects: the existing model takes into consideration a constant thawing air temperature, but it will be interesting to implement a multi set-points cycle, in order to find the best profile that minimizes the thawing indicators. Another interesting topic is the description of the water evaporation losses, which are important for the weight loss in thawing process and require the description of the water migration at the surface of the food.

A design method for gas-fired boilers for professional *combi* ovens is proposed and validated. It is based on two key simplifying assumptions: the combustion process taking place in the combustion chamber does not need to be modelled in detail (i.e., the kinetics of chemical reactions is not accounted for by the model) and the presence of the boiling water, surrounding the combustion chamber, can be represented by an isothermal boundary condition. These assumptions are validated extensively by comparison with experimental data for different operative conditions. The computational efficiency and reliability of this model make it ready for further studies related to optimization routines, mainly considering changes in the geometry of the boiler.

A lumped-parameter model for professional convection ovens is proposed. The analogy between heat transfer and electric networks offers a great opportunity to describe a complex thermal system with a very simple model and with a low number of tuning parameters. The model can be used to test control strategies under a number of different operating conditions, to carry out optimization studies or to assess energy-saving strategies. In particular the energetic behaviour of such ovens under idle conditions is a crucial aspect to consider for standards (e.g. ENERGY STAR label), thanks to the objectiveness of these conditions and their repeatability.

In the present work the author showed some methods to develop virtual models, which describe energetic aspects of some technologies, widely used in food service professional machines. The extensive validation processes permitted to create robust and reliable models: these two features are considered fundamental during the development phase of virtual models and when the models are used to investigate different scenarios. In fact it is possible to use them in optimization studies with a very low number of tuning parameters and this makes possible to extend the domain of investigation in a reliable way. Moreover the computationally efficiency makes possible to analyse hundreds of working conditions or configurations, in a relatively low time compared to the use of experimental tests.

Appendix A: Comprehensive collection of results for the thawing of the Tylose brick

Here we propose the extensive set of comparisons between experimental and numerical data for the thawing process of the Tylose brick. The graphics refer to nine configurations, obtained combining three nozzle-to-plate distances (H/D= 2, 5, 8) and three Reynolds numbers (Re=17000, 23000, 34000).

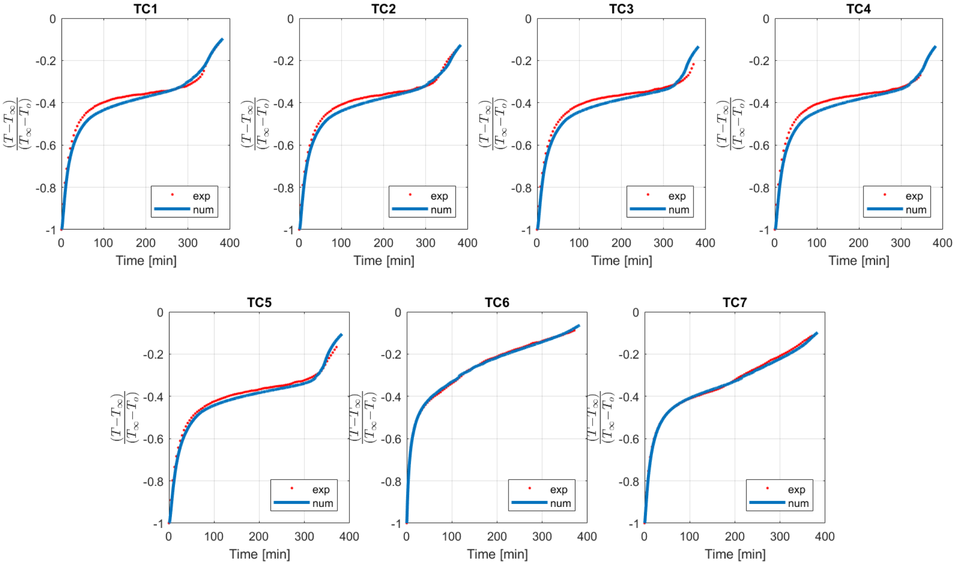

Figure 5.1: Comparison of the numerical and experimental temperature data for Re=17000 and H/D=2

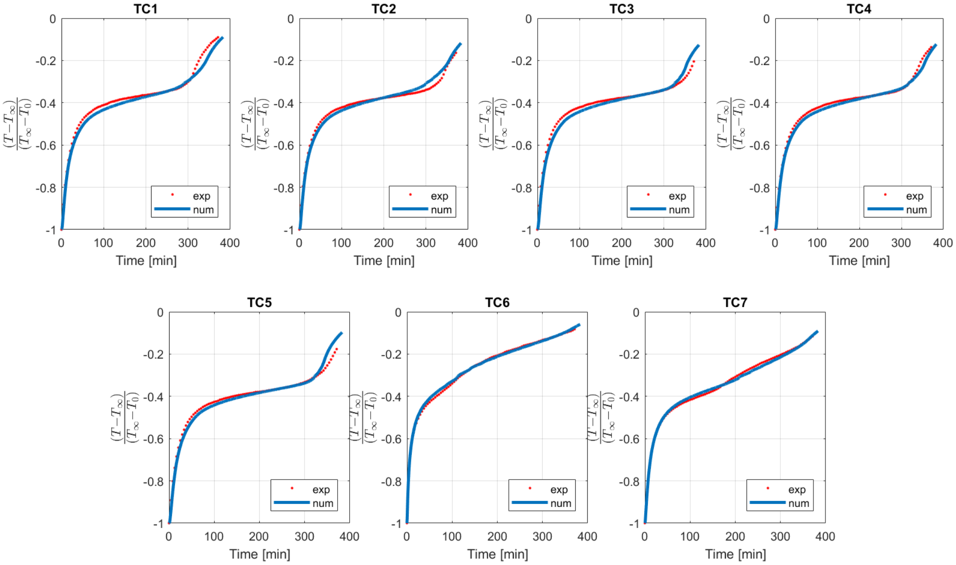

Figure 5.2: Comparison of the numerical and experimental temperature data for Re=23000 and H/D=2

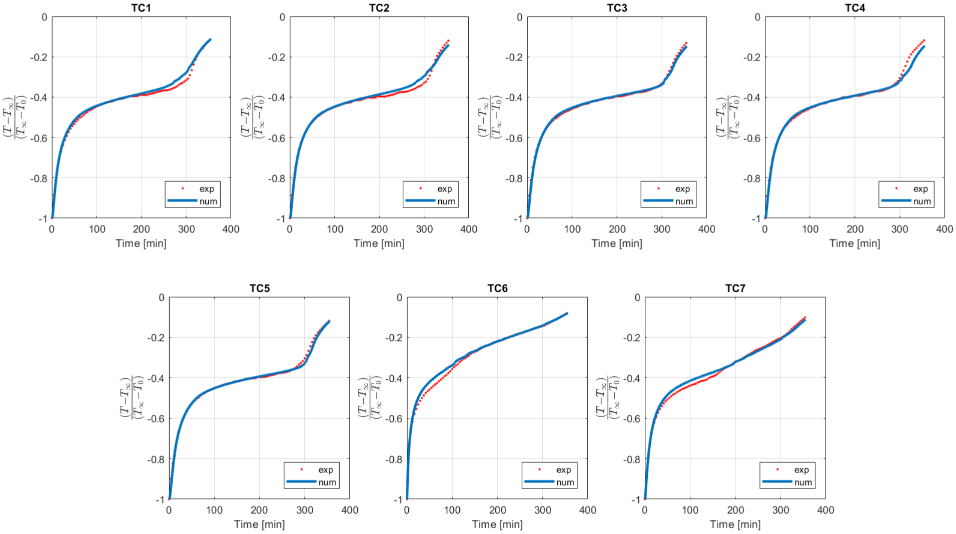

Figure 5.3: Comparison of the numerical and experimental temperature data for Re=34000 and H/D=2

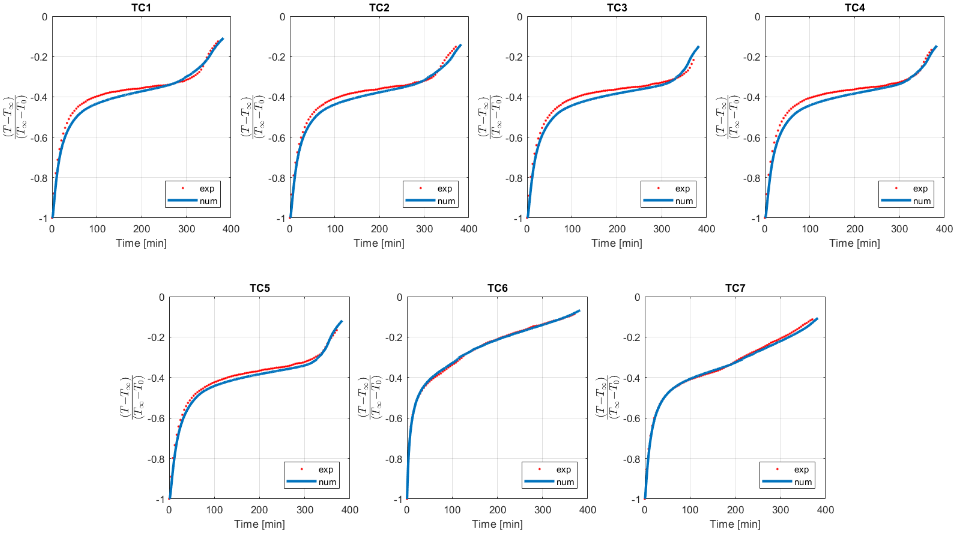

Figure 5.4: Comparison of the numerical and experimental temperature data for Re=17000 and H/D=5

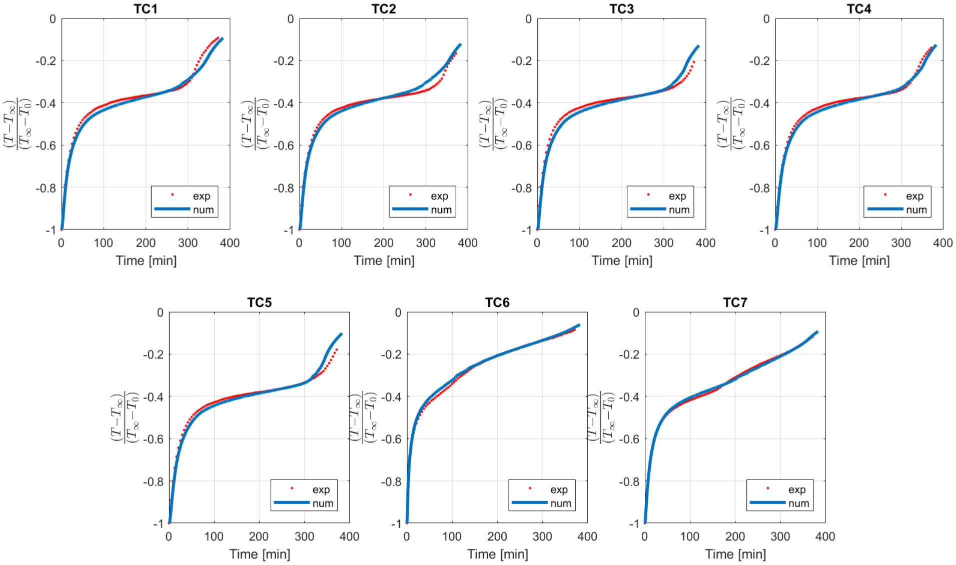

Figure 5.5: Comparison of the numerical and experimental temperature data for Re=23000 and H/D=5

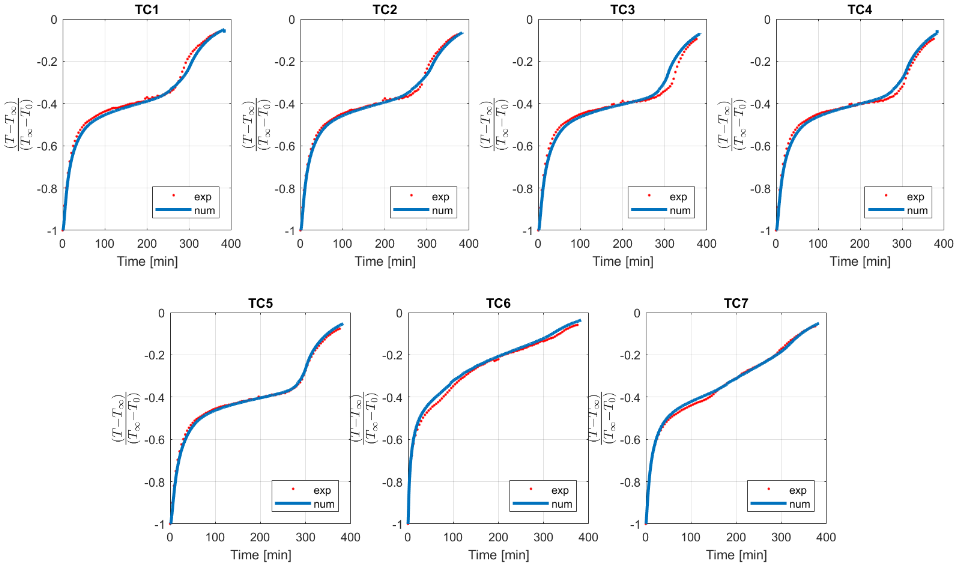

Figure 5.6: Comparison of the numerical and experimental temperature data for Re=34000 and H/D=5

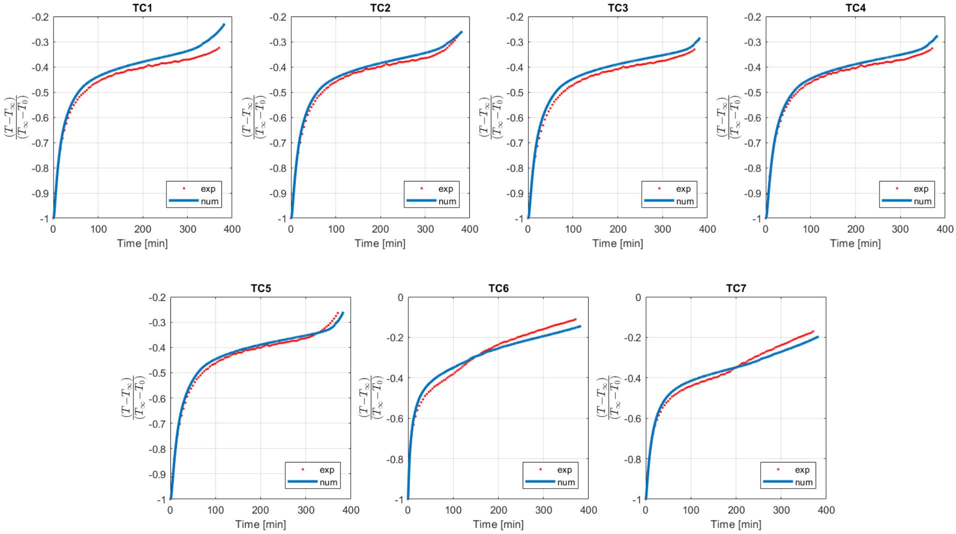

Figure 5.7: Comparison of the numerical and experimental temperature data for Re=17000 and H/D=8

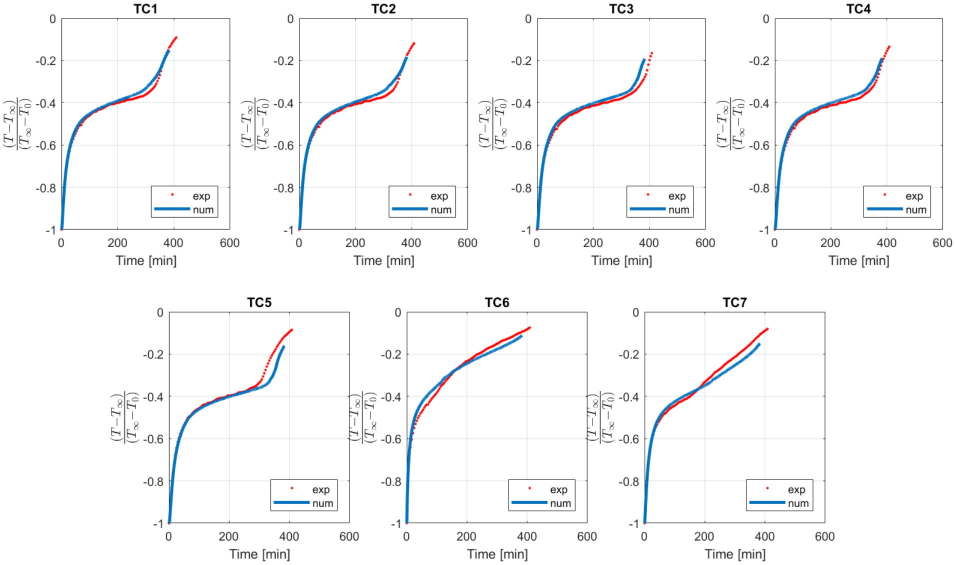

Figure 5.8: Comparison of the numerical and experimental temperature data for Re=23000 and H/D=8

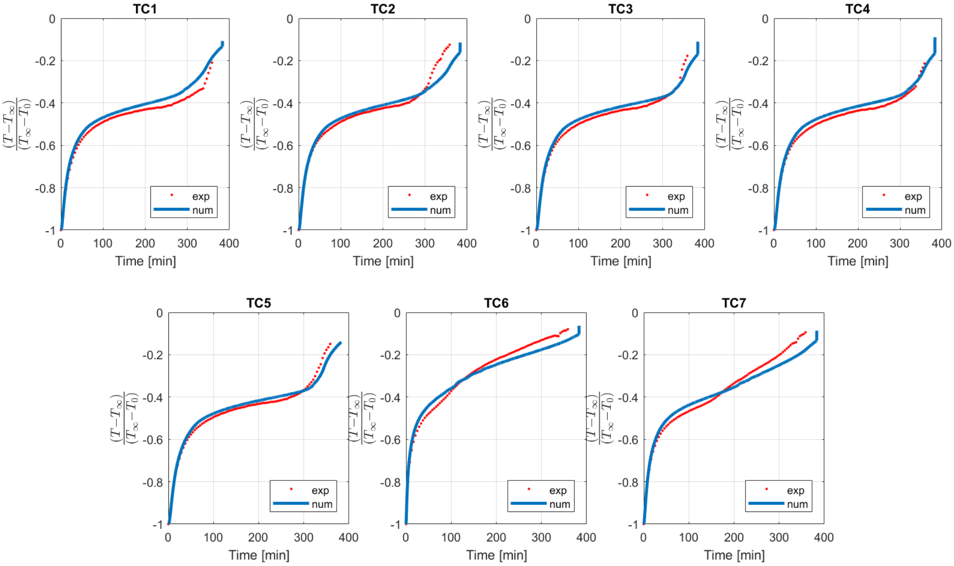

Figure 5.9: Comparison of the numerical and experimental temperature data for Re=34000 and H/D=8

Bibliography

[1] J.P. Abraham and E.M. Sparrow. “A simple model and validating experiments for predictiong the heat transfer to a load situated in an electrically heated oven”. In: *Journal of Food Engineering* 62 (2004), pp. 409–415.

[2] Air-o-Steam. *Air-o-Steam*. Electrolux Professional. 2017.

[3] B. Alfaifi et al. “Radio frequency disinfestation treatments for dried fruits: Model development and validation”. In: *Journal of Food Engineering* 120 (2014), pp. 268–276.

[4] B.A. Anderson and R.P. Singh. “Effective heat transfer coefficient measurement during air impingement thawing using an inverse method”. In: *International Journal of Refrigeration* 29 (2006), pp. 281–293.

[5] B.A. Anderson and R.P. Singh. “Moisture diffusivity in Tylose gel”. In: *Journal of Food Science* 70.5 (2005), pp. 331–337.

[6] N. Athanasios et al. “Optimization of a log wood boiler through CFD simulation methods”. In: *Fuel Processing Technology* 137 (2015), pp. 75–92.

[7] A. Bejan. *Convection Heat Transfer*. Wiley, 2004.

[8] T.L. Bergman et al. *Introduction to Heat Transfer*. John Wiley & Sons, inc., 2011.

[9] C. Bonacina, A. Cavallini, and L. Mattarolo. *Trasmissione del Calore*. 3rd ed. CLEUP, 1989.

[10] C. Bonacina and G. Comini. “On the solution of the nonlinear heat conduction equations by numerical methods”. In: *International Journal of Heat and Mass Transfer* 16.3 (1973), pp. 581–589.

[11] R. Bórquez et al. “Impinging jet drying of pressed fish cake”. In: *Journal of Food Engineering* 40 (1999), pp. 113–120.

[12] M. Bovo and L. Davidson. “Direct comparison of LES and experiment of a single-pulse impinging jet”. In: *International Journal of Heat and Mass Transfer* 88 (2015), pp. 102–110.

[13] R. Buczyński, R. Weber, and A. Szlęk. “Innovative design solutions for small-scale domestic boilers: Combustion improvements using a CFD-based mathematical model”. In: *Journal of the Energy Institute* 88.1 (2015), pp. 53–63.

[14] *Imaging Vector Fields Using Line Integral Convolution*. Proceedings of ACM SigGraph 93. Anaheim, California, Aug. 1993.

[15] A. Cavallini and L. Mattarolo. *Termodinamica Applicata*. CLEUP, 1990.

[16] K.V. Chau and J.J. Gafney. “A finite difference model for heat and mass transfer in products with internal heat generation and transpiration”. In: *Journal of Food Science* 55.2 (1990), pp. 484–487.

[17] N. Chhanwal et al. “Computational fluid dynamics (CFD) modeling of an electrical heating oven for bread-baking process”. In: *Journal of Food Engineering* 100 (2010), pp. 452–460.

[18] D.J. Cleland. “Prediction of freezing and thawing times for foods”. PhD thesis. Massey University, 1985.

[19] J. Collazo et al. “Numerical simulation of a small-scale biomass boiler”. In: *Energy Conversion and Management* 64 (2012), pp. 87–96.

[20] D. Cooper et al. “Impinging jet studies for turbulence model assessment-I. Flow-field experiments”. In: *International Journal of Heat and Mass Transfer* 36.10 (1993), pp. 2675–2684.

[21] P. Di Marco et al. “Mathematical modelling and energy performance assessment of air impingement drying systems for the production of tissue paper”. In: *Energy* 114 (2016), pp. 201–213.

[22] C.O. Díaz-Ovalle et al. “An approach to reduce the pre-heating time in a convection oven via CFD simulation”. In: *Food and Bioproducts Processing* 102 (2017), pp. 98–106.

[23] P. Drosatos et al. “CFD Simulation of Domestic Gasification Boiler”. In: *Journal of Energy Engineering* 143.2 (2017).

[24] J.S. Eastridge and B.C. Bowker. “Effect of Rapid Thawing on the Meat Quality Attributes of USDA Select Beef Strip Loin Steaks”. In: *Journal of Food Science* 76.2 (2011), pp. 156–162.

[25] Electrolux-Oven. *Air-o-Steam brochure*. `http://professional.electrolux.com`. Accessed: 2017-04-18. 2017.

[26] Electrolux-Thawing. *Thawing-Cabinet brochure*. `http://professional.electrolux.com`. Accessed: 2017-04-18. 2014.

[27] ENERGYSTAR. *ENERGY STAR Guide for Cafés, Restaurants and Institutional Kitchens*. Tech. rep. United States Environmental Protection Agency, 2015.

[28] F. Erdogdu and R.P. Singh. “Mathematical modeling of air-impingement cooling of finite slab shaped objects and effect of spatial variation of heat transfer coefficient”. In: *Journal of Food Engineering* 71 (2005), pp. 287–294.

[29] M. Fabbri, Jiang S., and V.K. Dhir. “A Comparative Study of Cooling of High Power Density Electronics Using Sprays and Microjets”. In: *Journal of Heat Transfer* 127.1 (2005), pp. 38–48.

[30] M. Fenot, J.J. Vullierme, and E. Dorignac. “Local heat transfer due to several configurations of circular air jets impinging on a flat plate with and without semi-confinement”. In: *International Journal of Thermal Science* 44 (2005), pp. 665–675.

[31] J.H. Ferziger and M. Perić. *Computationa methods for fluid dynamics*. 3rd edition. Berlin: Springer, 2002.

[32] FireBridge. *Understanding the Impact of Excess Air*. `http://www.firebridgeinc.com/understanding-the-impact-of-excess-air/`. Accessed: 2017-04-18. 2017.

[33] R. Fisher. “Application of "Student’s" distribution”. In: *Metron* 5 (1925), pp. 90–104.

[34] L.W. Florcshuetz, C.R. Truman, and D.E. Metzger. “Streamwise flow and heat transfer distributions for jet array impingement with crossflow”. In: *Journal of Heat Transfer* 103 (1981), pp. 337–342.

[35] L.W. Florschuetz et al. *Multiple Jet Impingement Heat Transfer Characteristic - Experimental Investigation of In-Line and Staggered Arrays With Crossflow*. Tech. rep. NASA, 1980.

[36] Food-Safety. *Food Safety Data Sheet*. Tech. rep. 1555 nr. 17th avenue, Greeley, CO: Weld County Department of Public Health and Environment, 2017.

[37] M.A. Gómez et al. “Dynamic simulation of a biomass domestic boiler under thermally thick considerations”. In: *Energy Conversion and Management* 140 (2017), pp. 260–272.

[38] W. Grassi, P. Conti, and D. Testi. “Development of a Simple Transient Model for Radiant Heating and Cooling Systems and Coupling with Building Energy Simulation”. In: *XXIX UIT Heat Transfer Conference*. 2011.

[39] W.G. Gray et al. *Mathematical tools for changing spatial scales in the analysis of physical systems*. 1st ed. CRC Press, 1993.

[40] D.W. Green and R.H. Perry. *Perry’s Chemical Engineers’ Handbook*. 8th ed. New York: McGraw-Hill, 2008.

[41] C. Grossmann and H.G. Roos. *Numerical Treatment of Partial Differential Equations*. Springer, 2007.

[42] H.M. Hofmann et al. “Calculations of Steady and Pulsating Impinging Jets - An Assessment of 13 Widely used Turbulence Models”. In: *Numerical Heat Transfer, Part B: Fundamentals* 51.6 (2007), pp. 565–583.

[43] J.R. Howell, M.P. Menguc, and R. Siegel. *Thermal Radiation Heat Transfer*. 6th ed. CRC Press, 2016.

[44] A.M. Huber and R. Viskanta. “Effect of jet-jet spacing on convective heat transfer to confined, impinging arrays of axisymmetric jets”. In: *International Journal of Heat and Mass Transfer* 37 (1994), pp. 2859–2869.

[45] S.J. James, C. Bailey, and S. Ono. “Determination of freezing and thawing times in the centre of blocks of meat by measurement of surface temperature”. In: *International Journal of Food Science & Technology* 11.5 (1976), pp. 505–513.

[46] K. Joy. “Determination of radiative view factor without considering the shadowing effect”. In: *International Journal of Advanced Engineering Technology* 5.2 (2014), pp. 91–95.

[47] K. Kim and C. Camci. “Fluid dynamics and convective heat transfer in impinging jets through implementation of a high resolution liquid crystal technique”. In: *International Journal of Turbo and Jet Engines* 12 (1995), pp. 1–12.

[48] J. Kunes. *Dimensionless Physical Quantities in Science and Engineering*. Elsevier, 2012.

[49] N. Lauzier. *View Factors*. `https://www.mathworks.com/matlabcentral/fileexchange/5664-view-factors`. 2004.

[50] A. Li and E. Walker. “Cake Baking in Conventional, Impingement and Hybrid Ovens”. In: *Journal of Food Science* 61.1 (1996), pp. 188–191.

[51] Y. Li et al. “Radio frequency tempering uniformity investigation of frozen beef with various shapes and sizes”. In: *Innovative Food Science and Emerging Technologies* 48 (2018), pp. 42–55.

[52] J.H. Lienard IV and J.H. Lienard V. *A Heat Transfer Textbook*. Phlogiston Press, 2003.

[53] L. Liu et al. “Effect of tangential jet impingement on blade leading edge impingement heat transfer”. In: *Applied Thermal Engineering* 130 (2018), pp. 1380–1390.

[54] C.G. Lomas. *Fundamentals of How Wire Anemometry*. Cambridge University Press, 2011.

[55] Testo LTD. *Testo 340 industrial flue analyzer: technical reference manual*. `http://www.testolimited.com/Content/downloads/testo340-manual-0632_3340.pdf`. Accessed: 2017-04-18.

[56] H.E. Marcroft and M.V. Karwe. “Flow Field in a Hot Air Jet Impingement Oven - Part I: a Single Impinging Jet”. In: *Journal of Food Processing Preservation* 23 (1999), pp. 217–233.

[57] H. Martin. “Heat and Mass Transfer between Impinging Gas Jets and Solid Surfaces”. In: *Advances in Heat Transfer* 13 (1977), pp. 1–60.

[58] R.H. Mascheroni. *Operations in Food Refrigeration*. CRC Press, 2012.

[59] H. Mistry et al. “A methodology to model flow-thermals inside a domestic gas oven”. In: *Applied Thermal Engineering* 31 (2011), pp. 103–111.

[60] C.P. Mohanty, S.S. Mahapatra, and J. Sahu. “Parametric optimisation of electrical discharge machining process: A numerical approach”. In: *International Journal of Industrial and Systems Engineering* 22.2 (2016), pp. 207–244.

[61] R.G. Moreira. “Impingement drying of foods using hot air and superheated steam”. In: *Journal of Food Engineering* 49 (2011), pp. 291–295.

[62] S. Mudie et al. “Electricity use in the commercial kitchen”. In: *International Journal of Low-Carbon Technologies* 11 (2016), pp. 66–74.

[63] N. Nitin and M.V. Karwe. “Heat Transfer Coefficient for Cookie Shaped Objects in a Hot Air Jet Impingement Oven”. In: *Journal of Food Processing Engineering* 24 (2001), pp. 51–69.

[64] T.S. O’Donovan and D.B. Murray. “Jet impingement heat transfer e Part I: Mean and root-mean-square heat transfer and velocity distributions”. In: *International Journal of Heat and Mass Transfer* 50 (2007a), pp. 3291–3301.

[65] T.S. O’Donovan and D.B. Murray. “Jet impingement heat transfer e Part II: A temporal investigation of heat transfer and local fluid velocities”. In: *International Journal of Heat and Mass Transfer* 50 (2007b), pp. 3302–3314.

[66] A.J. Onstad et al. “Flow and heat transfer for jet impingement arrays with local extraction”. In: *Sixth International Symposium on Turbulence and Shear Flow Phenomena*. 2009, pp. 315–320.

[67] D.Z. Ovadia. *Impingement Oven Airflow Devices and Methods*. U.S. patent document. Patent No. US6320165B1. Pizza Hut, Inc., 2000.

[68] S.V. Patankar. *Numerical Heat Transfer and Fluid Flow*. Hemisphere Publishing Corporation, 1980.

[69] S.K. Peddapelli. *Pulse Width Modulation*. De Gruyter Oldenbourg, 2017.

[70] K.S. Pitzer. “The volumetric and thermodynamic properties of fluids. I. Theoretical basis and virial coefficients”. In: *Journal of the American Chemical Society* 77.13 (1955), pp. 3427–3433.

[71] S.B. Pope. *Turbulent flows*. Cambridge University Press, 2000.

[72] A. Pugliese. “Set-up e calibrazione di un apparato sperimentale per misure locali di velocitÃ in una galleria del vento per prove radiatori.” MA thesis. Dipartimento di Ingegneria "Enzo Ferrari", UniversitÃ degli studi di Modena e Reggio Emilia, 2017.

[73] E. Ramirez-Laboreo, C. Sagues, and S. Llorente. “Dynamic heat and mass transfer model of an electric oven for energy analysis”. In: *Applied Thermal Engineering* 93 (2016), pp. 683–691.

[74] Riedel. “Eine prufsubstanz fur gefrierversuche”. In: *Kaltetechnik* 12 (1960), pp. 222–225.

[75] G. Ruocco, M.V. De Bonis, and F. Marra. “Combining microwave and jet-impingement in a oven prototype”. In: *Procedia Food Science* 1 (2011), pp. 1331–1337.

[76] V.G. Ryckaert, J.E. Claes, and J.F. Van Impe. “Model-based temperature control in ovens”. In: *Journal of Food Engineering* 39 (1999), pp. 47–58.

[77] A. Ryfa, D. Ingham, and R.A. Bialecki. “Direct and Inverse Methods for an Air Jet Impingement”. In: *Numerical Heat Transfer, Part A: Applications* 61.7 (2012), pp. 547–568.

[78] V.O. Salvadori and R.H. Mascheroni. “Analysis of impingement freezers performance”. In: *Journal of Food Engineering* 54 (2002), pp. 133–140.

[79] A. Sarkar and R.P. Singh. “Spatial variation of convective heat transfer coefficient in air impingement applications”. In: *Journal of Food Science* 68.3 (2003), pp. 910–916.

[80] R.A. Sherman. *Radiation from luminous and non-luminous natural-gas flames*. Tech. rep. Meeting of the Pittsburgh Section of the American Society of Mechanical Engineers, with the Iron and Steel Institute and the Engineers’ Society of Western Pennsylvania, Feb. 1933.

[81] R. Siegel and J.R. Howell. *Thermal Radiation Heat Transfer*. Hemisphere Publishing Corporation, 1992.

[82] D. Singh, B. Premachandran, and S. Kohli. “Numerical Simulation of the Jet Impingement Cooling of a Circular Cylinder”. In: *Numerical Heat Transfer, Part A: Applications* 64.2 (2013), pp. 153–185.

[83] D.P. Smith. *Cooking Apparatus*. U.S. patent document. Patent No. US3884213. 1973.

[84] E. Stalio and E. Nobile. “Direct numerical simulation of heat transfer riblets”. In: *Int. Journal of Heat and Fluid Flow* 24 (2003), pp. 356–371.

[85] STAR-CCM+. *STAR-CCM+ manual*. © SIEMENS PLM Software. 2017.

[86] J. Taghinia, M.M. Rahman, and T. Siikonen. “Numerical investigation of twin-jet impingement with hybrid-type turbulence modeling”. In: *Applied Thermal Engineering* 73 (2014), pp. 650–659.

[87] D. Testi et al. “Building energy simulation by an in-house full transient model for radiant systems coupled to a modulating heat pump”. In: *Energy Procedia* 78 (2015), pp. 1135–1140.

[88] UNI-10389-1:2009. *Generatori di calore: Misurazione in opera del rendimento di combustione*. 2009.

[89] UNI-EN-ISO-6946:2008. *Componenti ed elementi per edilizia - Resistenza termica e trasmittanza termica - Metodo di calcolo*. Tech. rep. UNI-Ente Italiano di Normazione, 2008.

[90] H. Versteeg and W. Malalasekra. *An Introduction to Computational Fluid Dynamics*. 2nd ed. Pearson, 2007.

[91] J.M.F. Vickers. “Heat Transfer Coefficients between Fluid Jets and Normal Surfaces. Behaviour of Laminar Impacted Jets”. In: *Industrial and Engineering Chemistry* 51.8 (1959), pp. 967–972.

[92] U. Wählby, C. Skjöldebrand, and E. Junker. “Impact of impingement on cooking time and food quality”. In: *Journal of Food Engineering* 43 (2000), pp. 179–187.

[93] J. Wang et al. “Effect of high-humidity hot air impingement blanching (HHAIB) on drying and quality of red pepper”. In: *Food Chemistry* 220 (2017), pp. 145–152.

[94] A.A. Westenberg and J.L. Rice. “Further measurements of turbulence intensity in flame zones”. In: *Combustion and Flame* 3.C (1959), pp. 459–465. url: `https://www.scopus.com/inward/record.uri?eid=2-s2.0-49749208841&partnerID=40&md5=6e5a51ef4c47361cce7a29a55f7ff4a7`.

[95] S. Whitaker. *The Method of Volume Averaging*. Springer Science + Business Media Dordrecht, 1999.

[96] H.W. Xiao et al. “The application of superheated steam impingement blanching (SSIB) in agricultural product processing - A review”. In: *Journal of Food Engineering* 132 (2014), pp. 39–47.

[97] R.N. Yadav, V. Yadava, and G.K. Singh. “Application of response surface methodology and genetic algorithm for optimisation of electro-discharge diamond face grinding of tungsten carbide-cobalt composite”. In: *International Journal of Industrial and Systems Engineering* 18.1 (2014), pp. 76–94.

[98] Y.S. Yang et al. “The multi-objective optimisation design for a light guide rod”. In: *International Journal of Industrial and Systems Engineering* 20.2 (2015), pp. 165–179.

[99] C. Yin et al. “A gas radiation property model applicable to general combustion CFD and its demonstration in oxy-fuel combustion simulation”. In: *Energy Procedia* 120 (2017), pp. 564–571.

[100] P. Yu et al. “Heat transfer rate and uniformity of mist flow jet impingement for glass tempering”. In: *International Journal of Heat and Mass Transfer* 115 (2017), pp. 368–378.

[101] L. Zhang et al. “Experimental and numerical investigation for hot water boiler with inorganic heat pipes”. In: *International journal of heat and mass transfer* 114 (2017), pp. 743–747.

[102] N. Zuckerman and N. Lior. “Jet impingement heat transfer: physics, correlations and numerical modeling”. In: *Advances in Heat Transfer* 39 (2006), pp. 565–631.